Structural and Luminescence Properties of RE Doped Fluoride and Silicate Phosphors

By

Nebiyu Gemechu Debelo (M.Sc)

A Thesis Presented in Fulfillment of the Requirement of the Degree of

Philosophiae Doctor/Doctor of Philosophy (PhD)

In the

Faculty of Natural and Agricultural Sciences, Department of Physics

At the

University of the Free State, Republic of South Africa

Promoter: Prof. F. B. Dejene

Co-Promoter: Dr. Kittessa Roro

April 2017

Declaration

This research has not been previously presented for any degree and is not being currently considered for any other degree at any other university. I declare that this thesis contains my own research work except where specifically acknowledged.

Name: **Nebiyu Gemechu Debelo** Student Number: **2014213199**

Signature:  Date: April 26, 2017

This thesis is dedicated to my loving wife (Eyu), my dear parents, brothers and sisters.

Acknowledgements

Thank you God for honoring me! My deep, heart-felt special gratitude and acknowledgement goes to following persons.

- My promoter Prof. F. B Dejene and co-promoter Dr. Kittessa Roro for their most valuable insight, invaluable suggestions, comments, scientific advice, scholarly remarks, respect and understanding throughout the duration of this study.
- UFS research directorate for its financial support
- Dr. K. G. Tshabalala, Dr. Fekadu Gashaw, Dr. L. F. Koao, Dr. Ahmen Iorokya, Mr. S. J. Motloung, Mr. R. O. Ocaya, Mr. T. D. Malevu, Mr. Jatani Ungula, Ms. W. M. Winfred, Ms. M. A. Lephoto, Ms. A. S. Tebele, Ms. Sharon Kiprotich, Ms. L. Meiki of the UFS, Qwa Qwa campus, Physics department for their useful help and discussions.
- Dr. Moges Yihunie, Dr. Ali Halake Wako and Dr. Raphael for their help on experimental techniques
- South African National Laser Center (NLC) for financial, logistic, and technical support.
- Dr. Bathusile Masina and Mr. Bafana Moya for his continuous assistance during pulsed laser deposition at National Laser Center (NLC). Bafana you suffered with me in that PLD room!
- Ms. P. Mokoena for SEM and CL measurements.
- National Metrology Agency of South Africa (NMSA) for SEM and XPS measurements.
- All staff members in the department of physics of UFS, Bloemfontein campus for their assistance and support.
- My parents, brothers and sisters for their encouragement and moral support.
- My wife Eyerusalem Abebe for her patience, love and continuous support.

Abstract

This work covers several aspects of rare earth activated silicate and fluoride commercial phosphor powders and thin films. All the films were synthesized by pulsed laser deposition technique using Nd-YAG laser and characterized by different techniques with the sole aim of studying their structural and luminescence properties for possible applications in dosimetry and display devices.

The Thermoluminescence (TL) properties of $Y_2SiO_5 : Ce^{3+}$ phosphor powder and thin films were reported. For the phosphor powder, the TL intensity increases with an increase in UV dose for up to 20 minutes and then decreases. The TL intensity peak shifts slightly to higher temperature region at relatively high heating rates, but with reduced peak intensity. Important TL kinetic parameters, such as the activation energy (E) and the frequency factor (s) were calculated from the glow curves using a variable heating rate (VHR) method and it was found that the glow peaks obey first order kinetics. For the films, broad TL emissions over a wide temperature range with low intensity as compared to that of the powder were observed. The maxima of the TL glow peaks of the films deposited in oxygen ambient and vacuum shift towards higher temperature relative to the TL peak position of the film deposited in an argon environment. Vacuum environment resulted in the formation of a deep trap as compared to oxygen and argon environments. Furthermore, the structure of $Y_2SiO_5 : Ce^{3+}$ phosphor powder transformed from x_2-monoclinic polycrystalline phase to x_1-monoclinic polycrystalline phase at low substrate temperature deposition.

TL and photoluminescence (PL) properties of $KY_3F_{10}: Ho^{3+}$ phosphor powder is also reported. The TL measurements were done for different heating rates and for various duration of UV exposure. The TL intensity increases with duration of UV exposure up to 20 minutes and then decreases. Decrease of the glow peak height was observed for the glow curves with increasing heating rate. The area under TL-time plot is calculated for each heating rate at constant UV dose and it is found to be constant and independent of the heating rate. It is therefore, the observed decrement in intensity of each glow curve following increment in heating rate is not attributed to the thermal quenching effect. Important TL kinetic parameters namely, the activation energy (E) and the frequency factor (s) were calculated using variable heating rate (VHR) method. The glow peaks obey first order kinetics.

$KY_3F_{10}: Ho^{3+}$ thin films were deposited by a pulsed-laser deposition technique with Nd-YAG laser radiation (λ= 266 nm) on (100) silicon substrate. The influence of background gas pressure, target to

substrate distance, and substrate temperature on structural, morphological and luminescence properties of the films have been investigated. For the film grown under different background gas pressure, the XRD and FE-SEM results show improved crystalline structure for the film deposited at a pressure of 1 Torr. The AFM results show that the RMS roughness of the films increases with rise in argon gas pressure. The EDS elemental mapping shows Y-excess for all the films deposited under all pressures and this is attributed to its higher mass and low volatility as compared to K and F. XPS analysis further confirmed Y-excess in the deposited films. XRD analysis of the films deposited under various target to substrate distances in the range of 4-7 cm shows that high crystalline quality film with largest grain size is obtained for target to substrate distance of 4 cm. Decrease in the thickness of the films is observed at larger target to substrate distances. This is attributed to the increased hemispherical expansion of the laser induced plasma plume at larger distances reducing the particle flux of the target species over a substrate area. Moreover, all the films are characterized by low reflectance and high absorption in the visible region. Furthermore, for the films deposited under various substrate temperatures, the crystallinity is improved following increment in deposition temperature and the calculated average crystallite size is in the range of 39-74 nm.

For all the $KY_3F_{10}:Ho^{3+}$ commercial phosphor powder and thin films, PL emission spectra were also investigated at four main excitation wavelengths; namely, 362, 416, 454 and 486 nm. Green emission at 540 nm and faint red emission at 750 nm were observed for all the excitations. The green emission at 540 nm is ascribed to the $^5F_4$–$^5I_8$ and $^5S_2$–$^5I_8$ transitions and the faint red emission at 750 nm is due to the $^5F_4$ –$^5I_7$ and $^5S_2$–$^5I_7$ transitions. In addition to the sharp green emission at 540 nm, a broad emission centered at 600 nm was observed for excitation wavelength of 362 nm for the powder. The highest PL intensity occurs at excitation of 454 nm for all samples of this material.

The Cathodoluminescence (CL) images of the films deposited under various background gas pressures show non uniform distribution of luminescent centers in the deposited films. Moreover, the CL emission spectra are similar to those of the PL with the main peak at 540 nm, suggesting that the electron beam did not change the electron energy level configuration or transitions of the activator ion in the film.

Table of Contents

List of Figures

List of Tables

Chapter 1
General Introduction

1.1 Background

Phosphor research delivered promising results for several new applications in today's science and technology including display medium and dosimetry. Different phosphors with different activators (dopants) and thus different colors and luminescent properties were investigated [1-3] and deep level research is still underway for investigation of highly optimized phosphor powders or thin films for related applications. Practical utilization of phosphor powders/thin films strongly depends on their optical properties which in turn depend on parameters such as host structure, presence of defects/dopants and their location in the host material, method of synthesis, post synthesis treatment (for example, annealing), etc. The chemical composition, electronic and luminescence properties of the phosphor powders or thin films also depend on these parameters.

The structure and properties of the host material plays a crucial role in determining its luminescence properties. Therefore, selection of a suitable host material which can lead to improved luminescence efficiency is very important. In general, a host material should possess high chemical durability and thermal stability for high temperature processes and be more chemically stable depending on the potential application. It has been reported that oxide based phosphors satisfy these properties [4]. Moreover, to reduce non-radiative recombination probability, a phosphor with low phonon energy is required and fluoride based phosphors fulfill this property [5-6]. Non-radiative recombination is reported to reduce the luminescence efficiency. Controlling the host matrix composition via chemical modification, for instance, doping with metal ions, also influences the host chemical environment and hence the resultant luminescence properties.

Introduction of impurities (dopants) in to the host generates defects or surface states which influence the band gap. Doping induces oxygen vacancies that form electron-trap centers which helps delay the decay of charge carriers, enhances the visible light absorption property and decreases the electron hole recombination rate [7]. Modifying the luminescence of the rare earth elements (dopants) can also be achieved by controlling the dopant concentration. Moreover, the luminescence properties of materials are also strongly associated with geometrical factors such as shape, dimensionality, size, etc. Crystalline, spherical shaped, uniform size particles with narrow size distribution with well-defined morphologies can reduce light scattering and produce fine luminescence properties [8].

In some applications such as field emission displays, thin film phosphor materials are more advantageous than powders in reducing outgassing problems and having high resolution and contrast [9]. Therefore, study of thin film phosphors is equally as important as that of powders. Furthermore, the luminescence properties of materials are in general improved following miniaturization to nanoscale [10]. Therefore, films with thickness of few hundreds of nanometers can give high luminescence efficiency than powders depending on deposition conditions. The success in the production of nanomaterials which involve control of size, shape and structure of the materials has been possible because of the success in the development of nanoscience and nanotechnology. During the last few years, insulating nanomaterials have been produced in large quantities by the use of physical and chemical techniques. In particular, various thin film synthesis (deposition) techniques, such as pulsed laser deposition (PLD), chemical bath deposition, magnetron sputtering etc, have been developed. However, it is reported that PLD has many advantages over other thin film deposition techniques.

PLD is a highly flexible thin-film growth technique which has been successfully applied to a wide range of materials [l1-13]. The energetic nature of the depositing species enhances the growth process, potentially enabling the deposition of high quality films on low-temperature substrates. Additionally, sequential ablation of multiple target materials allows accurate control of the film stoichiometry, enabling the growth of heterostructures and the deposition of films with well-defined doping profiles. Moreover, the possibility of using inert gases as background environment facilitates the growth of the films in a non-reactive medium. This is especially important for deposition of fluoride films which, otherwise, are reactive at the presence of oxygen. In this work, in addition to structural properties, photoluminescence (PL) and thermoluminescence (TL) properties of the phosphor powders and thin films grown by PLD are investigated for possible applications in display devices and radiation dosimetry.

Thermoluminescence (TL) spectrum, also called TL glow curve, gives the intensity of the emitted light as a function of temperature at a particular exciting radiation dose. Radiation dose plays a crucial role in the filling of the traps constituting a TL material and the TL response of a given sample to a known dose depends on the number of the traps filled by the given dose. A simple way to estimate the number of the filled traps is to assume the filling rate to be directly proportional to the dose and also directly proportional to the vacancies in the traps [14]. The dose at which all of the traps get filled up depends solely on the fraction of vacant traps which get filled up per unit dose. The TL intensity of most phosphor materials increases with increasing radiation dose up to a certain level and then decreases. This

decrease of the TL signal can be attributed to the stronger competition with non-radiative centers at higher doses [15]. At a given temperature of irradiation, many phosphor materials display an intensity of TL which is proportional (or nearly so) to the amount of radiation absorbed, and this leads to the fact that TL may be used as a means of radiation dosimetry. In general the TL signal of a good dosimeter is directly proportional to the applied dose.

The absorption of radiation increases the level of TL observed from a specimen by filling the localized energy levels with trapped electrons. The absorption of heat from the environment, on the other hand, tends to reduce the numbers of trapped electrons by thermally releasing them. Thus, the intensity of the TL is a competition between trap filling by radiation and trap emptying by thermal excitation. Investigating the TL properties of a material is crucial in the development of more efficient materials though many challenges are being faced during the manufacturing and processing of these materials. Therefore, there should be ways that would help overcome these challenges and enhance the TL properties of a phosphor. This includes selection of a suitable host material with high chemical durability and thermal and chemical stability.

Photoluminescence (PL) spectrum shows the intensity of the emitted light as a function of the excitation wavelength at particular excitation energy. Light is directed onto a sample, where it is absorbed and imparts excess energy into the material in a process called photo-excitation. The peak position and intensity of the corresponding emission is strongly dependent on the excitation energy. This enables researchers to select a suitable excitation wavelength for the required emission in display devices and light emitting diodes. For the deposited thin films, the PL intensity also strongly depends on the various deposition parameters such as background gas pressure, target to substrate distance, laser fluence and the type of background atmosphere. This is also important in optimizing the thin films for the required emission.

In this thesis, experimental study of TL properties of $KY_3F_{10}:Ho^{3+}$ phosphor powder, $Y_2SiO_5:Ce^{3+}$ phosphor powder and thin films were studied. Moreover, the PL phenomena in $KY_3F_{10}:Ho^{3+}$ phosphor powder and thin films were investigated. In particular, PL and TL properties of $KY_3F_{10}:Ho^{3+}$ phosphor, TL properties of $Y_2SiO_5:Ce^{3+}$ phosphor powder and thin films, The effect of argon gas pressure on structural, morphological and photoluminescence properties of pulsed laser deposited $KY_3F_{10}:Ho^{3+}$ thin films, Pulsed laser deposited $KY_3F_{10}:Ho^{3+}$ thin films: Influence of target to substrate distance, Improved crystallinity and luminescence properties of $KY_3F_{10}:Ho^{3+}$ thin films at high temperature deposition were studied. The phosphors were characterized by X-ray diffraction (XRD),

Photoluminescence spectroscopy, Ultra Violet-Visible (UV-VIS) spectroscopy, Thermoluminescence spectroscopy, Transmission electron microscopy (TEM), Atomic force microscopy (AFM), Scanning electron microscopy (SEM), and X-ray photoelectron spectroscopy (XPS).

1.2 Statement of the problem

The sudden increase in the source of ionizing radiations due to the various applications of nuclear energy in military and civil applications brought forth the necessity of a simple, reliable, and cheap method for their measurement. The TL phosphors used in the present day dosimetry such as LiF and CaF_2:Mn are extensively studied and varieties of TL phosphors are now being produced in large scale commercially for applications in radiation protection and medical radiation dosimetry. However, scientific research geared towards developing more efficient dosimeter is still underway. Therefore, studying inorganic materials (phosphors) that can be effectively and more efficiently used in radiation dosimetry is highly important at present time. In addition, more should be done on how the TL characteristics of a material is directly related to the materials solid state properties and how these solid state properties are being utilized in the field of radiation dosimetry.

Moreover, in the recent years, much attention has been focused on different phosphor materials due to their commercial applications in color television, fluorescent tube, X-ray phosphors, and scintillators. Recently various phosphor materials have been actively investigated to improve their luminescent properties and to meet the development of different display and luminescence devices. However, there is growing interest in the development of new full color emitting phosphor materials that combine thermal and chemical stability in air with high emission quantum yield at room temperature. It has been reported that the sulfide component in a sulfide based phosphors degrade rapidly in moisture and also at high current density necessary for field emission displays while oxide based phosphors have been found to be more stable under these conditions. Moreover, fluoride based phosphors have the advantage of enhancing luminescence efficiency since the low phonon frequency of their host lattice reduces non-radiative relaxation. Therefore, selection of fluoride and silicate based host materials for improved luminescence performance of a material is highly important.

1.3 Objectives of the study

The following are the objectives of the study.

- Studying the TL properties of $Y_2SiO_5:Ce^{3+}$ commercial phosphor powder and thin films.
- Studying the TL and PL properties of $KY_3F_{10}:Ho^{3+}$ commercial phosphor powder

- Investigating the structural and luminescence properties of $KY_3F_{10}:Ho^{3+}$ thin films deposited under varying deposition conditions such as background gas pressure, substrate temperature and target to substrate distance.

1.4 Thesis Layout

Chapter 2 deals with the theoretical background on luminescence phenomena in general and TL, PL and CL in particular. The mechanism of TL and PL and the different models of TL are discussed in this chapter. PLD as effective and flexible method for thin film growth is discussed in chapter 3. In chapter 4, the different experimental techniques used for characterization are discussed in detail. The main results of this study are discussed in chapters 5, 6, 7, 8 and 9. Chapter 5 deals with thermally stimulated luminescence of $Y_2SiO_5:Ce^{3+}$ commercial phosphor powder and thin films. Thermoluminescence and photoluminescence study of $KY_3F_{10}:Ho^{3+}$ commercial phosphor powder is covered in chapter 6. Chapter 7 deals with the effect of argon gas pressure on structural, morphological and photoluminescence properties of pulsed laser deposited $KY_3F_{10}:Ho^{3+}$ thin films, while the influence of target to substrate distance on structural and luminescence properties of the films is discussed in chapter 8. The improved in crystallinity and luminescence properties of $KY_3F_{10}:Ho^{3+}$ thin films at high deposition temperature is covered in chapter 9. Finally, the Cathodoluminescence properties of $KY_3F_{10}:Ho^{3+}$ thin films are studied in chapter 10.

References

[1] N. G. Debelo, F. B. Dejene, K. T. Roro, M. P. Pricilla, C. Oliphant, Appl. Phys. A, 122, 1 (2016).

[2] J. J. Dolo, H. C. Swart, J. J. Terblans, E. Coetsee, M. S. Dhlamini, O. M. Ntwaeaborwa, F. B. Dejene, Phys.Stat.Sol. (c), 5, 594 (2008).

[3] H. C. Swart, J. J. Terblans, O. M. Ntwaeaborwa, E. Coetsee, B. M. Mothudi, M. S. Dhlamini, Nucl. Instr. and Meth. B, 267, 2630 (2009).

[4] P. Kumari, P. K. Baitha, J Manam, Indian J Phys 89, 1297 (2015).

[5] S. Khiari, F. Bendjedaa, M. Diaf, Optics and Photonics Journal 3, 13 (2013).

[6] Y. Zheng, G. Feng, C. Qing, L. Lin, L. Ting, J. Hyun, Chin. Phys. B 23, 064212 (2014).

[7] B. Choudhury, A. Choudhury, J. Lumin. 136, 339 (2013).

[8] R. Vacassy, S. Scholz, J. Dutta, C. Plummer, R. Houriet, H. Hofmann, J. Am. Ceram. Soc. 81, 2699 (1998).

[9] K. T. Hillie, H. C. Swart, Appl. Surf. Sci. 183, 304 (2001).

[10] L. R. Singh, S. D. Singh, J. Nanomaterials 2012, 1 (2012).

[11] D. Fu, K. Liu, T. Tao, K. Lo, C. Cheng, B. Liu, R. Zhang, H. Bechtel, J. Wu, J. Appl. Phys 113, 043707 (2013).

[12] D. H. Kim, H. S. Kwok, Appl. Phys. Lett. 65, 3188 (1994).

[13] J. M. Cowly, Handbook of Nanophase and Nanostructured Materials: Synthesis, Tsingua University press, 2003.

[14] C.M. Sunta, E. Okuno, J.F. Lima, E.M. Yoshimura, J. Phys. D Appl. Phys. 27, 2636 (1994).

[15] R. Chen, D. Lo, J. L. Lawless, Radiat. Prot. Dosim. 119, 33 (2006).

Chapter Two

Review of Theoretical Concepts

2.1.Theory of luminescence

Luminescence is a collective term for different phenomena where a substance emits light without being strongly heated, i.e., the emission is not simply thermal radiation [1]. This definition is also reflected by the term "cold light". Luminescence can be categorized in to fluorescence or phosphorescence. Fluorescence is light emission caused by irradiation with light (normally visible or ultraviolet light) and typically occurring within nanoseconds to milliseconds after irradiation [1-3]. It involves the excitation of electrons into states with a higher energy, from which radiative decay is possible. Typically, the emitted wavelengths are longer than the excitation wavelengths; otherwise up-conversion fluorescence will occur. Phosphorescence is a light emission that can occur over much longer times (sometimes hours) after irradiation [1-3]. It involves storage of energy in metastable states and its release through relatively slow (often thermally activated) processes. In other words, phosphorescence is a radiational transition, in which the absorbed energy undergoes intersystem crossing into a state with a different spin multiplicity [4]. This will be discussed in detail in section 2.3. The lifetime of phosphorescence is usually from $10^{-4} - 10^{-2}$ s, much longer than that of fluorescence [4].

Table 2.1: Summary of types of luminescence [1]

Type of luminescence	**Excitation mechanism**
Thermoluminescence	Heat
Photoluminescence	Electromagnetic radiation
Cathodoluminescence	Electrons
Electroluminescence	Electric field
Triboluminescence	Mechanical energy
Radioluminescence	Electromagnetic radiation
Sonoluminescence	Sound waves
Chemiluminescence	Chemical reaction
Bioluminescence	Chemical reaction

Luminescence is, in some ways, the inverse process to absorption. Absorption of photons of appropriate frequency causes an atomic system shift to the excited states. This atomic system can return to the ground state by spontaneous emission of photons.

This de-excitation process is called luminescence. However, the absorption of light is only one of the multiple mechanisms by which a system can be excited. In a general sense, luminescence is the emission of light from a system that is excited by some form of energy [1-4]. The origin of the luminescence from a phosphor is the host material or the dopants or both of them. A dopant, which is also called an activator, is an impurity ion which is incorporated in to the host lattice to form a luminescent center. This luminescence center absorbs energy and gives off luminescence when excited. Depending on the excitation mechanism, luminescence can be categorized in to different types. The most important types of luminescence are summarized in Table 2.1.

In luminescence process, the emission spectrum shifts to a lower energies relative to the absorption spectrum. This shift is called Stoke's shift. It is also possible to obtain luminescence at photon energies higher than the absorbed photon energy. This is called anti-Stokes or up-conversion luminescence and it occurs for multilevel systems.

Having briefly looked at the basic definition and types of luminescence, let us now discuss in detail some basic types of luminescence which are frequently studied in this research work.

2.2.Thermoluminescence

Thermoluminescence (TL) is the phenomenon of light emission upon heating a material, which has been previously excited [5]. All types of radiations such as gamma rays, x-rays, alpha rays, beta rays and light rays can 'excite' a material but to widely different extents. Out of the excitation energy imparted, a very large portion is almost instantaneously dissipated by various processes such as heat and light and only some amount is absorbed and stored in it. On subsequent heating the energy may be released and some of it may be in the form of light, which we call TL. The underlying mechanism involves the role of (i) crystal defects which allows the storing of energy derived from exposure to radiation through the trapping of carriers at these defect centers and (ii) subsequent release of stored energy as visible light when these trapped carriers, after having been freed by thermal stimulation, recombine at the luminescent centers provided by impurity atoms in the solids. The phenomenon of TL has also been termed as thermally stimulated luminescence (TSL) [1, 6-7]. Thermoluminescence means not temperature radiation but enhancement of the light emission of materials already excited electronically

by the application of heat. TL can be distinguished clearly from incandescence emission from a material on heating. In incandescence, which is classical in nature, radiation is emitted when the material is very hot. The fundamental principles which govern the production of TL are essentially the same as those which govern all luminescence processes and hence TL is one member of a large family of luminescence [2]. To get TL emission from a material three essential conditions are necessary. Firstly the material must be an insulator or a semiconductor. Secondly the material should have some time-absorbed energy during exposure to radiation. Thirdly heating the material triggers the luminescent emission. Once TL emission has been observed the material will not show it again after simply cooling the specimen and reheating it but has to be exposed to radiation to obtain TL again. The plot of intensity of the emitted light against temperature is known as glow curve.

The fraction η of the excited carriers which produces luminescence during heating stage (luminescence efficiency) is given by the following equation [1],

$$\eta = \frac{R_{rec}}{R_{ret} + R_{rec}} \qquad (2.1)$$

The value of η strongly depends on the values of the parameters such as the probabilities of re-trapping/recombination and the concentration of the charge carriers). Depending on the existence of other possible routes of relaxation, for example non-radiative recapture in deeper level traps, the denominator in (2.1) may increase. Therefore, the expression of η would change according to the applicable physical model.

2.2.1 Early models of Thermoluminescence

The theoretical model for the TL emission was first suggested by Randall and Wilkins (RW) [8]. They assumed that the retrapping may be negligible ($R_{ret} = 0$) and therefore according to (2.1), we have η = 1. This means that the TL emission intensity I is directly proportional to R_{ex}.

$$I = cR_{ex} = c\, n\, s \exp\left(-\frac{E}{kT}\right), \quad (2.2)$$

where the temperature T can be expressed in terms of the linear heating rate β as $T = T_0 + \beta\, t$ and c is a constant representing the optical efficiency factor relating the luminescence output to the electron

release rate and the measuring instrument's efficiency to collect the light. The constant c influences only the intensity of the glow curve and it doesn't affect the characteristics like the shape of the glow curve and its decay pattern. Therefore its value can be taken to be unity.

Upon rearranging (2.2), we have [9],

$$\frac{dn}{n} = -s \exp\left(-\frac{E}{kT}\right) dt, \qquad (2.3)$$

Assuming linear heating rate i.e., $\frac{dT}{dt} = \beta\ ks^{-1}$, this equation may be written as,

$$\frac{dn}{n} = -\left(\frac{s}{\beta}\right) \exp\left(-\frac{E}{kT}\right), \qquad (2.4)$$

Integrating this equation, the value of n at any temperature T during the heating process is expressed as,

$$n = n_0 \exp\left(-\int_{T_0}^{T} \left(\frac{s}{\beta}\right) \exp\left(-\frac{E}{kT'}\right) dT'\right), \quad (2.5)$$

where n_0 is the initial concentration of trapped electrons and T_0 is the temperature at the beginning of the heating process. Substituting this expression for n in (2.2) we get the expression for TL intensity I(T), as a function of temperature T as,

$$I(T) = n_0\, s \exp\left(-\frac{E}{kT}\right) \exp\left[-\int_{T_0}^{T} \left(\frac{s}{\beta}\right) \exp\left(-\frac{E}{kT'}\right) dT'\right], \quad (2.6)$$

Equation (2.6) gives the expression of the glow curve. The integral in this equation can be expressed as,

$$\int \exp\left(-\frac{E}{kT}\right) dT = \exp\left(-\frac{E}{kT}\right) T + \frac{E \times \text{ExpIntegralEi}\left(-\frac{E}{kT}\right)}{k}, \qquad (2.7)$$

where $\text{ExpIntegralEi}\left(-\frac{E}{kT}\right)$ gives the exponential integral function $\text{Ei}\left(-\frac{E}{kT}\right)$.

The model proposed by RW for TL intensity was modified by Garlick and Gibson (GG) [10] using the same one trap and one recombination (OTOR) model. The assumption made by GG was that an electron which is de-trapped in to the conduction band from the trap centers after absorption of thermal energy may either recombine with a hole trapped at recombination center to produce luminescence or may be

re-trapped by any of the vacant traps. However, in RW model, re-trapping is ignored and the de-trapped electrons are assumed to recombine directly with the trapped holes emitting light. Using the probability coefficients for re-trapping and recombination A and A_r respectively, the recombination and re-trapping terms, respectively are proportional to $A_r n$ and $A\,(N - n)$, where N is the total number of the traps and n is the number of available recombination centers at any time. In the OTOR model n is also equal to the number of filled traps, so that the charge neutrality condition is maintained. The recombining fraction η of this combined probability of transitions for any excited carrier, then is,

$$\eta = \frac{A_r n}{A_r n + A\,(N - n)}, \qquad (2.8)$$

Garlick and Gibson (GG) assume that the excited charge carrier has no particular preference for recombination or retrapping which means $A_r = A$. Therefore, in contrast to the RW model in which the η value is equal to 1, the value of η in GG model becomes $\eta = \frac{n}{N}$. One can see that the TL intensity I(T) previously given by (2.2) would be modified by a factor equal to $\frac{n}{N}$. Thus, in GG model,

$$I(T) = -\frac{dn}{dt} = \left(\frac{n}{N}\right) n\, s \exp\left(-\frac{E}{kT}\right) = \left(\frac{n^2}{N}\right) s \exp\left(-\frac{E}{kT}\right), \quad (2.9)$$

Since the TL intensity I(T) is proportional to n^2 in GG model, it is called second order kinetics and discussed in detail in the next section. Again assuming linear heating rate $dt = \frac{dT}{\beta}$ and integrating (2.9) yields the value of n at any temperature T as,

$$n(T) = \frac{n_0}{1 + \frac{1}{N}\left(\frac{s}{\beta}\right) n_0 \int_{T_0}^{T} \exp\left(-\frac{E}{kT'}\right) dT'}, \qquad (2.10)$$

Plugging this equation in (2.8), one can get the following equation for glow curve [9],

$$I(T) = {n_0}^2 \frac{s}{N} \exp\left(-\frac{E}{kT}\right) \left[1 + \frac{n_0\, s}{\beta N} \int_{T_0}^{T} \exp\left(-\frac{E}{kT'}\right) dT'\right]^{-2} \quad (2.11)$$

It is worth to mention that, if $n \ll N$ (low dose sample) so that AN becomes much greater than $A_r n$, second order kinetics can be obtained in OTOR model even if $A_r \neq A$. Under this condition, $\eta = \frac{A_r n}{AN}$ and in (2.9), $\frac{n}{N}$ gets replaced by $\frac{A_r n}{AN}$ and in (2.9), $\frac{s}{N}$ gets replaced by $s\frac{A_r}{AN}$. Thus,

$$I(T) = {n_0}^2 \frac{sA_r}{NA} \exp\left(-\frac{E}{kT}\right) \left[1 + \frac{n_0\, sA_r}{\beta NA} \int_{T_0}^{T} \exp\left(-\frac{E}{kT'}\right) dT'\right]^{-2}, \qquad (2.12)$$

Therefore, it should be noted that in the case of $A_r \neq A$, the second order kinetics is obeyed only in low dose samples ($n \ll N$), whereas it is valid at all doses for the case when $A_r = A$.

2.2.2 The concept of kinetic order

The term order of kinetics or kinetic order in TL theory has been taken from chemistry. When the rate of a chemical reaction is directly proportional to the change in the concentration of only one of the reactant, it is called mono molecular kinetics or first order kinetics. If the rate of chemical reaction is directly proportional to the change in the concentration of both the reactants, it is called bi-molecular kinetics or second order kinetics [11].

In TL phenomena, first order kinetics means electron re-trapping is assumed to be zero and the TL intensity I at any temperature T during heating depends only on the concentration n of electrons in the active traps at that temperature [11]. Randall and Wilkins showed that a TL peak resulting from a single electron trapping state and a single kind of recombination center results in first-order kinetics if one assumes no re-trapping of the released electrons. The equation governing this process was shown in (2.3). The assumption of no re-trapping resulting in this equation made RW model a ‘ classical’ first order case among researchers dealing with TL, though in some cases the physical situation of ‘negligible re-trapping’ has been termed first order kinetics.

In addition to the concentration of electrons n in traps, if the values of the TL intensity are dependent also on the concentration h of the recombination centers, it becomes a case of non-first order kinetics. Some early investigators of TL phenomena said that ‘if the probability of re-trapping before recombination is non-zero, we have second-order kinetics’. For OTOR case in GG model, when $A_r = A$ and the concentration h of recombination center is equal to the concentration n of electrons in traps (so that the over-all charge neutrality condition is satisfied), it becomes a case of second order kinetics. Under the condition $A_r = A$, the ‘reaction’ rate between the released charges from the traps and the

recombination center becomes equal to n^2 (as shown in equation (2.9) which means we have kinetic order equal to 2. But when $A_r \neq A$, a value of kinetic order between 1 and 2 is obtained instead of being exactly equal to 2. Therefore, though a chemical reaction can be described in terms of first order or second order kinetics in chemical kinetics, all values of the kinetic order between 1 and 2 are also possible in TL phenomena. Such cases do not fit in to first order or second order kinetics and are called general order kinetics and it was first suggested by May and Partridge (MP) [9, 12]. They proposed the following expression for TL intensity with intention to provide a general expression for TL emission which would satisfy not only the first order and second order kinetics expressions when b = 1 and b = 2 respectively, but would also include all other possible values of b including its non-integral values between 1 and 2 or even outside this range.

$$I(T) = -\frac{dn}{dt} = s' n^b \exp\left(-\frac{E}{kT}\right) \quad (2.13)$$

where s' and b are the empirical constants called frequency factor and the order of kinetics, respectively. Therefore, this expression for TL intensity is called general order kinetics. Though equation (2.13) is based on OTOR model, there is a general practice of applying it to any experimental glow peak to do kinetic analysis. This is under the assumption that it includes all plausible physical schemes that may be applicable to the glow peaks. Solving this expression gives the following temperature dependent equation for the TL glow peak,

$$I(T) = {n_0}^b s' \exp\left(-\frac{E}{kT}\right)\left[1 + \frac{(b-1){n_0}^{b-1}s'}{\beta}\int_{T_0}^{T} \exp\left(-\frac{E}{kT'}\right)dT'\right]^{-\frac{b}{b-1}} \quad (2.14)$$

This equation was simplified by Chen [13] under the assumption that ${n_0}^{b-1}s' = s$. The role of ${n_0}^{b-1}s'$ was assumed to be similar to that of the frequency factor in the first order kinetics mainly because of the fact that it has the dimension s^{-1} like the frequency factor. However, to avoid confusion, later workers have designated it as s'' instead of s. Therefore, equation (2.14) becomes,

$$I(T) = n_0\, s'' \exp\left(-\frac{E}{kT}\right)\left[1 + \frac{(b-1)s''}{\beta}\int_{T_0}^{T} \exp\left(-\frac{E}{kT'}\right)dT'\right]^{-\frac{b}{b-1}} \quad (2.15)$$

Increased value of b implies greater degree of re-trapping which is found to raise the value of the temperature T_M corresponding to the maximum intensity.

2.3 Photoluminescence

As discussed above, an electron in a semiconductor or insulator is excited to a higher energy quantum state upon absorption of external energy from electromagnetic radiation. If the electron returns (relaxes) to a lower energy quantum state by radiating a photon, the process is called photoluminescence (PL) [14-15]. In other words, photoluminescence is the process in which a substance absorbs photons and radiates photons back out. Quantum mechanically, this can be described as an excitation to a higher energy state and then a return to a lower energy state accompanied by the emission of photon.

Upon absorption of an ultraviolet or visible photon, valence electrons will be promoted from ground state to an excited state. The electron spin will be conserved during this excitation process. For example, as shown in Figure 2.1(a), a pair of electrons occupying the same electronic ground state has opposite spins and are said to be in a singlet spin state. But one of the electrons will be promoted to a singlet excited state following absorption of energy from incident photon (Figure 2.1(b)).

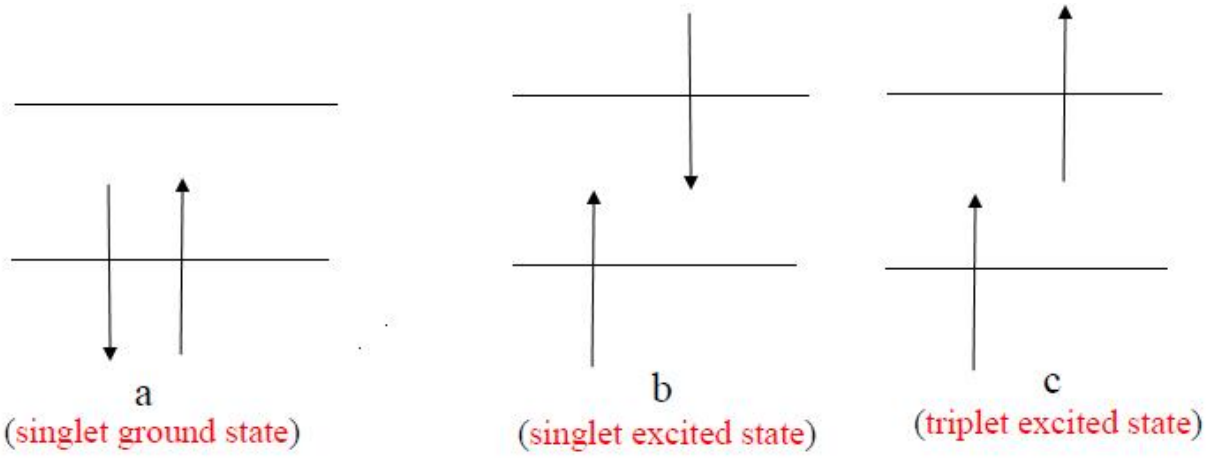

Fig. 2.1: The ground and excited states of a molecule [16].

This phenomenon is called “excitation”. However, in a triplet state, the excited electron has the same spin with the ground state electron and they are now no longer paired. Since excitation to a triplet state involves an additional spin transition, it is more probable that an excited singlet will form upon absorption of a photon. Because they are not stable, the excited states will not stay indefinitely. At some random moment, a molecule in the excited state will spontaneously return to the ground state by giving off some energy in the form of electromagnetic radiation. This return process is called decay,

deactivation or relaxation. As mentioned, the energy absorbed during the excitation process can be released during the relaxation in the form of a photon. This type of relaxation is called emission and it can be divided into fluorescence and phosphorescence. Though these two types of emission are discussed under section 2.1, it is important to illustrate in detail their mechanism.

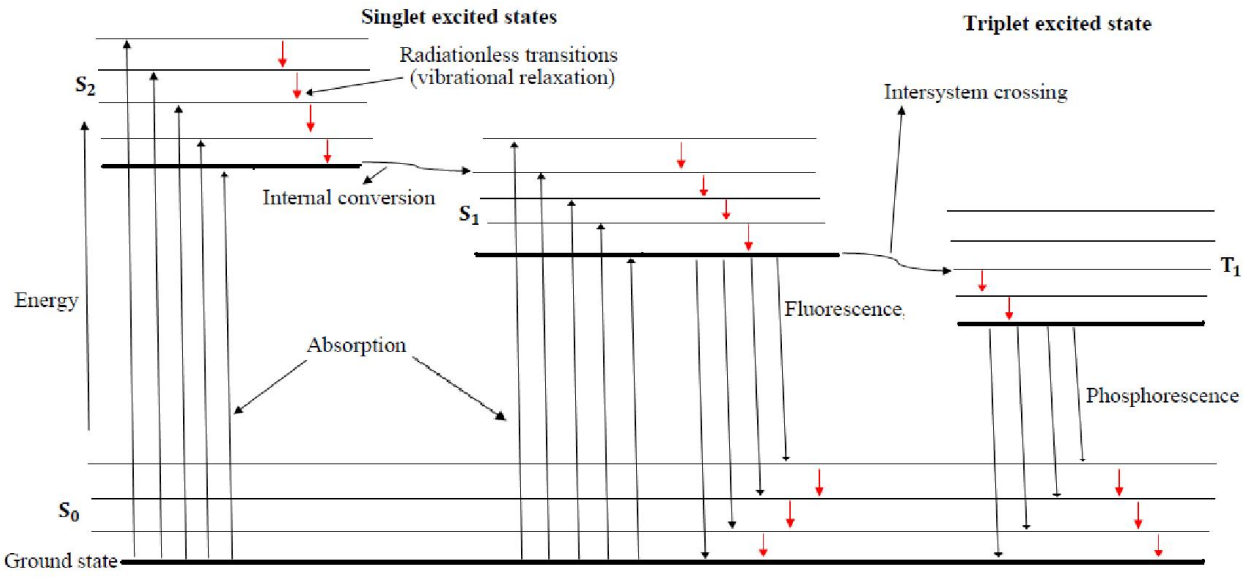

Fig. 2.2: Energy diagram for PL mechanism (Jablonski diagram) [17]

A given molecule in the excited state has several options to decay or relax to the ground state. The ground state, which is shown in Figure 2.2, is a singlet state labeled S_0. By absorption of a photon of correct energy, the molecule will be excited to one of several vibrational energy levels in the first excited electronic state, S_1, or the second electronic excited state, S_2. It is important to note that both S_1 and S_2 are singlet states. As shown in Figure 2.2, relaxation to the ground state from these excited states can be radiationless or involve the emission of a photon. Radiationless transition is a mechanism in which no photons are emitted. There are different forms of radiationless transitions. One form is vibrational relaxation**,** in which a molecule in an excited vibrational energy level loses energy as it moves to a lower vibrational energy level in the same electronic state. This process is very rapid, with the molecule's average lifetime in an excited vibrational energy level being $10^{-14} - 10^{-13}$ s [18]. Thus, because of their short life time, molecules that are excited to different vibrational energy levels of the same excited electronic state quickly return to the lowest vibrational energy level of the same excited state. Another form of radiationless relaxation involves internal conversion**.** In this process, a molecule in the ground vibrational level of an excited electronic state passes directly into a high vibrational energy

level of lower energy electronic state of the same spin state [19]. This is indicated as transitions from S_2 to S_1 in Figure 2.2. Therefore, a molecule in an excited electronic state may return or relaxes to the ground electronic state without emitting a photon by undergoing internal conversions and vibrational relaxations. A final form of radiationless relaxation is an intersystem crossing in which a molecule in the ground vibrational energy level of an excited electronic state passes into a high vibrational energy level of a lower energy electronic energy state with a different spin state. This process is shown as transitions from S_1 to T_1 in Figure 2.2.

Therefore, in terms of these transitions, fluorescence occurs when a molecule in the lowest vibrational energy level of an excited electronic state returns to a lower energy electronic state by emitting a photon. Because of the fact that molecules return to their ground state by the fastest possible mechanism, fluorescence is only observed if it is a more efficient means of relaxation than the combination of internal conversion and vibrational relaxation. One particular property of fluorescence emission of photons is that it stops immediately when excitation is cut off. Moreover, in the process of fluorescence the involvement of traps is not important; but there may be many luminescent centers.

Intersystem crossing is a more efficient method of populating triplet states from the lowest singlet excited states in many molecules and it is spin dependent internal conversion process. Otherwise, population of triplet states by direct absorption from the ground state is highly unlikely. The mechanism for intersystem crossing involves vibrational transitions between the excited singlet state and a triplet state and this is transition from S_1 to T_1 as shown in Figure 2.2. Once intersystem crossing has occurred, the molecule undergoes the usual internal conversion process and falls to the lowest vibrational level of the triplet state. A radiative transition between the lowest triplet state and the ground state then takes place. This emission is called phosphorescence [19]. Therefore, phosphorescence is even rarer than fluorescence, since a molecule in the triplet state has a good chance of undergoing intersystem crossing to ground state before phosphorescence can occur.

2.4 Cathodoluminescence

Cathodoluminescence (CL), a technique which has been conventionally used to investigate some characteristics of specimens, such as trace impurities and lattice defects, as well as to investigate crystal distortion, occurs due to the emission of light during electron irradiation [20-22]. In the beginning of the last century it was observed that invisible cathode rays produced by electrical discharges in the evacuated tubes, produced light when they struck the glass walls of the tube. The modern name for

cathode rays is electrons and this type of luminescence has retained the name CL. This is a very useful form of luminescence. Beams of electrons are used for many purposes. The electron microscope employs beams of electrons to produce high resolution images of small specimens. In some cases, the beam produces CL from the specimen. This is particularly useful for the study of minerals in rocks where the presence of transition metal trace elements can cause the mineral to give off a distinctive color light. The screens of cathode ray tubes and earlier version of televisions glow by this kind of emission [1]. In cathode ray tubes, zinc and cadmium sulfide phosphors are used. Production of phosphors for TV screens is a very specialized technique, which requires variety of colors and their appropriate persistence to smoothen out the flicker of the scan.

2.4.1 Mechanism of Cathodoluminescence

When a beam of energetic electrons, such as from a scanning electron microscope (SEM), impinges on a sample, the energy of the primary beam is partitioned in various ways. Some of the energy is converted into x-rays; some appears as backscattered electrons of relatively high energy, some as secondary electrons of much smaller energies, and some as Auger-process electrons, also of small energies. Much of the energy is absorbed and transferred to generation of phonons, with consequent release of heat.

A little of the total energy carried in the beam acts to promote non-localized electrons from the valence band to the conduction band, leaving holes behind in the valence band. That is, the electrons go from the ground state to an excited state. Even a small amount of the total energy applied to the valence band may be sufficient to promote many electrons into the conduction band. After a short time, these promoted electrons undergo de-excitation and return to a lower-energy state, moving randomly through the crystal structure until they encounter a trap. Electrons remain in traps only a very short time before vacating the traps, with concomitant emission of photons, and return to the ground state in the valence band. Electrons may encounter a single trap or multiple traps at they move through the band gap. The presence of these traps, at discrete energy levels within the band gap, is a precondition for emission of photons (CL) in the visible light range. If no traps are present, electrons fall directly back to the valence band and emit photons with wavelengths in the near ultraviolet. Residence times of electrons in traps are variable; however, most traps empty rapidly, on a timescale of microseconds. Those traps that empty promptly, producing photons with energies in the near-UV and visible portions of the electromagnetic spectrum, are the basis for CL. The greater the number of electron traps present in a crystal the greater will be the number of CL emissions in the visible range.

2.5 Structural and electronic properties of some selected phosphors

2.5.1 Definition of phosphor

The word phosphor was invented in the early 17th century and its meaning remains unchanged till today. Early alchemists found a heavy crystalline stone with a gloss at the foot of a volcano, and fired it in a charcoal oven intending to convert it to a noble metal. They found that the sintered stone emitted red light in the dark after exposure to sunlight rather than being converted in to metal. After this discovery, similar findings were reported from many places in Europe, and these light-emitting stones were named phosphors [23]. This word means "light bearer" in Greek. In other words, a phosphor emits energy from an excited electron as a light. In general, the excitation of electron is caused by absorption of energy from an external source such as another electron, a photon, or an electric field.

Phosphors have wide applications in today's science and technology. The applications of phosphors can be classified as light sources represented by fluorescent lamps, display devices represented by cathode-ray tubes, detector systems represented by x-ray screens and scintillators, and other simple applications such as luminous paint with long persistent phosphorescence [24]. Therefore, designing a phosphor for a particular application requires the understanding of the properties of the constituents of the phosphor. In addition to the host material (insulator or semiconductor), inorganic phosphors consist of impurities (dopants or activators) purposely incorporated in small amounts in to the host [25]. The luminescence emission from a given phosphor depends on many factors. In general, a phosphor with high luminescence efficiency is characterized by properties such as low phonon energy, high optical damage threshold, high quantum efficiency, stability, etc.

In this research work, interesting fluoride and silicate phosphors have been investigated for possible applications in display medium and TL dosimetry. These phosphors are Ho^{3+}doped $KY_3F_{10}$and Ce^{3+} doped $Y_2SiO_5$and are discussed in detail in the following sections.

2.5.2 Properties of KY_3F_{10}: Ho^{3+}phosphor

The KY_3F_{10} crystal has a cubic structure (space group Fm3m). The basic building unit consists of the two ionic groups $[KY_3F_8]^{2+}$and $[KY_3F_{12}]^{2-}$, which alternate along the three crystallographic directions [26-27] as shown in Figure 2.3. In the first group, the fluorine atoms form an empty cube. In the second unit, they form an empty cuboctahedron.

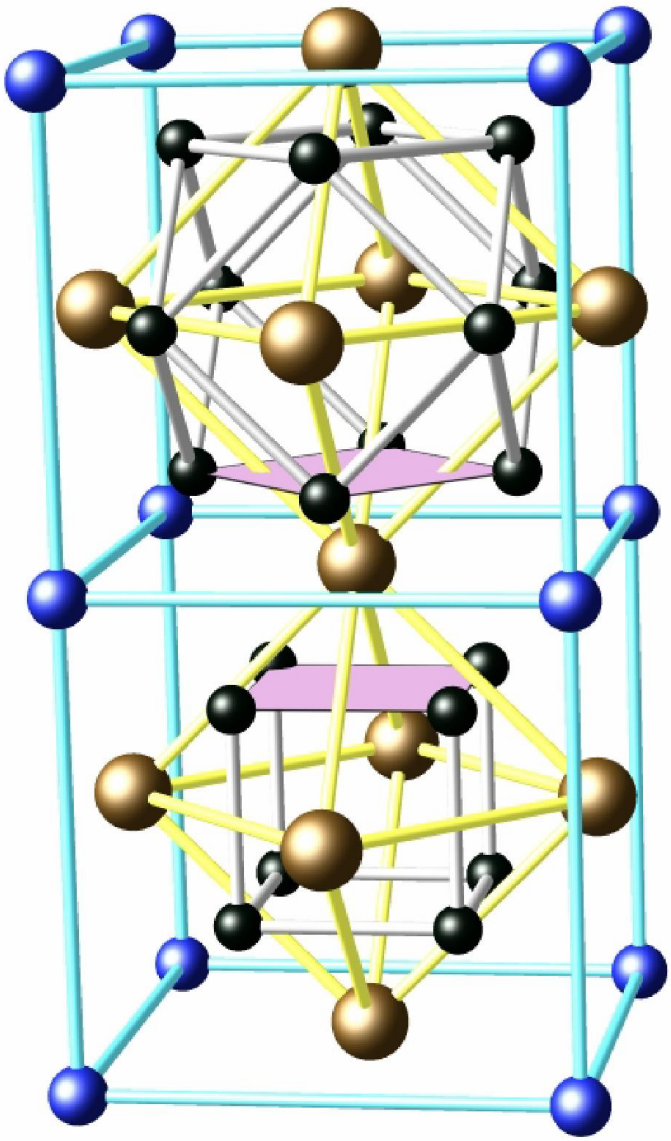

Fig. 2.3: The unit cell of the Fm3m structure of KY_3F_{10}. The biggest bronze (grey) spheres substitute for yttrium atoms, the blue (grey) ones for potassium atoms, and the black ones for fluorine atoms. The nearest surrounding of yttrium ions is represented by eight fluorine ions forming a square antiprism with the C_{4v} point symmetry group [38].

This structure could alternatively be described in terms of clusters of octahedrally arranged yttrium-centered square antiprisms YF_8 which share corners and edges to generate the fluorine cubes and cuboctahedra as shown in Figure 2.4 [28]. The potassium atoms are coordinated to 4 fluorine atoms at the distance 2.765 Å and to 12 fluorine atoms at the distance 3.200 Å. The 12 fluorine atoms form truncated tetrahedra. The additional four fluorine atoms are located nearby the hexagonal faces forming Friauf polyhedra KF_{16}.

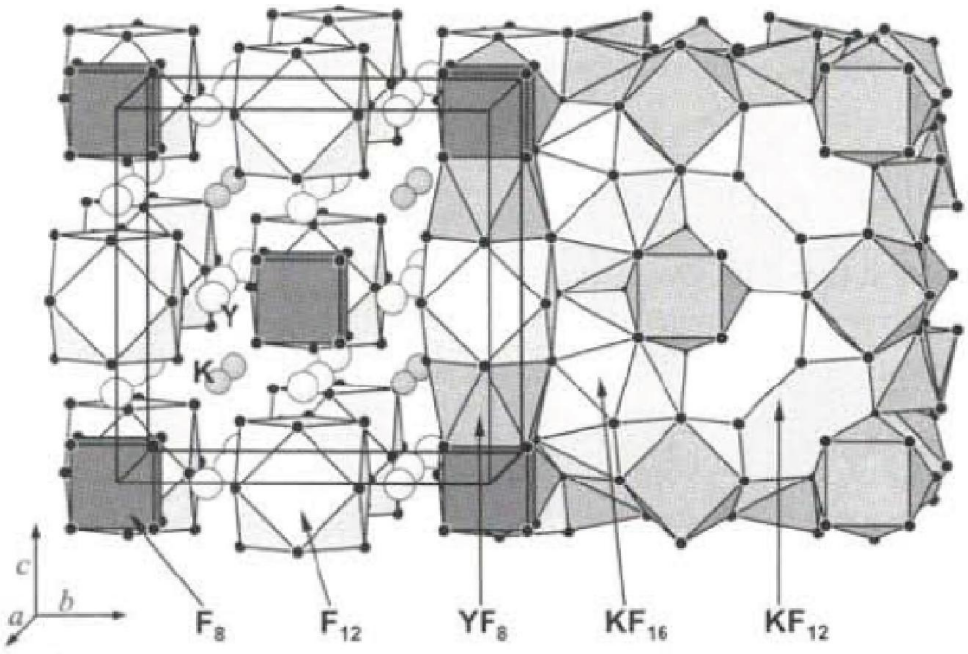

Fig. 2.4: Structural composition of KY_3F_{10} [27].

KY_3F_{10} crystal was grown for the very first time in 1971 [29]; and since then, it appears to be a very attractive materials because it is fairly easy to grow. Two synthesis methods, namely, the Czochralsky pulling technique [30], and Bridgman–Stockbarger method [31] are commonly used as growing mechanisms.

Upon doping this crystal with rare earth ions, these ions predominantly occupy yttrium positions. Each rare earth ion is surrounded by eight fluorine ions forming a square antiprism with the C_{4v} point symmetry group (see Fig. 2.3, the distances between Y^{3+} ion and F^- ions at the corners of the two squares, normal to the C_4 symmetry axis and rotated by the angle of $\pi/4$ relative to one another, is equal to 0.2352 and 0.2202 nm) [32]. There are three equivalent rare earth centers oriented along three different C_4 axes of the cubic lattice structure. The compound is chemically and thermally stable, transparent, and isotropic. Once doped with rare earth ions, it has received much attention since it is suitable to build solid state lasers [33-34], white-light emitters [35-36] and quantum cutting systems to enhance solar cells efficiency [37].

Table 2.2: Summary of crystallographic properties of KY_3F_{10}

Structure	Tetragonal
Space group	Fm3m
Cell parameters	$a = 8.161\ \mathring{A},\ \ c = 11.53\ \mathring{A}$
Number of elements by cell	8
Anisotropy	Isotropic
Melting point	990°C

2.5.3 Properties of $Y_2SiO_5:Ce^{3+}$ phosphor

The structure of Y_2SiO_5 contains isolated SiO4 tetrahedral and nonsilicon-bonded oxygen. Two different monoclinic structures have been found, a low temperature phase (X_1) and high temperature phase (X_2).

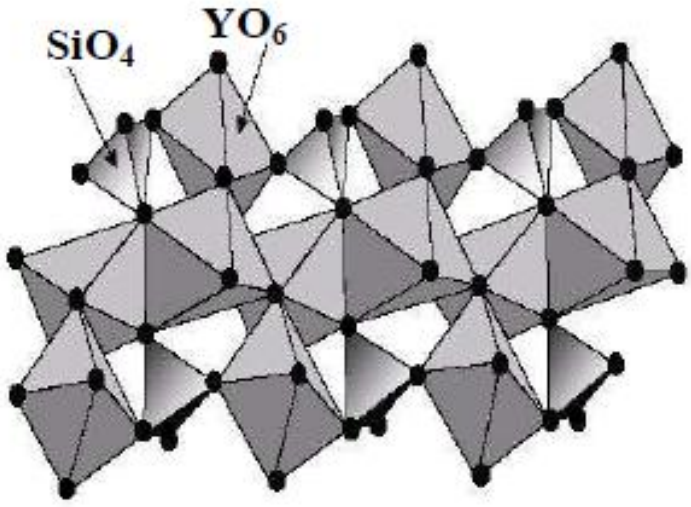

Fig. 2.5: Schematic structure of Y_2SiO_5[39].

The X_1 phase has the space group $P2_1/c$, whereas the space group B2/c is assigned to the X_2 phase. Both X_1 and X_2 phases have two different Y^{3+} sites, the coordination numbers of which are 7 and 9 for the X_1 phase and 6 and 7 for the X_2 phase [39-42] During the preparation method of $Y_2SiO_5:Ce$, the activator Ce^{3+} (radius of 0.106 nm) can easily substitute Y^{3+} (radius of 0.093 nm) thus also resulting in the two different crystallographic sites. The notation A_1 and A_2 are given to the two sites in the X_1 - phase with coordination number (CN) of 9 and 7. B_1 and B_2 are denoted to the X_2 - phase with CN of 6 and 7 [39]. A_1 with the CN of 9 means that there are 8 oxygen atoms bonded to yttrium and silicon and only one that is bonded to only yttrium and CN of 7 means that 4 oxygen atoms are bonded to yttrium and silicon and 3 are

bonded to yttrium only. Both B_1 and B_2 have two oxygen atoms that are only bonded to yttrium [39]. Y_2SiO_5 has a wide band gap of about 7.4 eV (insulator) so doping it with an activator such as Ce creates an energy level structure inside the wide band gap. The complicated monoclinic crystal structure of Y_2SiO_5 is formed from the SiO_4 and YO_6 tetra- and octahedron structures as shown in Figure 2.5.

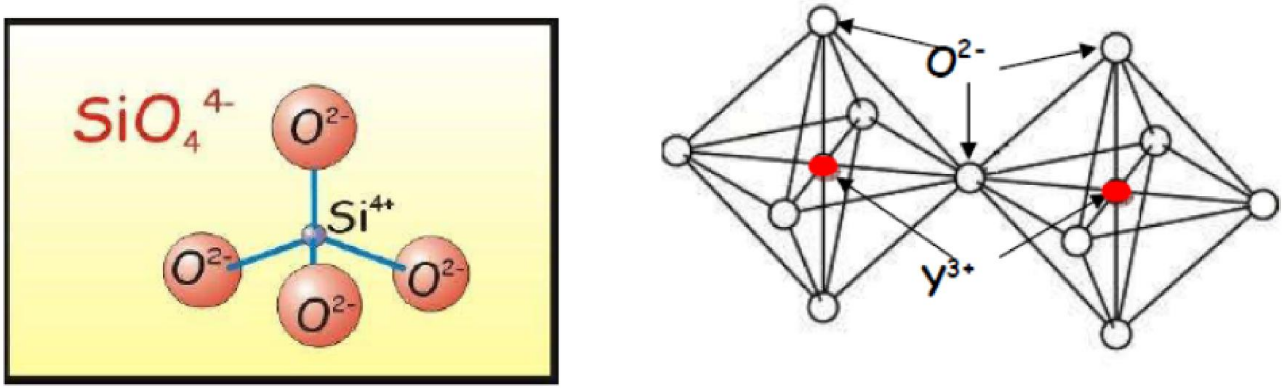

Fig. 2.6: Schematic diagrams illustrating the SiO_4 and YO_6 tetra- and octahedron structures of Y_2SiO_5 [39].

2.6 Crystal Field Theory (CFT)

Crystal field theory is a model that describes the interaction between a central metal ion that is surrounded by anions (ligands) in a crystal [43]. In crystalline field theory, the valence electrons belong to ion A and the effect of the lattice is considered through the electrostatic field created by the surrounding B ions at the A position. This electrostatic field is called the crystalline field. It is then assumed that the valence electrons are localized in ion A and that the charge of B ions does not penetrate into the region occupied by these valence electrons. Thus the Hamiltonian can be written as [44],

$$H = H_{FI} + H_{CF} \qquad (2.16)$$

where H_{FI} is the Hamiltonian related to the free ion A (an ideal situation in which the A ions are isolated, similar to a gas phase of these ions) and H_{CF} is the crystal field Hamiltonian, which accounts for the interaction of the valence electrons of A with the electrostatic crystal field created by the B ions. In order to apply quantum mechanical perturbation theory, the free ion term is usually written as [44],

$$H_{FI} = H_0 + H_{ee} + H_{SO} \qquad (2.17)$$

where H_0 is the central field Hamiltonian (a term that reflects the electric field acting on the valence electrons due to the nucleus and the inner- and outer-shell electrons), H_{ee} is a term that takes into account any perturbation due to the Coulomb interactions among the outer (valence) electrons, and H_{SO} represents the spin–orbit interaction summed over these electrons. Depending upon the size of the

crystal field term H_{CF} in comparison to these three free ion terms, different approaches can be considered to the solution of Equation (2.17) by perturbation methods:

- Weak crystalline field: $H_{CF} \ll H_{SO},\ H_{ee}, H_0$. In this case, the energy levels of the free ion A are only slightly perturbed (shifted and split) by the crystalline field. The free ion wavefunctions are then used as basis functions to apply perturbation theory, H_{CF} being the perturbation Hamiltonian over the $^{2S+1}L_J$ states (where S and L are the spin and orbital angular momenta and J = L + S). This approach is generally applied to describe the energy levels of trivalent rare earth ions, since for these ions the 4f valence electrons are screened by the outer $5s^2\ 5p^6$ electrons. These electrons partially shield the crystalline field created by the B ions.
- Intermediate crystalline field: $H_{SO} \ll H_{CF} < H_{ee}$. In this case, the crystalline field is stronger than the spin–orbit interaction, but it is still less important than the interaction between the valence electrons. Here, the crystalline field is considered a perturbation on the ^{2S+1}L terms. This approach is applied for transition metal ion centers in some crystals.
- Strong crystalline field: $H_{SO} < H_{ee} < H_{CF}$. In this approach, the crystalline field term dominates over both the spin–orbit and the electron–electron interactions. This applies to transition metal ions in some crystalline environments.

2.7 Rare Earth Ions

The rare earth (RE) ions most commonly used for applications as phosphors, lasers, and amplifiers are the so-called lanthanide ions. Lanthanide ions are formed by ionization of a number of atoms located in periodic table after lanthanum: from the cerium atom (atomic number 58), which has an outer electronic configuration $5s^2\ 5p^6\ 5d^1\ 4f^1\ 6s^2$, to the ytterbium atom (atomic number 70), with an outer electronic configuration $5s^2\ 5p^6\ 4f^{14}\ 6s^2$. These atoms are usually incorporated in crystals as divalent or trivalent cations. In trivalent ions 5d, 6s, and some 4f electrons are removed and so RE^{3+} ions deal with transitions between electronic energy sublevels of the $4f^n$ electronic configuration [45-46]. Divalent lanthanide ions contain one more f electron (for instance, the Eu^{2+} ion has the same electronic configuration as the Gd^{3+} ion, the next element in the periodic table) but, at variance with trivalent ions, they tend to show the f→d interconfigurational optical transitions [45-46].

2.7.1 Trivalent rare Earth Ions and the Dieke Diagram

Trivalent lanthanide ions have an outer electronic configuration $5s^2\ 5p^6\ 4f^n$, where n varies from 1 (Ce^{3+}) to 13 (Yb^{3+}) and indicates the number of electrons in the unfilled 4f shell. The $4f^n$ electrons are, in fact, the valence electrons that are responsible for the optical transitions. Table 2.3 gives the number of 4f valence electrons for each trivalent rare earth ion of the lanthanide series. These valence electrons are shielded by the 5s and 5p outer electrons of the $5s^2\ 5p^6$ less energetic configurations. Because of this shielding effect, the valence electrons of trivalent rare earth ions are weakly affected by the ligand ions in crystals; a situation that corresponds to the case of a weak crystalline field, which was discussed in the previous section (section 2.6). Consequently, the spin–orbit interaction term of the free ion Hamiltonian is dominant over the crystalline field Hamiltonian term. This causes the $^{2S+l}L_J$ states of the RE^{3+} ions to be slightly perturbed when these ions are incorporated in crystals [47]. The effect of the crystal field is to produce a slight shift in the energy of these states and to cause additional level splitting.

Table 2.3: The number of 4f electrons (n) in trivalent lanthanide ions.

Ion	n
Ce^{3+}	1
Pr^{3+}	2
Nd^{3+}	3
Pm^{3+}	4
Sm^{3+}	5
Eu^{3+}	6
Gd^{3+}	7
Tb^{3+}	8
Dy^{3+}	9
Ho^{3+}	10
Er^{3+}	11
Tm^{3+}	12
Yb^{3+}	13

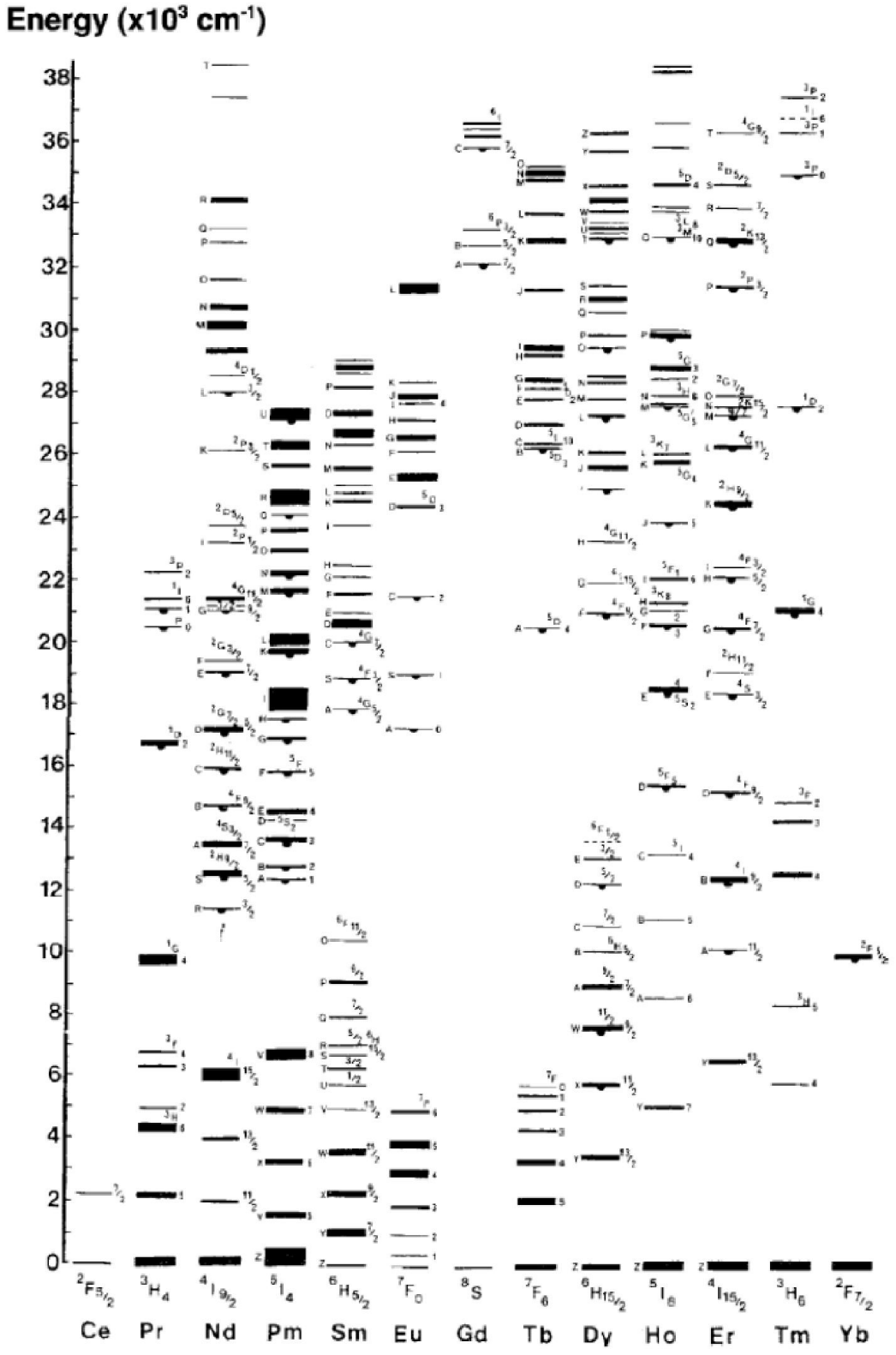

Fig. 2.7: An energy level diagram for trivalent lanthanide rare earth ions (Dieke diagram) [47].

However, the amount of this shift and the splitting energy are much smaller than the spin–orbit splitting, and thus, the optical spectra of RE^{3+} ions are fairly similar to those expected for free ions. Moreover, this implies that the main features of RE^{3+} ion spectra are similar from one crystal to another. In fact, the interpretation of the absorption and luminescence spectra of lanthanide RE^{3+} ions in crystals is based on systematic spectral measurements made in a particular host, lanthanum chloride ($LaCl_3$) [47]. These spectra were obtained by Dieke and co-workers (1968) and provide a famous energy-level diagram, the so-called Dieke diagram, shown in Fig. 2.7. This diagram shows the energy of the $^{2S+1}L_J$ states for the RE^{3+} ions in $LaCl_3$. The width of each state indicates the magnitude of the crystal field splitting, while the center of gravity of each multiplet gives the approximate location of its corresponding free ion $^{2S+1}L_J$ energy level.

Of course, the energy splitting and center of gravity of the $^{2S+1}L_J$ energy levels for RE^{3+} ion can change slightly when it is incorporated into crystals other than $LaCl_3$, but the gross features of its energy-level diagram remain unchanged. According to its degeneracy, the maximum number of split components for each $^{2S+1}L_J$ multiplet is (2J + 1) for integer J, or $(J + \frac{1}{2})$ for half-integer J. The Dieke diagram provides very useful information with which to predict and/or to make a proper assignment of the emission spectra corresponding to trivalent rare earth ions in crystals.

2.7.2 Divalent Rare Earth Ions

Divalent rare earth ions also have an outer electronic configuration of $4f^n$ (n including one more electron than for the equivalent trivalent rare earth). However, unlike that of RE^{3+} ions, the $4f^{(n-1)}5d$ excited configuration of divalent rare earth ions is not far from the $4f^n$ fundamental configuration. As a result, $4f^n \rightarrow 4f^{(n-1)}5d$ transitions can possibly occur in the optical range for divalent rare earth ions [45-46]. They lead to intense (parity-allowed transitions) and broad absorption and emission bands.

2.8. Optical transitions in Ce^{3+} and Ho^{3+} ions

The present study focuses on developing $Ce^{3+}$and Ho^{3+} doped silicate and fluoride phosphors and thin films synthesized by different techniques and investigate their structural and luminescence properties, it is important to briefly study the optical transitions of these ions.

2.8.1. Optical transitions in Ce^{3+} ion

Cerium (Ce) is one of the rare earth elements in the lanthanide group with electronic configuration [Xe] $4f^1\ 5d^1\ 6s^2$. As discussed above, the $4f^n$ energy levels are completely shielded by the filled $5p^6$ and $5s^2$ shells and hence, they are not affected by the host environment. However, an electron in a 5d orbital is not completely shielded and its energy is very susceptible to changes in the crystalline environment. Therefore, the $5d^1$ level strongly interacts with the host lattice due to the large spatial field of the 5d wave-function and the crystal field splitting dominates over the split spin-orbit interaction [43]. Hence, emission transition is an allowed one since the 5d-4f transition is parity and spin allowed/electric dipole allowed. As a consequence, the emitting level has a short life time, a common property in certain phosphors. Emission observed from cerium differs greatly with the type of host material.

2.8.2. Optical transitions in Ho^{3+} ion

Holmium (Ho) is also one of the rare earth elements in the lanthanide group with electronic configuration [Xe] $4f^{11}\ 6s^2$. It is well known that Ho ions can produce laser emission in the 2 and 2.9 μm ranges [1–4] arising from transitions between Stark levels of the $^5I_7$ and $^5I_6$ states and the $^5I_8$ ground state. As can be seen from the energy level diagram of trivalent holmium (Ho^{3+}) shown below, this ion has also several high lying metastable levels giving rise to transitions at various wavelengths from infrared (IR) to ultraviolet (UV) region.

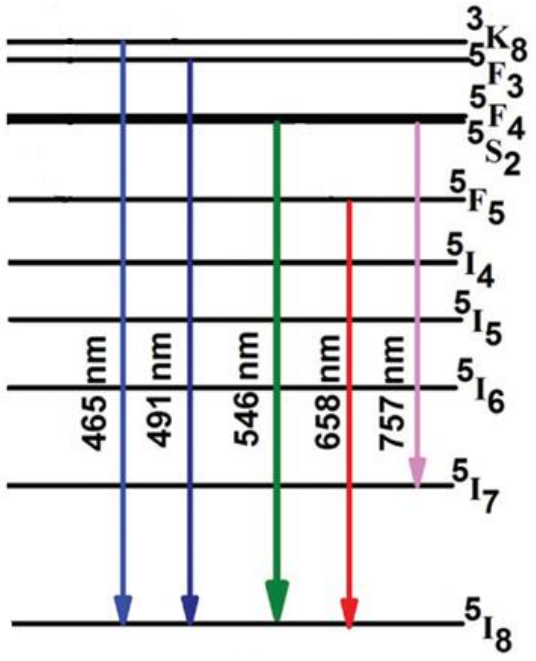

Fig. 2.8: Energy level diagram of Ho^{3+} with possible transitions [48].

References

[1] C. M. Sunta, Unravelling Thermoluminescence, Springer, London, 2015.

[2] S.W.S. McKeever, Thermoluminescence of solids, Cambridge Solid State Science Series, Oklahoma State University, 1988.

[3] V. Pagonis, G. Kitis and C. Furetta, Numerical and Practical Exercises in Thermoluminecsnce, Springer, USA, 2006.

[4] R. Ye and A. Barron, Photoluminescence Spectroscopy and its Applications, SPIE, USA, 2011.

[5] C. Furetta, Handbook of Thermoluminescence, 2003, World Scientific, Italy.

[6] M. Martini, F. Meinardi, F. Riv. Nuovo Cim. 20, 1(1997).

[7] A. Akin, E. Ekdal, Y. Arslanlar, M. Ayvacikli, T. Karali, N. Can, Luminescence, 30, 830 (2014).

[8] J.T. Randall, M.H.F. Wilkins, Proc. Roy. Soc. (London) ser. A, 184, 365 (1945).

[9] C. Furetta, S.Guzman, B.Ruiz, E.Cruz-Zaragoza, Applied Radiation and Isotopes 69, 346 (2011).

[10] G. Garlick, A.F. Gibson, Proc. Phys. Soc (London) 60, 574 (1948).

[11] R. Chen, J. Phys. D: Appl. Phys. 16, 107 (1983).

[12] C.E. May, J.A. Partridge, J. Chem. Phys. 40, 1401 (1964).

[13] R. Chen, J. Electrochem. Soc. (Solid State Sci.) 116, 1254 (1969).

[14] S. Tripathy, R. K. Soni, S. K. Ghoshal and K. P. Jain, Bull. Mater. Sci. 24, 285 (2005).

[15] Z. Zhou, M. Steigeward, R.. Frienser, and L. Brus, Phys. Rev. B 71, 1 (2005).

[16] C. P. Schaller, Electronic Spectroscopy: Theory, Saint John's University, USA, 2016.

[17] A. Abdel Shafi, D. Worrall, J. Photochem. Photobiol. A: Chemistry 172, 170 (2005).

[18] H. H. Jaffe, Albert L. Miller, J. Chem. Educ. 43, 469 (1966).

[19] IUPAC, Compendium of Chemical Terminology, 2nd ed. (the "Gold Book") (1997).

[20] K. T. Hillie and H. C. Swart, Appl. Surf. Sci, 183, 304 (2001).

[21] L. Oosthuizen, H. C. Swart, P. E. Viljoen, P. H. Holloway and G. L. P. Berning, Appl. Surf. Sci, 120, 9 (1997).

[22] S. H. Shin, J. H. Kang, D. Y. Jeon and D. S. Zang, J. Solid State Chem, 178, 2205 (2005).

[23] S. Shionoya, W. Yen, H. Yamamoto, Phosphor handbook (second edition), CRC Press, New York, 2007.

[24] X. Zhang, W. Liu, G. Wei, D. Banerjee, J. Li, Am. Chem. Soc., 136, 14230 (2014).

[25] W. Yen and M. Weber, Inorganic phosphors compositions, Preparation and optical properties, CRC Press, London, 2004.
[26] J. W. Pierce and Y.-P. Hong, in Proceedings of the Tenth Rare Earth Research Conference, Springfield, 1973.
[27] A. Grzechnik, J. Nuss, K. Friese, J. Gesland, M. Jansen, Z. Christalloger. NCS 217, 1 (2002).
[28] D. Bevan, S. Lawton, Acta Crystallogr. B42, 55 (1986).
[29] M.P. Borzenkova, G.N. Kuznetsova, A.V. Novoselova: Inorg. Mater. 7, 214 (1971).
[30] A. Braud, P.Y. Tigreat, J. L. Doualan, R. Moncorg, Appl. Phys. B 72, 909 (2001).
[31] E. Chukalina, D. Pytalev, M. Popova, Phy. Lett. A 375, 3205 (2011).
[32] K. Friese H. Kruger, V. Kahlnberg, T. Zunic, H. Emerich, J. Gesland, A. Grzechnik, J. Phys.: Condens. Matter 18, 2677 (2006).
[33] P. Camy, J. L. Doualan, R. Moncorgé, J. Bengoechea, and U. Weichmann, Opt. Lett. 32, 1462 (2007).
[34] Y. Dong, S. T. Li, and X. H. Zhang, Laser Phys. Lett. 9, 116 (2012).
[35] A. Toncelli, L. Bonelli, R. Faoro, D. Parisi, and M. Tonelli, Opt. Mater. 31, 1205 (2009).
[36] T. Pang, W. Cao, M. Xing, X. Luo, X. Yang, Opt. Mater. 33, 485 (2011).
[37] D. Serrano, A. Braud, J. Doualana, P. Camy, A. Benayad, V. Menard, R. Moncorge, Opt. Mater. 33, 1028 (2011).
[38] M. Hehlen, Proc. SPIE 7614, 761404 (2010).
[39] E. Coetsee, Luminescent properties of Y_2SiO_5:Ce thin films, PhD Thesis, University of the Free State, 2010.
[40] J. Felsche, Struct. Bonding (Berlin), 13, 99 (1973).
[41] K. Liddell and D. P. Thompson, Br. Ceram. Trans., 85, 17 (1986).
[42] J. Wang, S. Tian, G. Li, F. Liao, and X. Jing, Mater. Res. Bull., 36, 1855 (2001).
[43] A. H. Wako, Tailoring luminescence properties of RE doped Aluminate and Garnet Phosphors, PhD Thesis, University of the Free State, 2015.
[44] G. Newman and N. Betty, Crystal Field Handbook, Cambridge University Press, London, 2007.
[45] S. Zhou, J. Lumin. 118, 179 (2006).
[46] C. W. Thiel, Y. Sune, R. L. Cone, J. Mod. Opt. 49, 2399 (2002).
[47] S. V.E Eliseeva, J. C. G. Bunzli, Chem. Soc. Rev. 39, 189 (210).
[48] A. Pandey and V. K. Rai, Dalton Trans. 42, 11005 (2013).

Chapter 3
Pulsed Laser Deposition (PLD)

3.1 Background

Laser has been developed into a powerful tool in many applications since it was first demonstrated in 1960. Laser possesses many unique properties such as narrow frequency bandwidth, coherence and high power density and because of this it is especially useful in materials processing [1]. Often the light beam is intense enough to vaporize the hardest and most heat resistant materials. Besides, due to its high precision, reliability and spatial resolution, it is widely used in the industry for machining of thin films, modification of materials, material surface heat treatment, welding and micro patterning. Apart from these, polycomponent materials can be ablated and deposited onto substrates to form stoichiometric thin films. This last mentioned application of laser is the so-called pulsed laser deposition (PLD) [2].

3.2 Historical Development of PLD

The first stimulated emission process was postulated by Albert Einstein in 1916. 44 years later, the first optical master using a rod of ruby as the lasing medium was constructed in 1960 by Theodore H. Maiman at Hughes Research Laboratories. Breech and Cross [3], used ruby laser to vaporize and excite atoms from a solid surface in 1962 and this is the start of using laser to ablate materials. Three years later, Smith and Turner [4] used ruby laser to deposit thin films. This marked the very beginning of the development of the pulsed laser deposition technique.

However, the development and investigations of pulsed laser deposition did not gather the expected momentum because of the immaturity of laser technology at that time. The availability of the types of laser was limited; the stability output was poor and the laser repetition rate was too low for any realistic film growth processes. Thus the development of PLD in thin film fabrication was slow comparing with other techniques which can produce much better thin film quality.

The rapid progress of the laser technology [5,6], however, enhanced the competitiveness of PLD. The lasers having a higher repetition rate than the early ruby lasers made the thin film growth possible. Subsequently, reliable electronic Q-switch lasers became available for generation of very short optical pulses. For this reason PLD can be used to achieve congruent evaporation of the target and to deposit stoichiometric thin films.

Pulsed laser deposition as a film growth technique has attained its reputed fame and has attracted wide spread interest after it has been used successfully to grow high-temperature superconducting films in 1987. During the last decade, pulsed laser deposition has been employed to fabricate quality crystalline thin films. Ceramic, oxide, nitride films, metallic multilayers, and various superlattices grown by PLD have been demonstrated [7-9].

3.3 Mechanisms of PLD

In general, the idea of PLD is simple. A pulsed laser beam is focused onto the surface of a solid target. The strong absorption of the electromagnetic radiation by the solid surface leads to rapid evaporation of the target materials. The evaporated materials consist of highly excited and ionized species. They present themselves as a glowing plasma plume immediately in front of the target surface as shown in Figure 3.1. The spatial extent of the plume depends on various parameters such as the background gas pressure.

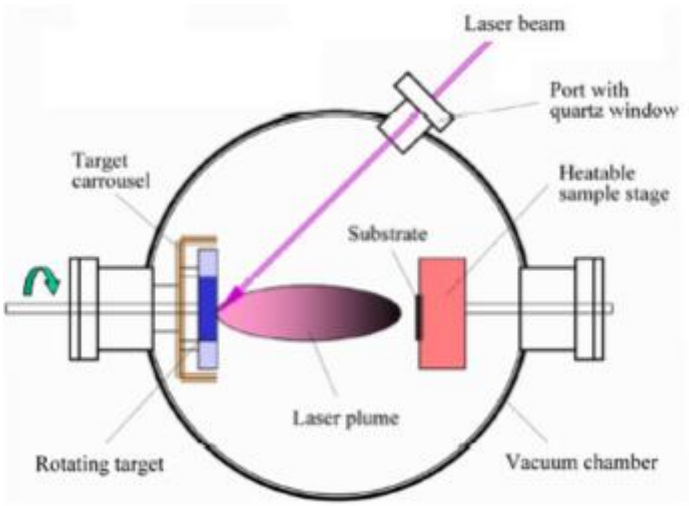

Fig. 3.1: Schematic diagram of typical PLD setup [10].

In PLD, only few parameters need to be controlled during the process of deposition. The targets used are small compared with the large size required for other techniques of making thin films, such as chemical bath deposition (CBD). Using PLD, it is quite easy to produce multi-layered films of different materials (hetrostructures) by sequential ablation of assorted targets. Besides, by controlling the number of pulses, a fine control of film thickness down to atomic monolayer can be achieved.

The most important feature of PLD is that, under careful control of external parameters such as laser energy, substrate temperature, background gas pressure and target to substrate distance, the congruent

transfer of the target can be achieved in the deposited films for most ablated materials [11]. This is the result of the extremely high heating rate of the target surface due to pulsed laser irradiation which leads to the stoichiometric evaporation of the target irrespective of the evaporating point of the constituent elements or compounds of the target. The principle of pulsed laser deposition, in contrast to the simplicity of the system set-up, is a very complex physical phenomenon. It involves all the physical processes of laser-material interaction during the impact of the high-power pulsed radiation on a solid target. It also includes the formation of the plasma plume with high energetic species, the subsequent transfer of the ablated material through the plasma plume onto the heated substrate surface and the final film growth process.

Fig. 3.2: The PLD system used during the thin film growth.

Thus, generally PLD can be divided into the following four stages.

1. Laser-target interaction
2. Dynamic of the ablation materials
3. Decomposition of the ablation materials onto the substrate
4. Nucleation and growth of a thin film on the substrate surface

In the first stage, the laser beam is focused onto the surface of the target. At sufficiently high energy density and short pulse duration, all elements in the target surface are rapidly heated up to their

evaporation temperature. Materials are dissociated from the target and ablated out with stoichiometry as in the target. The instantaneous ablation rate is highly dependent on the fluences of the laser irradiating on the target. The ablation mechanisms involve many complex physical phenomena such as collisional, thermal and electronic excitation, exfoliation and hydrodynamics [12].

During the second stage the emitted materials tend to move towards the substrate according to the laws of gas-dynamic and show the forward peaking phenomenon [13-14]. The laser spot size and the plasma temperature have significant effects on the deposited film uniformity. The target-to-substrate distance is another parameter that governs the angular spread of the ablated materials. Hanabusa [15] also found that a mask placed close to the substrate could reduce the spreading.

The third stage is important to determine the quality of thin film. The ejected high-energy species impinge onto the substrate surface and may induce various type of damage to the substrate. The mechanism of the interaction is illustrated in the following figure. These energetic species sputter some of the surface atoms and a collision region is established between the incident flow and the sputtered atoms [16]. Film grows immediately after this thermalized region (collision region) is formed. The region serves as a source for condensation of particles. When the condensation rate is higher than the rate of particles supplied by the sputtering, thermal equilibrium condition can be reached quickly and film grows on the substrate surface at the expense of the direct flow of the ablation particles.

Nucleation-and-growth of crystalline films depends on many factors such as the density, energy, degree of ionization, and the type of the condensing material, as well as the temperature and the physical-chemical properties of the substrate [17]. The nucleation process depends on the interfacial energies between the three phases present – substrate, the condensing material and the vapour. The critical size of the nucleus depends on the driving force, i.e. the deposition rate and the substrate temperature. For the large nuclei, they create isolated patches (islands) of the film on the substrates, which subsequently grow and coalesce together.

The crystalline film growth depends on the surface mobility of the adatom (vapor atoms). Normally, the adatom will diffuse through several atomic distances before sticking to a stable position within the newly formed film. The surface temperature of the substrate determines the adatom's surface diffusion ability. High temperature usually favors rapid and defect free crystal growth for most materials [18].

In the PLD process, due to the short laser pulsed duration (~10 ns) and the small temporal spread ($< 10\ \mu s$) of the ablated materials, the deposition rate can be enormous (~$10\ \mu m/s$). Consequently a

layer-by-layer nucleation is favored and ultra-thin and smooth film can be produced. In addition the rapid deposition of the energetic ablation species helps to raise the substrate surface temperature.

3.4 Complex plume and formation of the Knudsen layer

The plume composition is complex, especially for multicomponent targets, and may change during expansion. In the first few millimeters of the plume expansion, emission from atoms and ions, multiple charged ions and possible molecules can typically be observed together with electromagnetic radiation produced by the deceleration of charged particles (Bremsstrahlung emission) in the plasma [19]. After the first millimeters of expansion, Bremsstrahlung emission and emission from multiple charged ions are no longer observed.

For plume expansion in vacuum, the density of ablated particles may be initially high and the ablated particles close to the target surface have an anisotropic velocity distribution, all velocity vectors pointing away from the target surface. However, this anisotropic velocity distribution is transformed into an isotropic one by collisions among the ablated particles. This happens within a few mean-free paths from the surface, a region known as the Knudsen layer [20].

3.5 Gas dynamics and film profiles in PLD

Deposition and/or ablation can be of great interest in vast fields of physics, e.g., thin film deposition, material evaporation. A clear understanding of the physics defining the plume expansion is of fundamental importance in such applications of laser ablation as thin films deposition and mass spectrometry. Quality of the deposited films in pulsed laser deposition [21-22] and quality of mass spectra in matrix assisted laser desorption ionization [23-24] are critically dependent on the velocity distributions of the ejected species and their spatial distributions in the plume. Theoretical and computational investigation of the laser ablation phenomenon is challenging due to the complex collective characters of the involved processes that occur at different time and length scales [25-26]. Plume behavior can be described as a two-stage process: a “violent” plume expansion due to the absorption of the laser beam energy (during the laser pulse) followed by a fast adiabatic expansion in the ambient gas (after the end of the laser pulse). Plasma plume may last a few microseconds and may have densities 10 times lower than the solid densities at temperatures close to the ambient temperature [27]. Many theoretical models can be found in the literature concerning the plume expansion; some have been in vacuum and others in gas atmosphere. A clear understanding of the physics defining the plume expansion is of great importance in many laser-matter interactions and laser applications.

The expansion of the laser induced plasma plume increases on its way from the target to the substrate. This varies the particle flux of the target species over the substrate area which makes the different parts of the same film to have slightly different thickness. It is reported that near the axis of the plasma plume, the angular distribution of the flux species is proportional to $\cos^{n}\theta$ where $n \gg 1$ and θ is the radial angle with respect to the normal to the substrate [28]. The cause of this strong forward direction is the strong differences in pressure gradients in axial and radial directions. R. K. Singh and J. Narayan, investigated the problem of the angular distribution of the mass flow in the plasma expansion using the isothermal solution of the following gas dynamical equations with Gaussian pressure and density profiles [29].

$$\frac{\partial \rho}{\partial \mathrm{t}} + \mathrm{div}(\rho \boldsymbol{v}) = 0, \qquad (3.1)$$

$$\frac{\partial \boldsymbol{v}}{\partial \mathrm{t}} + (\boldsymbol{v}.\boldsymbol{\nabla})\boldsymbol{v} + \frac{1}{\rho}\nabla P = 0, \qquad (3.2)$$

$$\frac{\partial S}{\partial \mathrm{t}} + (\boldsymbol{v}.\boldsymbol{\nabla})S = 0, \qquad (3.3)$$

where ρ, P, $\boldsymbol{v}$, and S are the density, pressure, velocity and entropy respectively.

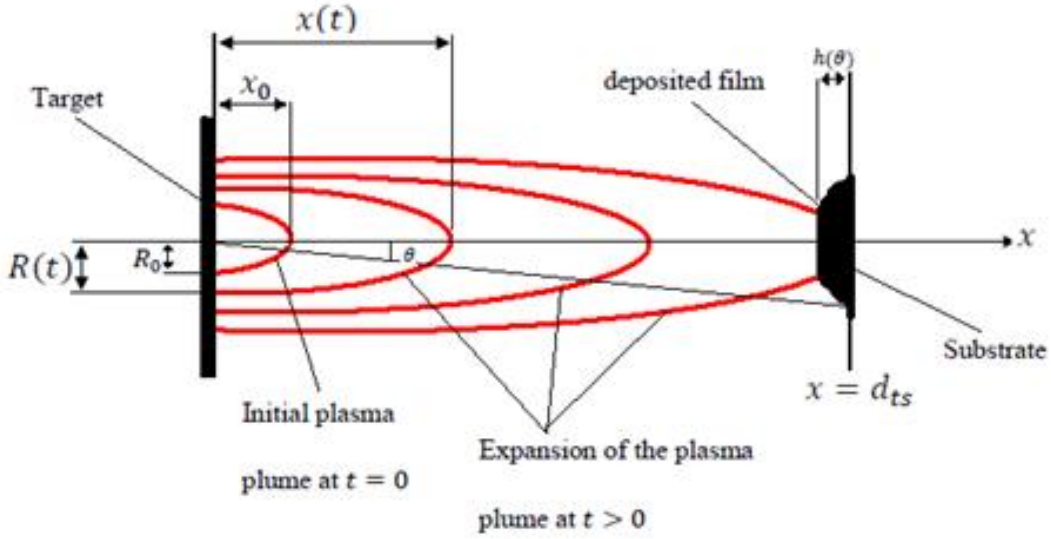

Fig. 3.3: Elliptical plasma plume expansion and the deposited film. R_0 and x_0 are the initial state of the plume at $t = 0$. $R(t)$ and $x(t)$ are the final radius and height of the plume at $t > 0$. The ablated material is deposited and forms a thin film of thickness profile $h(\theta)$ after reaching $x = d_{ts}$.

However, since there exists considerable temperature gradient inside the plasma plume [28, 30], consideration of isothermal solution is inadequate for description of PLD. S. I. Anisimov et al considered an adiabatic expansion of the plume, which is more realistic situation [28] and described the ellipsoidal expansion of the plasma plume in to vacuum by the above gas dynamic equations as well. By assuming that the evaporated material can be described by the equation of the ideal gases with a constant adiabatic exponent $\gamma = c_P/c_v$, they rigorously derived the angular dependence of the film thickness $h(\theta)$ which is given by,

$$h(\theta) = \frac{M\mathrm{k}^2}{2\pi\rho_s {d_{ts}}^2}(1 + \mathrm{k}^2 tan^2\theta)^{-\frac{3}{2}}, \quad (3.4)$$

where M is the mass of the plume, ρ_s is the density of the deposited material, k is a constant and θ is as defined above. This is a powerful technique in determining the thickness profile of a deposited film theoretically. Change in $\mathrm{d_{ts}}$ changes the value of the radial angle θ (from simple trigonometry) and the thickness profile $h(\theta)$. It is clear that the thickness profile depends both on d_{ts} and θ. Figure 3.3 depicts the typical expansion of the plasma plume and deposition of the film. The parameters x_0 and R_0 are the initial height and radius of the plasma plume respectively. Here R_0 can be approximated by the radius of the laser spot. The dependence of $h(\theta)$ which follows from equation (4) is shown in Figure 3.4. It shows that the thickness profile decreases at relatively larger radial angles.

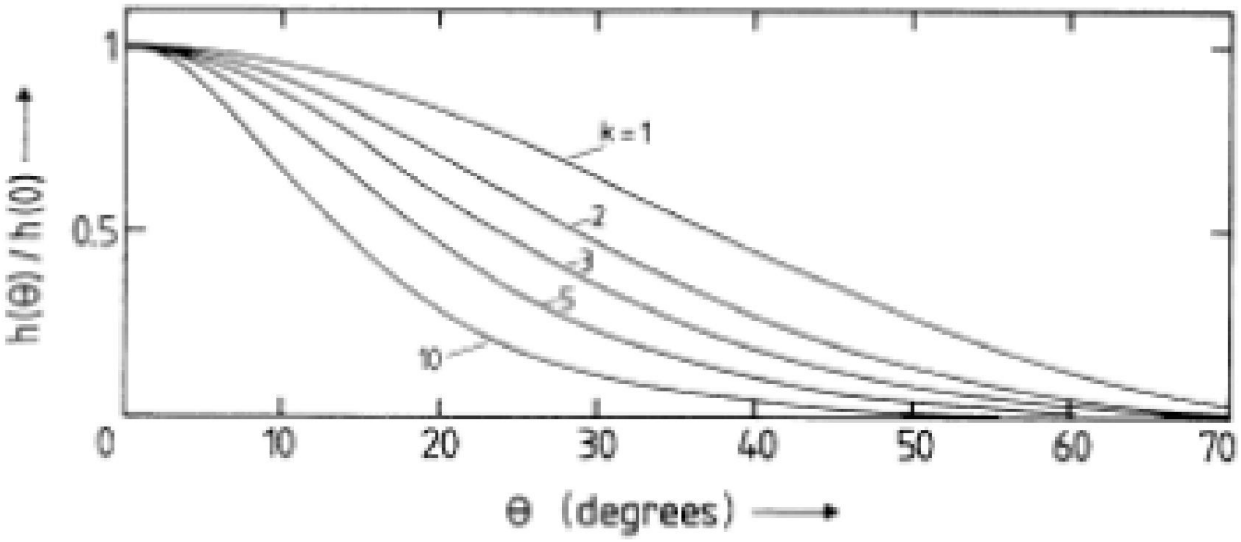

Fig. 3.4: Stationary profile of the deposited film for various values of θ [28].

3.6 Parameters for pulsed laser deposition

3.6.1 Background gas pressure

Ambient gases present during PLD scatter, attenuate, and thermalize the plume, changing important film growth parameters such as the spatial distribution, deposition rate, and kinetic energy distribution of the depositing species. In addition, the plume particles can react chemically with the gas particles. In general, raising the background pressure results in the following effects:

- Slowing of the plume: After a few microseconds of expansion and at sufficiently high background gas pressure, the plume slows down relative to the propagation in vacuum and eventually coalesces with slower moving material [31]. The velocity of the emitted particles is maximum for helium and minimum for argon background gas. This is attributed to larger degree of freedom per unit mass of helium than of any other gas and hence the collisional volume of helium is less as compared to that of other gases. The emitted species cover larger distances in helium atmosphere followed by air, oxygen, and argon [32].
- Sharpening of the plume boundary, indicative of a shock front: As the plume propagates into the background atmosphere it seems to push the background gas ahead and a sharp plume boundary may be created at the plume front. This plume sharpening indicates the formation of a shock front.
- Plume splitting: At intermediate background gas pressures (in the 10^{-3} mbar range) the plume tends to split up into a fast (collisionless) and a slow (scattered) component.
- Changes in angular distribution: In the presence of an ambient gas, the nascent plume angular distribution is perturbed by additional plume particles collisions with the background gas. These collisions scatter the plume particles from their original trajectories and broaden the angular distribution. Collision-induced broadening effects might be expected to begin appearing when the mean free path of a particle in the background gas starts to become less than the target-substrate distance, d_{ts}.
- Plume thermalization: With typical PLD target-substrate distances around a few centimeters and at sufficiently high background gas pressures, i.e. $\geq 10^{-1}$ mbar approximately, the plume particles can thermalize completely.
- Chemical reactions: Reactive scattering can result in the formation of molecules or clusters in the plume [31].

The influence of inert gas pressure on deposition rate during PLD is investigated [33]. It is reported that under ultrahigh vacuum, re-sputtering from the film surface occurs due to the presence of energetic

particles in the plasma plume. With increasing gas pressure, a reduction of the particle energy is accompanied with a decrease of re-sputtering and a rise in the deposition rate. At higher gas pressures, scattering of ablated material out of the deposition path between target and substrate was observed, and this lead to a decrease in the deposition rate. The maximum deposition rate was obtained in a He pressure of about 300mTorr.

3.6.2 Laser Fluence

In PLD, fluence is the parameter that controls the energy of the laser as well as the spot of the laser on the target sample. Particles' number density depends on the fluence. The particle number density increases with increasing fluence and decrease again at higher fluence which shows saturation. There is however a threshold at which below it the particles are barely visible. For example the threshold for yttrium barium copper oxide (YBCO) is about 0.9 J/cm2 when a XeCL 308 nm excimer laser with 20 ns pulses is used [34]. Crystalline quality of the films improves with increasing fluence. The increased energy cause an increase in plasma density and enhancement of mobility of the deposited atoms on substrate surface and this result in better orientation and thus improved crystalinity [35]. The improvement of crystallization with increased laser fluence was also showed by Fang et al. [36].

3.6.3 The type of background gas

PLD in a background gas is a promising method of preparing multicomponent functional thin films, because interactions between the ablated species and the background gases promote not only physical collisions but also chemical reactions, and affect the characteristics of the deposited films [37]. Moreover, the background gas determines the mean free path length, the kinetic energy, the time the particles take inside the plume. The increased collisions decrease the kinetic energies of the particles, slowing them down, increasing their stay time in the plume as they move slower. In general, deposition in various background gases changes the structural, optical and electrical properties of films. For example, the properties of In_2O_3 films deposited in oxygen and helium/oxygen mixture are investigated. It was found that the films depend on the oxygen content. Oxygen deficiency leads to darkening of the films because of suboxide formation. However, transparent films were obtained for the films deposited in He/O_2 gas mixture. Moreover, it was found that the resistivity of the films deposited in He/O_2 gas mixture is less than that of the films deposited in pure He.

3.6.4 Substrate temperature

The substrate temperature also plays a significant role during PLD and influences the kinetic energies of the particles once on the substrate surface which leads to better crystalinity [38-39]. This was reported during investigating the effect of substrate temperature on structural, optical and electrical properties of ZnO thin films deposited by PLD and the investigation of optical properties of sol-gel derived Y2O3:Eu3+ thin film phosphors for display applications respectively. The substrate temperature not only affects the crystallinity but it can also influence the thin film composition. XRD results obtained showed a constraint in the growth of the crystal due to low atomic mobility at a deposited temperature of 100 °C [38]. An increase to 500 °C supplied the atoms on the substrate surface with more thermal energy and thus increased their surface mobility that lead to better crystallization. However at too high temperatures such as 700 °C, decrease in the crystallinity of the thin films was observed and it was due to desorption and dissociation of atoms.

3.6.5 Target to substrate distance

The target to substrate distance (d_{ts}) is one of the most critical factors which affect the quality and properties of films in PLD. For instance, it was observed that the crystallinity and thickness of rhodium (Rh) thin films reduced with the increase of d_{ts} [40]. It is due to the increase of hemispherical expansion of the laser induced plasma plume with the increase of d_{ts}. As mentioned before, the particle flux of the ablated species in the plume over the substrate area decreases with the increase of d_{ts} which lowers the deposition rate of the Rh films and hence the thickness. The possible mechanism for the reduction in surface roughness is due to plume expansion. The substrate area at large distance is exposed to more uniform plasma plume. Moreover, the particle flux density also reduces due to the plume expansion. These low density laser ablated particles slowly showered onto the substrate. Further, the re-sputtering of deposited material from the film surface on shot to shot basis of the laser beam is reduced at large d_{ts} due to the decrease in kinetic energy of the Rh atom.

On the other hand, literature shows that the crystallinity of aluminum doped ZnO films is improved and the crystallite size becomes larger when the d_{ts} is increasing, while there is no change in the thickness of the films [41]. Moreover, it was found that with decreasing the d_{ts}, the growth rate is increased and the films become more stiochiometric. Therefore, it can be concluded that the properties of thin films deposited under various values of d_{ts} also depend on the type material deposited.

Table 3.1: Summary of typical parameters for PLD.

Parameter	Typical values
Materials examples	KY3F10, Y2SiO5, etc
Laser wavelength	248, 266, 308, 355 nm, etc
Laser pulse width	6-50 ns
Laser repetition rate	1-10 Hz
Laser fluence	0.5-5 J/cm^2
Vacuum pressure	10^{-7} mbar
Background gas	O_2, Ar, NO_2, etc
Background gas pressure	1-300 Torr
Substrate	MgO, Si, Al_2O_3, glass, etc
Substrate temperature	25-800^{o}C

3.7 Advantages and disadvantages of PLD

3.7.1 Advantages of PLD

PLD is so straightforward that only a few parameters, such as laser energy density and pulse repetition rate, need to be controlled during the process. The targets used in PLD are small compared with the large size required for other sputtering techniques. It is quite easy to produce multi-layered films of different materials by sequential ablation of assorted targets. Besides, by controlling the number of pulses, a fine control of film thickness down to atomic monolayer can be achieved. The most important feature of PLD is that the stoichiometry of the target can be retained in the deposited films. This is the result of the extremely high heating rate of the target surface (10^8 K/s) due to pulsed laser irradiation. It leads to the congruent evaporation of the target irrespective of the evaporating point of the constituent elements or compounds of the target. And because of the high heating rate of ablated materials, laser deposition of crystalline film demands a much lower substrate temperature than other film growth techniques. For this reason the semiconductor and the underlying integrated circuit can refrain from thermal degradation. Moreover, PLD is also a good technique for depositing extremely pure films.

3.7.2 Disadvantages of PLD

In spite of the said advantages of PLD, some shortcomings have been identified in using this deposition technique. One of the major problems is the splashing or the particulates deposition on the films. The

physical mechanisms leading to splashing include the sub-surface boiling, expulsion of the liquid layer by shock wave recoil pressure and exfoliation. The size of particulates may be as large as a few micrometers. Such particulates will greatly affect the growth of the subsequent layers as well as the electrical properties of the films. Another problem of PLD is the narrow angular distribution of the ablated species, which is generated by the adiabatic expansion of laser, produced plasma plume and the pitting on the target surface. These features limit the usefulness of PLD in producing large area uniform thin films, and PLD has not been fully deployed in industry. Recently remedial measures have been proposed. Inserting a shadow mask is effective to block off the large particulates. Rotating both the target and substrate can help to produce larger uniform films.

The other major problem in PLD is the presence of particulates on the film surface. Particulates can originate from liquid droplets that are expelled from the target during irradiation, from ejected protruding surface features that are mechanically removed from the target by laser induced thermal and mechanical shock, or from cluster condensation from vapour species due to supersaturation. The first particulate type is typically observed at laser power densities above $10^7\ \mathrm{W/cm^2}$, and the latter type is most likely observed in the presence of a background gas during film deposition. Typical particulate sizes are in the micron and submicron ranges, however, for particulates formed from the vapour state the size tends to be in the nanometer range. In general, the density and the size of particulates on the deposited film surface tend to increase with increasing laser fluence.

References

[1] S.M. Metev and V.P. Veiko, Laser Assisted Microtechnology, Springer, Berlin, 1994.

[2] D.B. Chrisey and G.K. Hubler, Pulsed Laser Deposition of Thin Film, John Wiley & Sons, New York, 1994.

[3] F. Breech and L. Cross, Appl. Spect.16, 59 (1962).

[4] H.M. Smith and A.F. Tuner, Appl. Opt. 4, 147 (1965).

[5] C.K.N. Patel, Phys. Rev. Lett.12, 588 (1964).

[6] J.E. Geusic, H.M. Marcos and L.G. Uitert, Appl. Phys. Lett. 4, 182 (1964).

[7] Q. Shi, Thin Solid Films 520, 6845 (2012).

[8] S. Isber, EPJ Web of Conferences, 75, 03008 (2014).

[9] S. Aoqui, Thin Solid Films 407, 126 (2002).

[10] http://titan.physx.u-szeged.hu/~lamilab/plden.htm [accessed on October 31, 2016].

[11] P.D. Nsimama, O.M. Ntwaeaborwa, H.C. Swart, Journal of Luminescence 131, 119 (2011).

[12] G. L. Hornyak, Introduction to Nanoscience and Nanotechnology, CRC Press, (2008).

[13] A. Namiki, T. Kawai, K. Ichige, Surf. Sci. 166, 129 (1986).

[14] A.V. Singh, J. Appl. Phys. 90, 5661 (2001).

[15] M. Hanabusa, Mater. Res. Soc. Symp. Proc. 285, 447 (1993).

[16] D. Manova, J. W. Gerlach and S. Mändl, Materials, 3,4109 (2010).

[17] M. A. Silva Leal, Pulsed Laser Deposition and Characterization of $Na_{0.5}K_{0.5}NbO_3$ Thin Films, PhD dissertation, Universidade Tecnica de Lisboa, 2012.

[18] F. Engang, Study of epitaxial thin films of $yba_2cu_3o_{7-\delta}$ on silicon with different buffer layers, PhD Thesis, The University of Hong Kong, 2005.

[19] R. Issac, Evolution and Dynamics of Plasma Generated from Solid Targets by Strong Laser Fields, PhD Thesis, Cochin University of Science & Technology, 1998.

[20] R. Kelly and R. W. Dreyfus, Surface Science 198, 263 (1988).

[21] L. Saenger, Proc. Adv. Mat. 2, 1 (1993).

[22] A.V. Singh, R.M. Mehra, N. Buthrath, A. Wakahara, J. Yoshida, J. Appl. Phys. 90, 5661 (2001).

[23] A. Rohrbacher, R.E. Continetti, Rev. Sci. Instrum. 72, 3386 (2001).

[24] F. Hillenkamp, M. Karas, Int. J. Mass. Spectrom. 200, 71 (2000).

[25] L.V. Zhigilei, A.M. Dongare, CMES 3,539 (2002).

[26] N.M. Bulgakova, *JLMN* 2, 76 (2007).

[27] M. Cirisan, J.M. Jouvard, L. Lavisse, L. Hallo, R. Oltra, J. Appl. Phys. 109, 103301 (2011).

[28] S. I. Anisimov, D. Bauerle, B. S. Luk'yanchuk, Phys. Rev. B 48, 12076 (1993).

[29] R. K. Singh and J. Narayan, Phys. Rev. B 41, 8843 (1990).

[30] M. K. Matzen and R. L. Morse, Phys. Fluids 22, 654 (1979).

[31] R. Delmdahl, A. Wiessner Journal of Physics: Conference Series 59, 28 (2007).

[32] A. Misra and R.K. Thareja, IEEE Transactions on Plasma Science, 27, 1553 (1999).

[33] T. Scharf and H. U. Krebs, Appl. Phys. A, 75, 551 (2002).

[34] L. Chen, Particles generated by pulsed laser ablation, John Wiley & Sons, Inc, New York, 1994.

[35] X. L. Tong, D. S. Jiang, L. Liu, Z. M. Liu, M. Z. Luo, Optics Communications, 270, 356 (2007).

[36] L. Fang and M. Shen, J. Crystal Growth, 310, 3470 (2008).

[37] Y. Yamanda, Proc. SPIE 4637, Photon processing in Microelectronics and Photonics, 119 (2002).

[38] S. J. Kang, Y. H. Joung, H. H. Shin and Y. S. Yoon, J. Mater. Sci: Mater. Electron, 19, 1073 (2003).

[39] J. Y. Cho, K. Ko and Y. R. Do, Thin Solid Films, 515, 3373 (2007).

[40] A. T. T. Mostako, Alika Khare, Appl Nanosci,2, 289 (2012).

[41] S.H. Jeong, J.H. Boo, Thin Solid Films 447, 105 (2004).

Chapter 4
Review of Experimental Techniques

In this research work, the phosphor powders and thin films were characterized using Atomic Force Microscopy (AFM), Photoluminescence Spectroscopy (PL), Scanning Electron Microscopy (SEM), Thermoluminescence Spectroscopy (TL), Transmission Electron Microscopy (TEM), UV-VIS Spectroscopy and X-ray Diffraction (XRD). The brief theoretical review of these characterization techniques are covered in this chapter.

4.1. Atomic Force Microscope (AFM)

Atomic Force Microscope (AFM) is a form of scanning probe microscope where a small probe scans across the sample surface to obtain information about the sample's local properties such as height, friction and magnetism [1]. To acquire an image, the SPM raster-scans the probe over a small area of the sample measuring the local properties simultaneously.

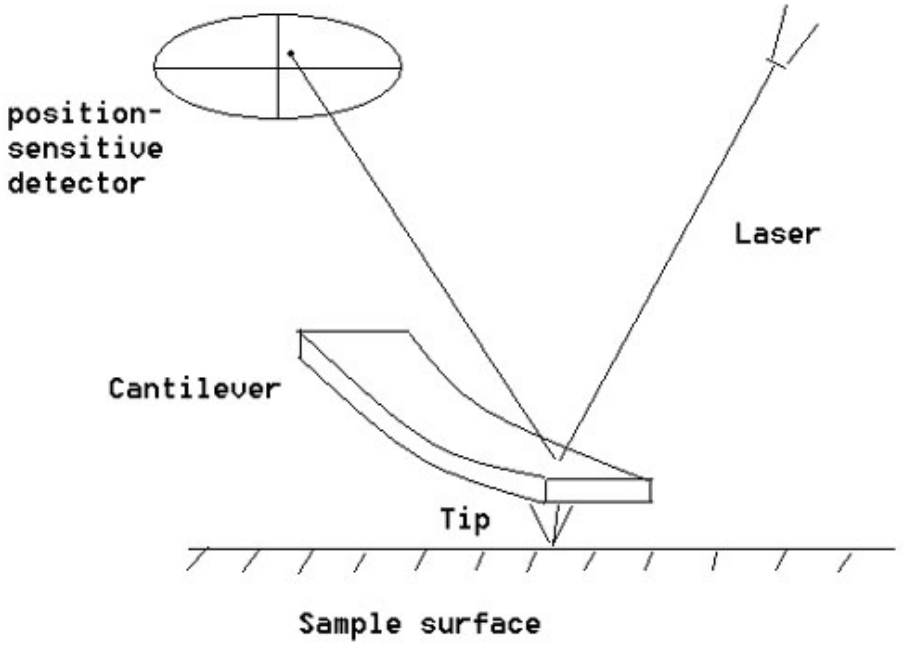

Fig. 4.1: Principles of AFM [2].

The AFM has been applied to problems in a wide range of disciplines of natural sciences including solid state sciences, semiconductor science and technology, molecular engineering, polymer chemistry and physics, molecular biology, cell biology and medicine. AFM consists of a cantilever with a sharp tip (probe) at its end that is used to scan the sample surface (see Figure 4.1). The cantilever is typically silicon or silicon nitride with a tip radius of curvature of the order of nanometers. The probe is attached to a piezoelectric scanner tube, which scans the tube across a selected area of the sample surface. When the tip is brought in to proximity of a sample surface, forces between the tip and the sample lead to a deflection of the cantilever [3]. Depending on the situation, forces that are measured in AFM include mechanical contact force, van der waals forces, capillary forces, electrostatic forces, magnetic forces, etc. These forces between the probe tip and the sample surface, which are determined by the deflection of the cantilever during scanning, causes the cantilever to deflect as the sample's surface topography changes.

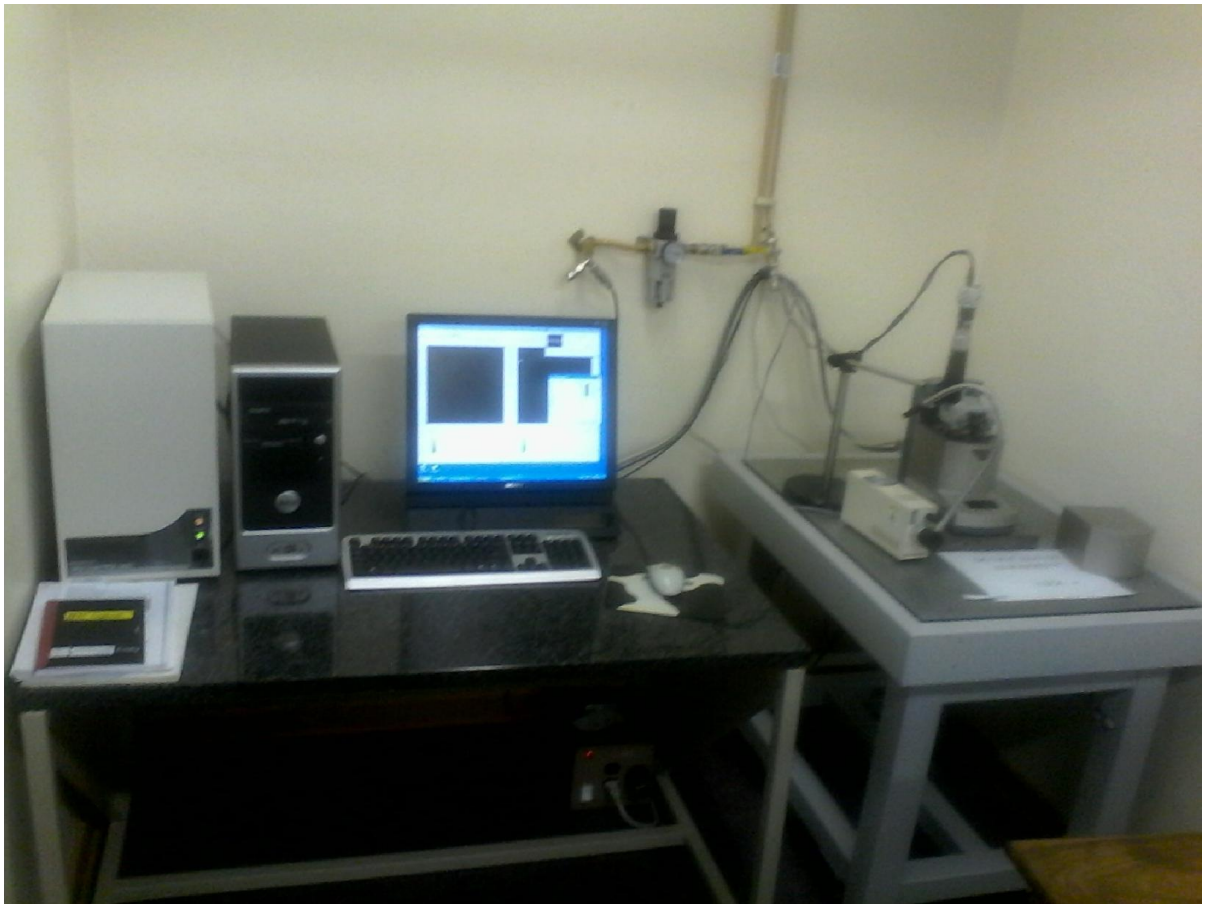

Fig. 4.2: Shimadzu SPM-9600 model AFM used during the experiment.

The deflection of the cantilever is measured by optical lever technique. A beam from a laser diode is focused onto the end of the cantilever and the position of the reflected beam is monitored by a position sensitive detector [3]. The deflection of the cantilever is measured by the laser beam reflected from the back of the cantilever. By plotting the deflection of the cantilever versus its position on the sample, a topographic image of the sample can be obtained and this information is fed back to a computer, which generates a map of topography or other properties of interest. With AFM, which normally operates in contact mode, tapping mode or non-contact mode [4], areas as large as about 100 μm square to less than 100 nm square can be imaged [5].

In this work, the AFM images were recorded using Shimadzu SPM-9600 model shown in Figure 4.2 and Bruker Dimension Icon.

4.2. Cathodoluminescence spectroscopy (CL)

Cathodoluminescence is generated when a suitable specimen, such as a polished thin section, is bombarded with a beam of high-energy electrons [6]. A major breakthrough in cathodoluminescence instrumentation came with the development of CL detectors that could be attached to a scanning electron microscope (SEM). Because of its high magnification capability and the capability of combining CL and SEM observations (e.g., backscatter and secondary imaging), SEM–CL is rapidly becoming the technique of choice for high-resolution CL imaging [7]. When a specimen on the stage of the microscope is bombarded or irradiated by the electron beam, various kinds of emissions take place including emission of secondary electrons, backscattered electrons, X-rays, and photons. Detectors must be present to capture or collect these emissions and convert the signals, by appropriate electronics, to point-by-point intensity changes on the viewing screen and produce an image. The signals are collected by the detector and passed by means of a light pipe (e.g., a fiber-optic cable) to a photomultiplier tube (PMT), which is a device for measuring photon counts. When light enters the photocathode, the photocathode emits photoelectrons into the vacuum. These photoelectrons are then directed by the focusing electrode voltages towards the electron multiplier where electrons are multiplied by the process of secondary emission [8]. The multiplied electrons are collected by the anode as an output signal. The signal from the PMT is amplified for display and viewing on a CRT. A detector is also present to collect X-ray signals, and a CL detector can be added to collect photon (cathodoluminescence) emissions. In this research work, the CL spectra are obtained by using a CL detector attached to JSM-7800F field emission SEM.

4.3. Energy Dispersive x-ray spectroscopy (EDS)

The elemental composition/mapping of the thin films investigated in this research study was determined by EDS spectroscopy equipped in SEM. EDS makes use of the x-ray spectrum emitted by a solid sample bombarded with a focused beam of electrons to obtain a localized chemical analysis. All elements from atomic number 4 (Be) to 92 (U) can be detected in principle, though not all instruments are equipped for 'light' elements (Z < 10) [9]. Part of the sample as small as 1 μm can be analyzed [10]. Qualitative analysis involves the identification of the lines in the spectrum and is fairly straightforward owing to the simplicity of x-ray spectra. Quantitative analysis (determination of the concentrations of the elements present) entails measuring line intensities for each element in the sample.

The incident beam of electrons generated by the electron gun of the SEM interact with core electrons of the sample's atoms transferring sufficient energy to it, thereby ejecting it from the target atom resulting in the creation of holes in the atom's electronic structure. An electron from the outer high energy shell then occupies the hole releasing excess energy in the form of an x-ray photon. This emitted x-ray photon is characteristic because its energy equals the energy difference between the two levels involved in the transition and this difference is characteristic of the material. The quantitative and qualitative elemental composition of the sample can be determined from the emitted x-ray photon [11]. Due to a well-defined nature of the various atomic energy levels, it is clear that the energies and associated wavelengths of the set of x-rays will have characteristic values for each of the atomic species present in the sample [11]. By scanning the beam in a television-like raster and displaying the intensity of a selected X-ray line, element distribution images or 'maps' can be produced.

4.4. Photoluminescence Spectroscopy (PL)

In the process of photo-excitation, light is directed onto the sample and gets absorbed to impart excess energy into the material causing creation of electron-hole pairs. As the system relaxes to its ground state, the excess energy is released through the emission of light and this process is called photoluminescence [12].

Photoluminescence Spectroscopy is a contactless, non-destructive method of probing the electronic structure of materials and it was done on the phosphor materials studied in this research. In PL, one measures the emission properties of materials by using photons to induce excited electronic states in the material system and analyzing the optical emission as these states relax. In the PL experiment, the sample is excited by a light of certain wavelength for creation of electron-hole pairs in the sample. The

system is connected to a computer for displaying the PL excitation and emission spectra. Therefore, two kinds of spectra (the excitation and emission spectra) can be registered. In excitation spectra, the emission monochromator is fixed at any emission wavelength while the excitation wavelength is scanned in a certain spectral range. In emission spectra, the excitation wavelength is fixed and the emitted light intensity is measured at different wavelengths by scanning the emission monochromator. In PL spectroscopy, even very small quantities or low concentrations of materials can be analyzed because of the high sensitivity of the technique. Precise quantitative concentration determinations are difficult unless conditions can be carefully controlled, and many applications of PL are primarily qualitative.

Fig. 4.3: Cary Eclipse fluorescence spectrophotometer.

In this study, the excitation and emission spectra were measured at room temperature using a Cary Eclipse fluorescence spectrophotometer model: LS-55 with a built-in 150W xenon flash lamp and is shown Figure 4.3.

4.5. Scanning Electron Microscopy (SEM)

Scanning Electron Microscopy (SEM) is used to study the topographical and morphological structure of specimens at very high magnifications. In other words, SEM is an instrument capable of producing high-resolution images electronically rather than optically. A beam of electrons produce by the electron gun, focused by a system of electromagnetic lenses is used to produce enlarged images of small objects, which can be displayed on a fluorescent screen [13]. A very fine ‘‘probe’’ of electrons with energies ranging from a few hundred electron volts (eV) to tens of keV is focused at the surface of a specimen. A scanning raster deflects the electron beam so that it scans the surface of the specimen in a pattern of parallel lines. The scan is synchronized with that of the cathode-ray tube, allowing a picture to be built up of the scanned area of the sample.

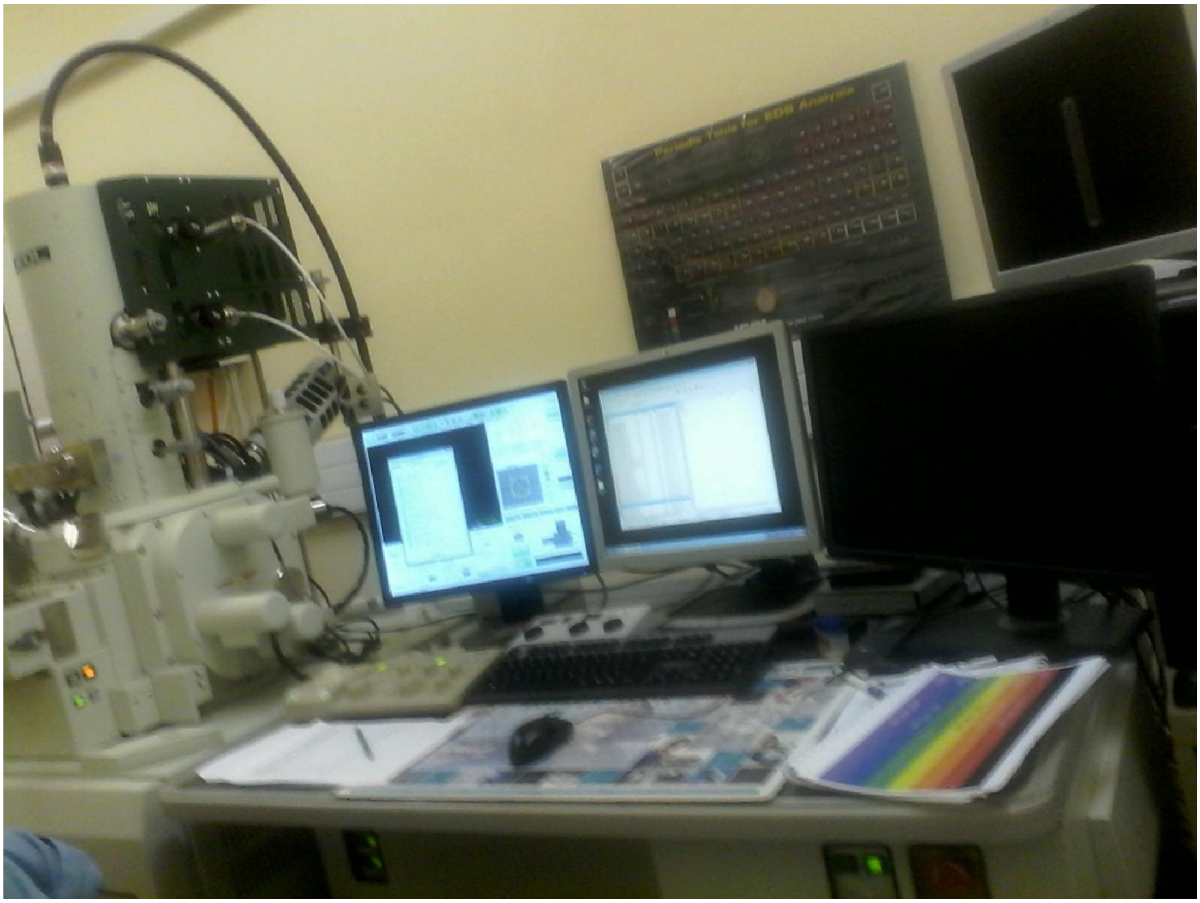

Fig. 4.4: SEM used during the experiment.

The electron gun consists of tungsten or lanthanum hexaboride (LaB_6) filament source, or a field emission electron gun which is used to generate electrons, when the applied current causes resistance

heating which generates the electrons [14]. The highest possible vacuum is maintained using turbo and ion pumps [15]. Using SEM, information like external morphology (texture), chemical composition and crystalline structure and orientation of materials making up the sample can be obtained [?].

In this research work, a highly advanced JSM-7800F Field Emission SEM (FESEM) equipped with EDS and CL was used (see Figure 4.4). It has superb resolution and stability for imaging and analysis which makes it possible to observe the finest structural morphology of nanomaterials at 1000,000X magnification with sub-1nm resolution [16].

4.6. Thermoluminescence (TL) Spectroscopy

Heating a phosphor which is previously excited with some external source of excitation increases the afterglow called thermally stimulated luminescence (TSL) because of the recombination of electrons de-trapped from deep traps within the phosphor. As discussed in chapter 2, this type of luminescence is called thermoluminescence (TL), and the temperature dependence of the TL intensity is called the glow curve. In order to measure the glow curve of a given sample, one needs to cool the sample down to room temperature and excite it by some source of external radiation such as UV light. Then the excitation should be terminated and the temperature of the sample is raised at a constant rate while the intensity is recorded.

The TSL glow curves in this research work were obtained by TL reader type TL1009I (Figure 4.5) offered by Nucleonix systems Pvt. Ltd., India interfaced to a PC where the TL signals were analyzed.

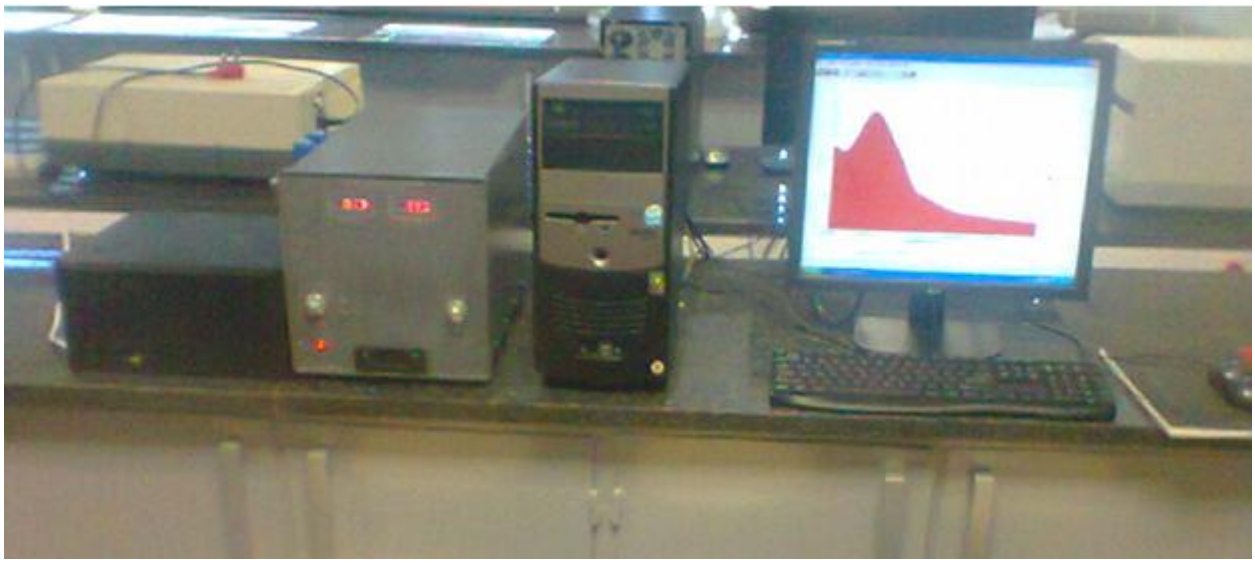

Fig. 4.5: Thermoluminescence reader type TL1009I.

The user can easily subject the TL sample under study to the desired heating profile and record the digitized glow curve because of its versatile controller based unit. A complete electronics hardware circuits (comprising of Power Electronics, Low/High voltage Supplies, Temperature Controller, Micro Controller based data acquisition circuits, sample heating system, drawer assembly, etc.) are enclosed in a single enclosure [17]. Some of the software features like glow curve acquisition, analysis, filing, printing, plotting, overlapping, maker data reporting, etc are also included in the system. This Integral TL Reader unit gets connected to the personal computer system through USB port. This system essentially works as a PC controlled TL reader with command buttons and dropdown menus defined for various functions. This system has been evaluated for its performance with $CaSO_4$: Dy discs, powder, as well as with LiF: Mg, Ti chips [17]. Linearity and reproducibility have been found to be quite satisfactory also within +2%. This system is quite useful to study the TL of phosphor, minerals and characterization of various solid semiconducting materials, and also can be used in personal dosimetry measurements and research studies in medical dosimetry, environmental radiation monitoring, etc.

4.7. Transmission Electron Microscopy (TEM)

Transmission Electron Microscopy (TEM) is an imaging technique in which a beam of electrons generated by an electron gun is transmitted through a thin specimen and then an image is formed through the interaction of electrons with the specimen. It is a valuable analysis technique applied in a wide range of scientific fields such as medicine, biological/physical sciences, material sciences etc. TEM can investigate the size, morphology (shape), and arrangement of the particles which make up the sample on the scale of atomic diameters [15]. The TEM is capable of displaying magnified images of a thin specimen, typically with a magnification in the range 10^3 to 10^6. In addition, the instrument can be used to produce electron-diffraction patterns, useful for analyzing the properties of a crystalline specimen. This overall flexibility is achieved with an electron-optical system containing an electron gun and several magnetic lenses, stacked vertically to form a lens column. The instrument consists of the illumination system, the specimen stage, and the imaging system.

The illumination system comprises the electron gun, together with two or more condenser lenses that focus the electrons onto the specimen. Its design and operation determine the diameter of the electron beam (often called the “illumination”) at the specimen and the intensity level in the final TEM image. The specimen stage allows specimens to either be held stationary or else intentionally moved, and also

inserted or withdrawn from the TEM. The mechanical stability of the specimen stage is an important factor that determines the spatial resolution of the TEM image.

The imaging system contains at least three lenses that together produce a magnified image (or a diffraction pattern) of the specimen on a fluorescent screen, on photographic film, or on the monitor screen of an electronic camera system. How this imaging system is operated determines the magnification of the TEM image, while the design of the imaging lenses largely determines the spatial resolution that can be obtained from the microscope. Today's TEM offer resolutions up to 0.1 nm and probe diameters up to 0.34 nm. Due to the fact that that electrons are strongly scattered within a solid as a result of the large forces acting on an electron when it passes through the electrostatic field within each atom, the thickness of a TEM specimen must be very small: usually in the range 10 nm to 1 μm. TEM specimen preparation involves ensuring that the thickness of at least some regions of the specimen are within this thickness range.

4.8. Ultraviolet-Visible (UV-VIS) Spectroscopy

When a beam of radiation strikes any object it can be absorbed, transmitted, scattered, reflected or it can excite fluorescence. Ultraviolet-visible (UV-VIS) spectrometer has become the most important analytical instrument in the modern day laboratory. It is highly preferable in terms of its simplicity, versatility speed, and accuracy. It measures the percentage absorbance (%A), percentage reflectance (%A), and percentage transmittance (%T) in the ultraviolet-visible spectral region. An absorbance versus wavelength graph measures transitions from the ground state to excited state (excitation). Clearly, it is the reverse of photoluminescence where the transition is from the excited state to the ground state. An excitation spectrum looks very much like an absorption spectrum. The greater the absorbance is at the excitation wavelength, the more molecules are promoted to the excited state and the more emission will be observed. By running an UV-VIS absorption spectrum, the wavelength at which the molecule absorbs energy most and is excited to a large extent can be obtained.

The simple single beam spectrophotometer used to measure the absorption spectra consists of the following elements [18].

i. Light source (usually a deuterium lamp for the UV spectral range and a tungsten lamp for the VIS and IR spectral ranges)
ii. A monochromator, which is used to select a single frequency (wavelength) from all of those provided by the lamp source and to scan over a desired frequency range,

iii. A sample holder

iv. A light detector (usually a photomultiplier for the UV-VIS range and a SPb cell for the IR range) to measure the intensity of each monochromatic beam after traversing the sample;

v. A computer to display and record the absorption spectrum.

Fig. 4.6: UV-VIS Spectrophotometer.

A similar and complimentary information to the absorption measurements can be obtained from difffuse reflectance spectra. The diffuse reflectivity is generally used for unpolished or powdered samples. The percedntage reflectance is defined by,

$$\%\mathrm{R} = \frac{\mathrm{I_R}}{\mathrm{I_o}} \times 100 \qquad (4.1)$$

where I_R is the reflected intensity and I_o is the incident intensity. Simlarly, if the intensity of the transmitted light is I_T, the percentage transmittance is given by,

$$\%\mathrm{T} = \frac{\mathrm{I_T}}{\mathrm{I_o}} \times 100 \qquad (4.2)$$

In this work, a Perkin Elmer Scan-Lambda 950 UV-Vis spectrophotometer (LAMBDA^{TM} 950) was used to record the reflectance characteristics of samples and is shown in Figure 4.6.

4.9. X-ray diffraction (XRD)

X-ray diffraction (XRD) is also one of the most important analytical instrument in the modern day laboratory and is an efficient non-destructive technique which is used for many purposes such as investigation of structural properties of crystalline materials, phase identification, determination of grain size, evaluation of lattice constants, and determination of degree of crystallinity in a mixture of amorphous and crystalline substances [19]. The three basic elements of x-ray diffractometer are, an x-ray tube (source), a sample holder and an x-ray detector (see Figure 4.7).

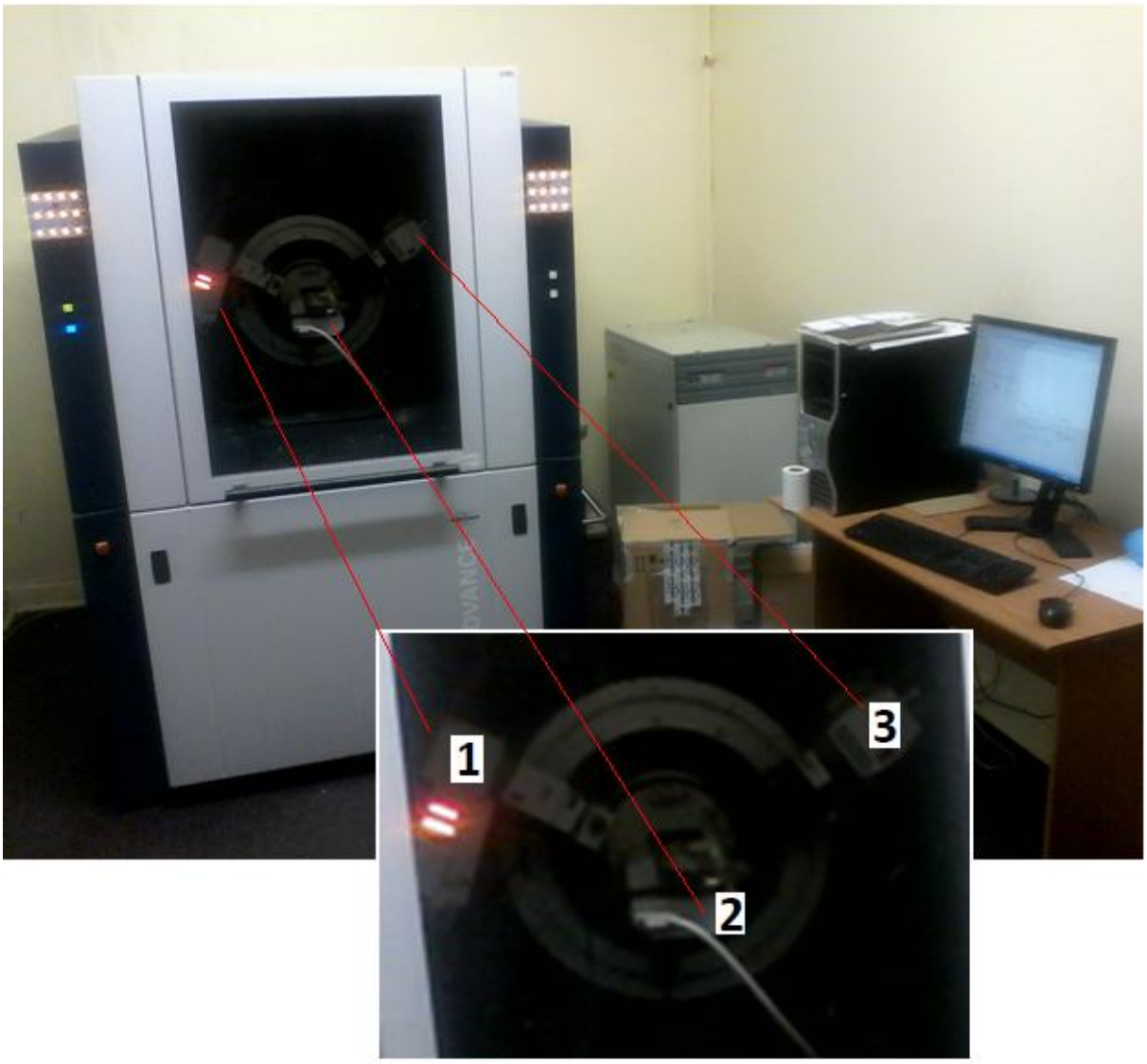

Fig. 4.7: The XRD system. The zoomed part shows the X-ray source (1), the sample holder (2) and the detector (3).

4.9.1. Production of X-ray spectra

X-rays are produced in the x-ray tube as a result of rapid deceleration of electrons. The tube consists of an evacuated chamber with a tungsten filament at one end of the tube, called the cathode, and a metal target at the other end, called an anode. The large voltage difference maintained across these electrons (usually tens of thousands of volts) rapidly derives the electrons to the anode (the target), which they strike with very high velocity. Thus, x-rays are produced at the point of impact and radiate in all directions. Since every electron is not decelerating in the same way, analysis of rays coming out of the target shows the existence of a mixture of different wavelengths, and the variation of intensity with wavelength is found to depend on the tube voltage. The kind of spectra obtained in this way is known as continuous x-ray spectra. The second type of spectra, called the characteristic spectra, is produced when the voltage on an x-ray tube is raised above a certain critical value, characteristic of the target metal. The characteristic lines consist of a sharp intensity maxima appearing at certain wavelengths, superimposed on the continuous spectrum and their wavelengths are characteristic of the target materials used (see Table 4.1).

Table 4.1: Characteristic wavelengths of target materials [18].

Elements	Kα wavelength (λ) in $A°$
Mo	0.7107
Cu	1.5418
Co	1.7902
Cr	2.2909

In other words, when the energy of the electrons accelerated toward the target becomes high enough to dislodge k-shell electrons, electrons from the L and M shells move in to take the place of those dislodged. Each of these electronic transitions produces X-ray with a wavelength that depends on the exact structure of the atom being bombarded. A transition from the L shell to the K shell produces a Kα X-ray, while the transition from M shell to K shell produces Kβ X-rays (see Figure 4.8). These characteristic X-rays have a much higher intensity than those produced by the continuous spectra, with Kα x-rays having higher intensity than Kβ X-rays. The important point here is that the wavelengths of these characteristic X-rays is different for each atom in the periodic table (of course only those elements with higher atomic number have L and M shell electrons that can undergo transitions to produce X-rays). A filter is generally used to filter out the lower intensity Kβ x-rays. From commonly used target materials in x-ray tubes, the x-rays have the well-known experimentally determined wavelengths shown in the Table 4.1.

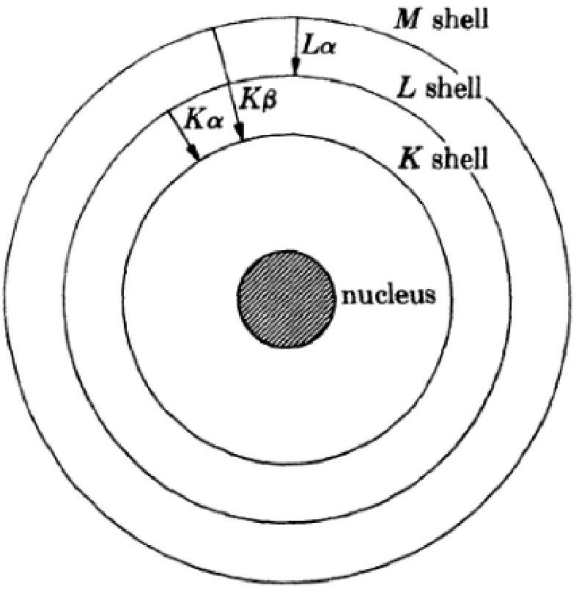

Fig. 4.8: Characteristic X-ray radiations [20].

4.9.2: Bragg's law

A regular three dimensional distribution of atoms in space are arranged in such a way that they form a series of parallel planes separated from one another by a distance d, called interplanar spacing (d-spacing).

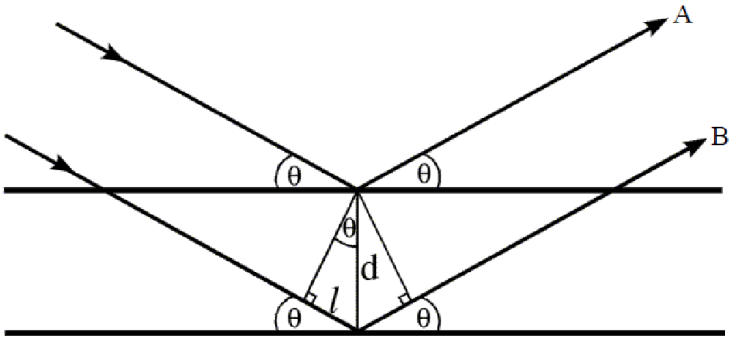

Fig. 4.9: Two incident X-rays entering a crystal with interplanar spacing d.

Because the fact that crystal structure consists of an orderly arrangement of atoms, x-ray reflections occur from the atomic planes. Consider a beam of monochromatic x-rays entering a crystal with one of its planes oriented at an angle of θ to the incoming beam (see Figure 4.9). At the time of exit of ray B from the crystal, it travels a distance of $2l$ further than ray A. Rays A and B will be in phase on their exit from the crystal and constructive interference will occur provided that the path difference between the

two rays ($2l$) is equal to an integral number of wavelengths (nλ). If the distance $2l$ is not an integral multiple of wavelengths, then destructive interference will occur. These, the condition for the constructive interference to occur is

$$n\lambda = 2l \qquad (4.3)$$

Or,

$$n\lambda = 2d\ sin\theta \qquad (4.4)$$

This is known as Bragg's law for X-ray diffraction. Thus, if we know the wavelength λ of the X-rays going in to the crystal and we can measure the angle θ of the diffracted X-rays coming out of the crystal, the d-spacing between the atomic planes is given by;

$$d = \frac{n\lambda}{2\ sin\theta} \qquad (4.5)$$

4.10. X-ray Photoelectron Spectroscopy (XPS)

X-ray Photoelectron Spectroscopy (XPS) is a technique is used to investigate the chemistry at the surface of a sample including information about the chemical states of surfaces of materials such evaluation of valence states, bonding environments and the molecular and atomic composition of surface layers. XPS can also be used for elemental analysis, imaging, and depth profile of thin films [21]. The basic mechanism behind an XPS instrument is illustrated in Figure 4.10.

Photons of a specific energy are used to excite the electronic states of atoms below the surface of the sample. Electrons ejected from the surface are energy filtered via a hemispherical analyzer (HSA) before the intensity for a defined energy is recorded by a detector. Since core level electrons in solid-state atoms are quantized, the resulting energy spectra exhibit resonance peaks characteristic of the electronic structure for atoms at the sample surface. While the x-rays may penetrate deep into the sample, the escape depth of the ejected electrons is limited. That is, for energies around 1400 eV, ejected electrons from depths greater than 10nm have a low probability of leaving the surface without undergoing an energy loss event, and therefore contribute to the background signal rather than well-defined primary photoelectric peaks.

In principle, the energies of the photoelectric lines are well defined in terms of the binding energy of the electronic states of atoms. Further, the chemical environment of the atoms at the surface result in well-defined energy shifts to the peak energies. In the case of conducting samples, for which the detected electron energies can be referenced to the Fermi energy of the spectrometer, an absolute energy scale can be established, thus aiding the identification of species. However, for non-conducting samples the

problem of energy calibration is significant. Electrons leaving the sample surface cause a potential difference to exist between the sample and the spectrometer resulting in a retarding field acting on the electrons escaping the surface. Without redress, the consequence can be peaks shifted in energy by as much as 150 eV. Charge compensation designed to replace the electrons emitted from the sample is used to reduce the influence of sample charging on insulating materials, but nevertheless identification of chemical state based on peak positions requires careful analysis.

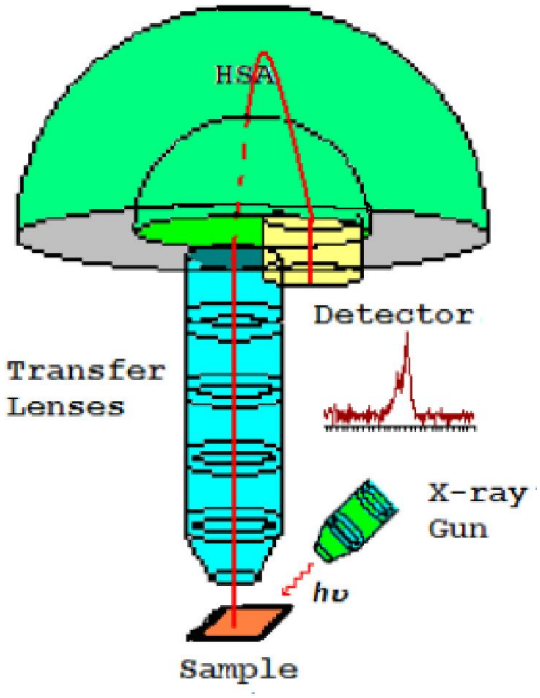

Fig. 4.10: Schematic diagram of XPS instrument [22].

XPS is a quantitative technique in the sense that the number of electrons recorded for a given transition is proportional to the number of atoms at the surface. In practice, however, to produce accurate atomic concentrations from XPS spectra is not straight forward. The precision of the intensities measured using XPS is not in doubt; that is intensities measured from similar samples are repeatable to good precision. What may be doubtful are results reporting to be atomic concentrations for the elements at the surface. An accuracy of 10% is typically quoted for routinely performed XPS atomic concentrations. For specific carefully performed and characterised measurements better accuracy is possible, but for quantification based on standard relative sensitivity factors, precision is achieved not accuracy. Since many problems involve monitoring changes in samples, the precision of XPS makes the technique very powerful.

The first issue involved with quantifying XPS spectra is identifying those electrons belonging to a given transition. The standard approach is to define an approximation to the background signal. The background in XPS is non-trivial in nature and results from all those electrons with initial energy greater than the measurement energy for which scattering events cause energy losses prior to emission from the sample. The zero-loss electrons constituting the photoelectric peak are considered to be the signal above the background approximation. A variety of background algorithms are used to measure the peak area; none of the practical algorithms are correct and therefore represent a source for uncertainty when computing the peak area. Peak areas computed from the background subtracted data form the basis for most elemental quantification results from XPS. In this research PHI 5000 XPS Versa probe is used for recording the binding energies of electrons within the samples.

References:

[1] A. H. Wako, PhD Thesis, University of the Free State, 2015.

[2] http://www.nanoscience.gatech.edu/zlwang/research/afm.html.

[3] N. Jalili, K. Laxminarayana, Mechatronics 14, 907 (204).

[4] http://www.novascan.com/education/non_contact_mode_afm.php.

[5] L. D. Hanke, Handbook of Analytical Methods for Materials: Materials Evaluation and Engineering, 763, 449 (2009)

[6] E. Coetsee, PhD Thesis, University of the Free State, 2010.

[7] R. F. Egerton, Physical Principles of and Electron Microscopy, Springer, Canada, 2005.

[8] serc.carleton.edu/research_education/geochemsheets/techniques/SEM.html.

[9] cfamm.ucr.edu/documents/eds-intro.pdf.

[10] Description of EDS technique http://mee-inc.com/index.html.

[11] B. G. Yakobi, D. B. Holt and L. L. Kazmerski, Microanalysis of Solids, New York, Plenum Press, 1994.

[12] S. Shionoya, W. M. Yen, Phosphors Handbook, CRC Press, USA, 1998, 95.

[13] B. M. Mothudi, PhD Thesis, University of the Free State, 2009.

[14] R. W. Kelsall, I. W. Hamley and M. Geoghegan, Nanoscale Science and Technology, Wiley, 2005.

[15] M. S. Dhlamini, PhD Thesis, University of the Free State, 2008.

[16] http://www.jeol.co.jp/en/products/detail/JSM-7800F.html.

[17] J. N. Reddy and K.V.R. Murthy, Defect and Diffusion Forum, 357, (2014) 261.

[18] J. G. Sol'e. L E Baus'a, and D. Jaque, An Introduction to the Optical Spectroscopy of Inorganic Solids, 2005, 33.

[19] G Cao, Nanostructures and Nanomaterials, Synthesis, properties and applications, 6th edition, Imperial college press, London UK, 2004.

[20] B. D. Culity, Elements of x-ray diffraction, Addison-Wesley, 1956.

[21] S. K. Shaat, PhD Thesis, University of the Free State, 2013.

[22] www.casaxps.com/help_manual/casaxps2316_manual/xps_spectra.pdf.

Chapter 5

Thermally stimulated luminescence of $Y_2SiO_5:Ce^{3+}$ commercial phosphor powder and thin films

5.1 Introduction

Thermoluminescence (TL) is the thermally stimulated emission of light from a semiconductor or insulator following the previous absorption of energy from radiation [1-3]. The word phosphor refers to a luminescent material synthesized for the purpose of practical applications which converts absorbed energy into visible light [4-9].

Because of their excellent chemical stability, high luminescence efficiency and flexible emission colors with different activators, inorganic compounds doped with rare earth elements form an important class of phosphors [10, 11]. These phosphors have versatile applications, for example, in cathode ray tubes, photodiodes, lamps and x-ray detectors, bio-detectors, in lamp industries, color display, radiation dosimetry etc [12-16]. Rare earth activated yttrium silicate phosphor host material displays some exciting practical applications such as long lasting phosphorescence, lasers, X-ray imaging, plasma display panels (PDP), flat panel displays (FPD) and environmental monitoring and have recently attracted much attention [17-19]. Y_2SiO_5 can exist in x_1-monoclinic or x_2-moniclinic phases depending on the synthesis temperature. A high temperature synthesis leads to x_2-type whereas a low temperature synthesis forms the x_1-type [20].

Luminescent thin films have some advantages over powders, including superior adhesion to substrates and reduced out-gassing [21]. Therefore, the study of the luminescence properties of thin films is equally as important as powders. Mechanisms such as growing films with rougher surfaces, using a less absorbing substrate and optimizing parameters during deposition of the films reportedly improve the lower luminescence of thin films [21-22].

UV and X-ray irradiated TL properties of $Y_2SiO_5:Ce^{3+}$ phosphor prepared by solid state reaction and sol-gel methods were already studied [23-24]. However, the TL properties of commercially available silicate phosphor powder and its corresponding thin films have not been studied to the best of our knowledge. In addition, the previous study of UV-irradiated TL properties of this phosphor belongs to different polycrystalline phase of the phosphor powder (JCPDS card no. 36-1476) [23]. Generally,

different phases, synthesis and irradiation mechanisms result in different TL properties of a material [20].

Therefore, in this work, the effect of heating rate and UV dose on the TL properties of $Y_2SiO_5 : Ce^{3+}$ commercial phosphor is reported. The TL kinetic parameters such as the trap depth (E), the frequency factor (s) and the order of kinetics were also determined. The TL properties of the thin films of $Y_2SiO_5 : Ce^{3+}$ phosphor prepared by pulsed laser deposition (PLD) were also investigated. The films were prepared using various deposition parameters such as different oxygen gas pressures and background gas environments.

5.2 Experimental details

Pulsed laser deposition of commercially available $Y_2SiO_5 : Ce^{3+}$ standard phosphor powder from Phosphor Technology (UK) Ltd was performed with Nd-YAG laser radiation ($\lambda = 266\,\text{nm}$, pulse duration of 9.3 nm, repetition rate of 10 Hz) on (100) silicon substrates. The powder was pressed in to a pellet and annealed at $300°\,\text{C}$ for removal of any water vapor. The laser fluence, energy and the target to substrate distance, respectively, were kept at $4\,\text{J/cm}^2, 40\,\text{mJ}$ and 4.2 cm. The vacuum chamber was pumped to a background pressure of 5.6×10^{-3} Pa before introducing argon and oxygen. In all the measurements, the substrate temperature was kept at $350\,°\,\text{C}$. The structure of phosphor powder and its corresponding thin films were studied by X-ray diffraction (XRD) using a Bruker D8 X-ray advance diffractometer operating at 40 kV and 40mA using Cu $k_\alpha = 0.15406\,\text{nm}$. In TL measurements, a UV source was used for TL excitation prior to heating. The TL measurements were taken using TL reader type TL1009I offered by Nucleonix systems Pvt. Ltd., India interfaced to a PC where the TL signals were analyzed.Samples were heated from 0 to $400\,°\,\text{C}$ at various heating rates and for various UV doses.

5.3 Results and discussion

5.3.1 Thermoluminescence study of $Y_2SiO_5 : Ce^{3+}$ phosphor powder

5.3.1.1 Effect of heating rate

To analyze the effect of heating rate on TL intensity, the TL measurements were taken at seven different heating rates of $0.5°\,\text{C/s}, 0.8°\,\text{C/s}, 1°\,\text{C/s}, 1.2°\,\text{C/s}, 1.5°\,\text{C/s}, 1.8°\,\text{C/s}$ and $2°\,\text{C/s}$. Figure 5.1 depicts the TL intensity versus temperature of $Y_2SiO_5 : Ce^{3+}$ for the different heating rates and at constant UV exposure time of 10 minutes. It can be clearly observed that the intensity maximum shifts to higher temperatures as the heating rate increased. Moreover, decrease of the glow peak height was observed

with increasing heating rate and this could be attributed to thermal quenching effect in which the efficiency of the luminescence decreases as the temperature increases due to opening up of competing non-radiative relaxation pathways [23].

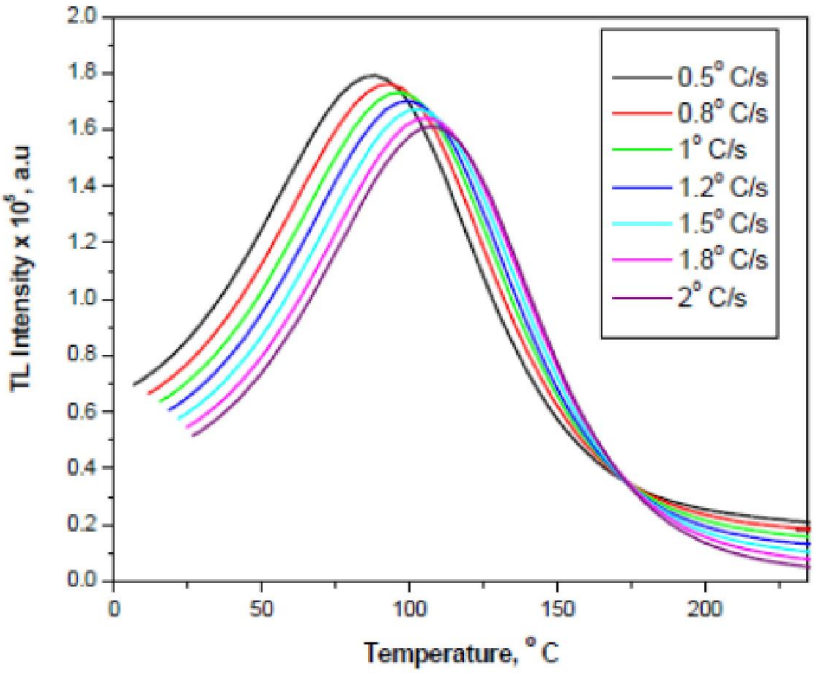

Fig. 5.1: The TL intensity versus temperature of the phosphor for different heating rates.

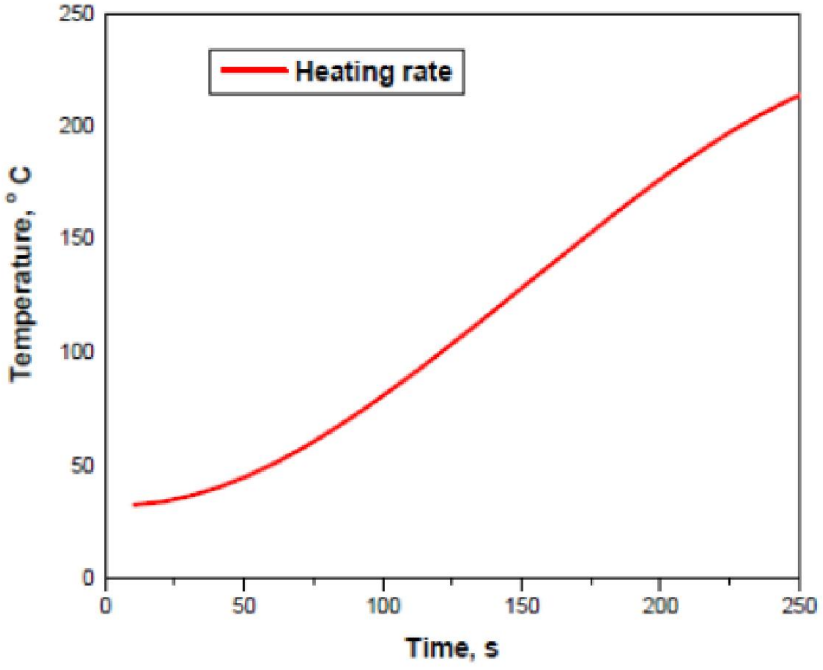

Fig. 5.2: The profile of the heating rate used during TL experiment.

Further evidence for the presence of thermal quenching effect was confirmed by the observation of the decrease in the area of $\frac{TL}{\beta}$ versus temperature plot with increasing heating rate at constant UV dose [25-26]. In literature there are reports where the decrease in intensity is significantly larger due to thermal quenching effects [25-26]. However, in this study, the decrease in intensity is not large and, therefore, it could be attributed to the narrow heating rates used during the TL measurements. It is worth noting that the initial non-zero TL intensity could be attributed to UV induced shallow traps with peak temperatures at, or below, room temperature. Linear heating rates were used in this work and the linearity of the temperature ramp is shown in Figure 5.2. Slight deviation from linearity was observed and this could be due to the low temperature sensitivity of the TL reader.

Analysis of the evolution of the TL maximum with the heating rate determines the TL kinetic parameters; namely the activation energy (E), the frequency factor (s) and the order of kinetics. Variable heating rate (VHR) analysis was performed in order to consider how the traps are emptied at different heating rates while all the other parameters are held constant. The heating rate β can be related to the position of the TL maximum T_M of its corresponding peak using an equation of the following form [9-10]:

$$\frac{\beta E}{kT_M{}^2} = s \exp\left(-\frac{E}{kT_M}\right) \qquad (5.1)$$

where k is the Boltzmann constant (in units of eV/K) and E is the activation energy (in units of eV). Change in the linear heating rate β results in the change of the temperature T_M of the maximum TL intensity of the peak: faster heating rates produce shifts in temperature relatively towards higher values of T_M but with reduced peak intensity as shown in Figure 5.1. When $\ln\left(\frac{T_M{}^2}{\beta}\right)$ is plotted against $\frac{1}{kT_M}$, the resulting graph consists of a straight line of slope E and intercept (on $\ln\left(\frac{T_M{}^2}{\beta}\right)$ axis) $\ln\left(\frac{E}{Sk}\right)$. The value of the frequency factor (s) was determined from the value of this intercept. The temperature T_M for the maximum TL intensity corresponding to each heating rate and the calculation of $\ln\left(\frac{T_M{}^2}{\beta}\right)$ and $\frac{1}{kT_M}$ is shown in Table 5.1. The values listed in the table are subject to a known experimental uncertainty of $\Delta T = 0.4\,^{\circ}K$ during the measurements. This induces the uncertainty of ± 0.002 and ± 0.03 in the evaluated values of $\ln\left(\frac{T_M{}^2}{\beta}\right)$ and $\frac{1}{kT_M}$ respectively.

Table 5.1: The calculation of $\ln\left(\frac{T_M{}^2}{\beta}\right)$ and $\frac{1}{kT_M}$.

β (° C/s)	T_M(° C)	T_M(° K)	$\ln\left(\frac{T_M{}^2}{\beta}\right)$	$\frac{1}{kT_M}(eV^{-1})$
0.5	88.34	361.34	12.47	32.12
0.8	93.71	366.71	12.03	31.65
1	97.29	370.29	11.83	31.34
1.2	100.63	373.63	11.66	31.06
1.5	103.54	376.54	11.46	30.82
1.8	106.15	379.15	11.29	30.61
2	108.04	381.04	11.19	30.46

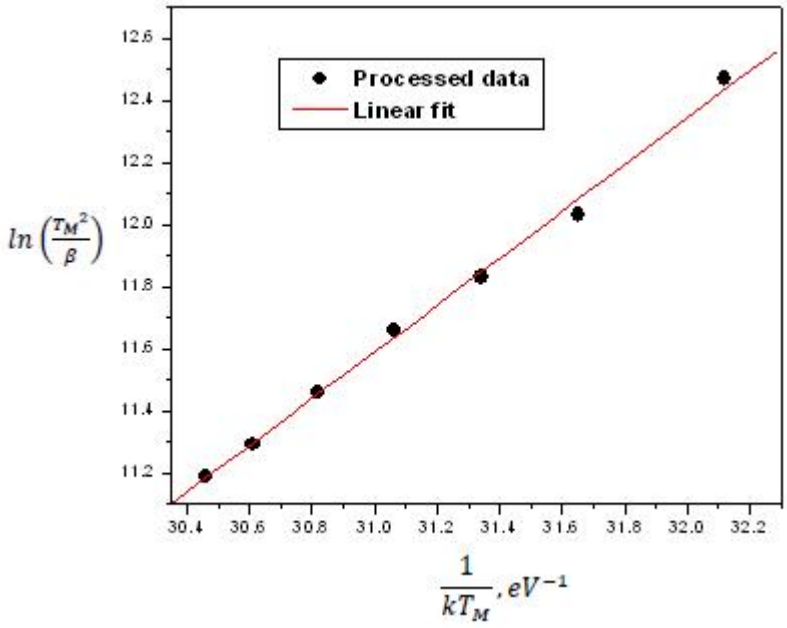

Fig. 5.3: The graph of calculation of $\ln\left(\frac{T_M{}^2}{\beta}\right)$ and $\frac{1}{kT_M}$ to determine E and s. The processed data is shown by the dots.

From the slope and intercept of the graph $\ln\left(\frac{T_M{}^2}{\beta}\right)$ versus $\frac{1}{kT_M}$ in Figure 5.3, the kinetic parameters E and s were calculated. The calculated values are $E = 0.75 \pm 0.021$ eV and $s = (1.15 \pm 0.69) \times 10^9\ s^{-1}$. Y. Parganiha et al., reported that the values of E and s for $Y_2SiO_5 : Ce^{3+}$ prepared by solid state reaction method are of the order of 0.7eV and $10^8\ s^{-1}$ respectively [23] while A. Meijerink et al., reported $E = 0.82$ eV and $s = 9 \times 10^9\ s^{-1}$ [24]. These two observations are in a good agreement with our results.

Equation (1) holds exactly for first order kinetics, though it is also good approximation for other kinds of kinetics [1]. To justify the assumption of first order kinetics, the sample was exposed to varying UV exposure times (doses) varying from 10-30 minutes (see Figure 5.4). It was observed that all the glow peaks obtained for various UV doses attained their maxima at the same temperature confirming the assumption of first order kinetics [3].

5.3.1.2 Effect of UV dose

Figure 5.4 shows the TL intensity of the phosphor powder for different UV doses while fixing heating rate at $1.2\ ^{\circ}\mathrm{C/s}$. It was observed that the TL intensity of the powder increased with UV dose up to 20 minutes and then decreased. The dose response curve is linear up to 20 minutes and sub-linear over the range 20-30 minutes as shown in the inset of Figure 4. There was no observed shift of the TL peak positions due to the variation of the UV exposure. Y. Parganiha et al., investigated the TL intensity of $Y_2SiO_5 : Ce^{3+}$ phosphor prepared by solid state reaction method and found that the intensity increased up to 20 minutes of UV exposure time and then decreased [23]. In this study, the observed decrease in the TL peak intensity after 20 minutes could be attributed the UV induced non-radiative recombination centers that could result in the decrease in the TL signal at higher doses.

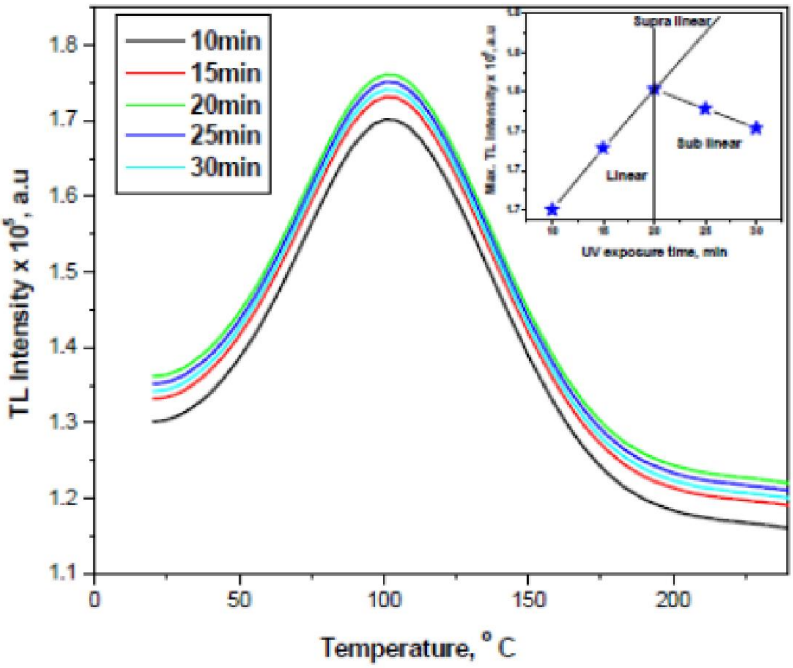

Fig. 5.4: The TL peak intensity of $Y_2SiO_5 : Ce^{3+}$ phosphor powder against UV exposure time. The inset is included for elaboration.

5.3.2 Thermoluminescence study of $Y_2SiO_5 : Ce^{3+}$ phosphor thin films

5.3.2.1 Effect background gas pressure

The influence of oxygen gas pressure on the TL properties of the deposited films was also investigated. The deposition was made for various oxygen pressures of 1.3 Pa, 6.7 Pa and 22.6 Pa. Figure 5.5 shows the effect of oxygen pressure on the TL glow curve intensities of $Y_2SiO_5 : Ce^{3+}$ phosphor powder thin films for 10 minutes of UV dose and heating rate of 1° C/s. The increase in oxygen pressure resulted in an increase in the TL intensity of the thin films. Similar results of enhancement in luminescence of thin films at higher oxygen pressures were reported in literature [21-22]. In this study, the increment in the TL intensity at higher oxygen pressure is attributed to the increase in surface roughness of the films at such higher pressures. The rough surface reduces the total internal reflection thereby enhancing luminescence intensity [21-22]. There was no observed appreciable glow peak shift for all the pressures applied. The TL emissions observed are, in general, broad over a wide temperature range.

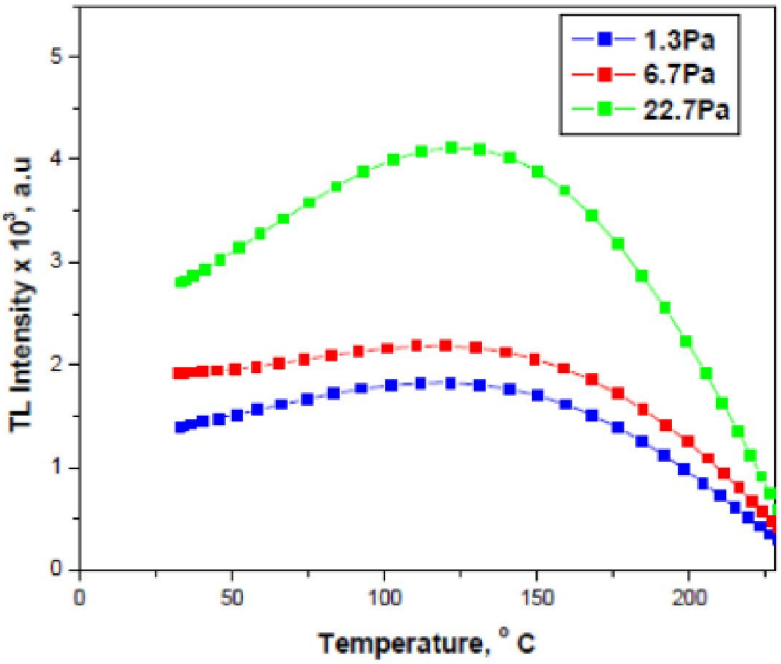

Fig. 5.5: The effect of background gas pressure on the TL intensity of $Y_2SiO_5 : Ce^{3+}$ phosphor thin films.

5.3.2.2 Effect of different gas atmospheres

To investigate the effect of various background gas atmospheres on the TL properties of the prepared thin films, the deposition was made with oxygen, argon and vacuum as background atmospheres. Figure 5.6 shows the effect of different background gas atmospheres on the TL intensity of the films. High TL

intensity was obtained for the film deposited using argon as a background gas. This could be attributed to the improved crystallinity of the film. In general, the TL properties of thin film phosphors are improved following improvement in crystallinity [27-28]. As shown in Figure 5.8, the film with improved crystallinity was obtained when argon was used as a background gas. As discussed before, the initial non-zero TL intensity could be attribute to the UV induced shallow traps with peak temperatures at or below room temperature.

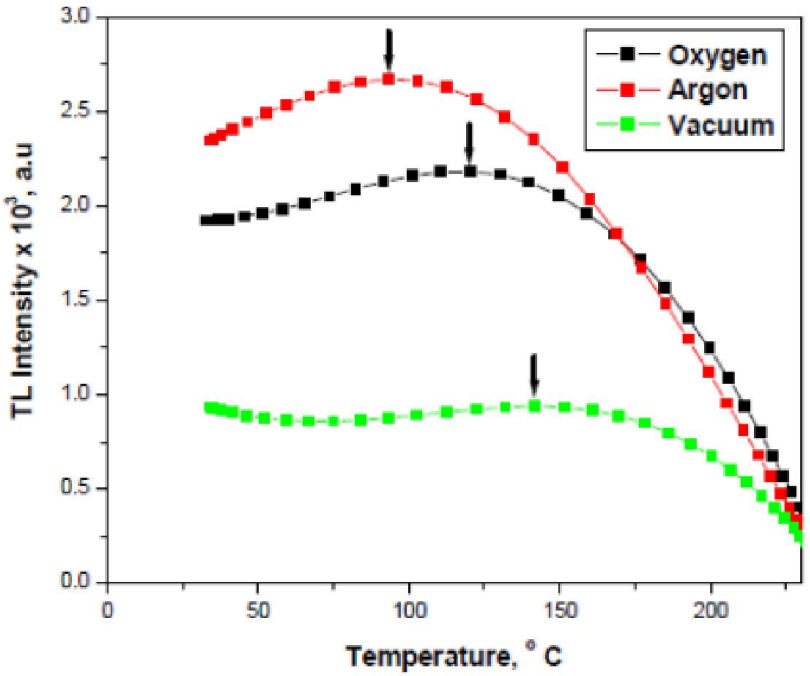

Fig. 5.6: The effect of background gas atmosphere on the TL intensity of $Y_2SiO_5 : Ce^{3+}$ phosphor thin films. The maxima of the glow peaks are indicated by arrows.

The maxima of the TL glow peaks of the films deposited in oxygen and vacuum shift towards higher temperature relative to the TL maximum of the film deposited in argon. This could be attributed to the relatively deep traps formed for deposition in oxygen and vacuum environments. Vacuum environment resulted in the formation of deep trap as compared to oxygen and argon environments.

5.3.3 Structural properties of $Y_2SiO_5 : Ce^{3+}$ phosphor powder and thin films

Figure 5.7 shows the XRD pattern of $Y_2SiO_5 : Ce^{3+}$ phosphor powder and it reveals x_2-monoclinic polycrystalline phase with the maximum peak centered at $2\theta = 37^{\circ}$. The pattern corresponds to monoclinic phase with JCPDS No 21-1458 in the reference data. This structure of $Y_2SiO_5 : Ce^{3+}$ phosphor powder is different from the previously studied one. As compared to the previously studied powders [23-24], this structure gives intense TL emissions and is highly efficient TL material. The average crystallite size of the phosphor was estimated from the most intense XRD peaks using Sherrer's equation which is given by [29]:

$$D = \frac{0.89\lambda}{\beta \cos\theta_B} \qquad (5.2)$$

where D is the average crystallite size, λ is the incident wavelength of Cu K_α radiation (1.54 Å), β is the full width at half maximum (in radians) and θ_B is the Bragg angle.

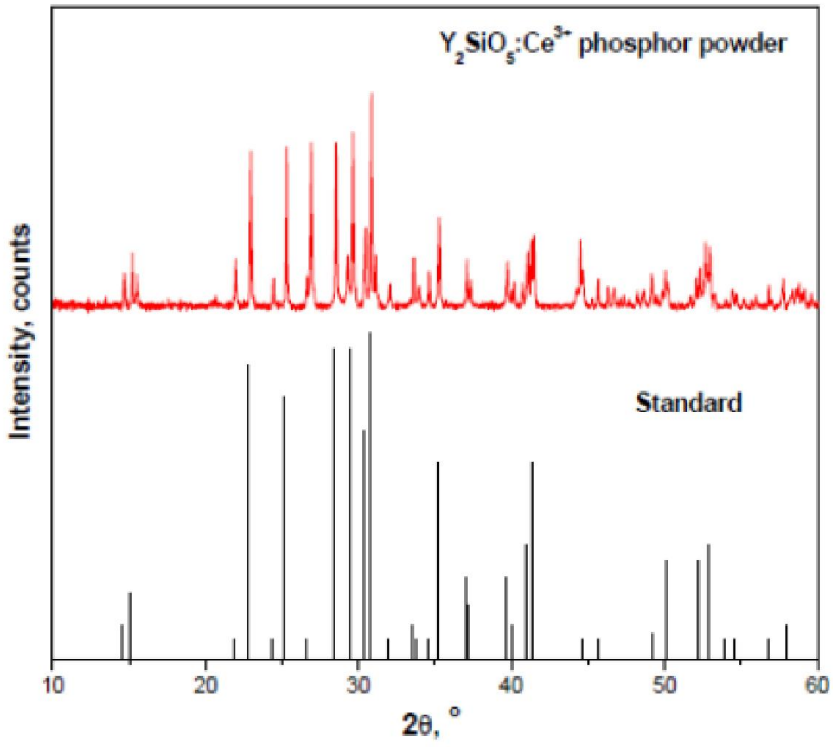

Fig. 5.7: XRD pattern of $Y_2SiO_5 : Ce^{3+}$ phosphor powder. The spectrum of the standard is included for comparison.

The average crystallite size of the phosphor was found to be 61.2 nm. Figure 5.8(a) depicts the structure of the films deposited at various oxygen gas pressures at constant substrate temperature of 350 ° C. The experimental pattern matches well with x_1-monoclinic polycrystalline phase with JCPDS card 74-1266. The film deposited at a pressure of 22.7 Pa is amorphous. As the pressure is reduced to 6.7Pa some diffraction peaks appeared and with further reduction in pressure to 1.3 Pa, more peaks became visible. This clearly shows that deposition pressure has clear effect on the crystallinity of the deposited films. It can be observed that the film deposited at pressure of 1.3 Pa is more crystalline than those deposited at 6.7 and 22.7 Pa. We present this improvement in the crystallinity of the film at low pressure of 1.3 Pa in terms of the actual surface temperature of the film which is because of two factors. The first factor is the temperature of the substrates, which is 350 ° C in our case, and the second factor is the kinetic energy of the vapor species striking the surface [30]. At relatively lower pressure, the ablated target species face low resistance from the gas molecules and strike the substrate with relatively high kinetic energy. Therefore, the film deposited at a pressure of 1.3 Pa has the highest actual surface temperature as compared to the other films. This high temperature increases surface mobility which, in turn, increases the crystallinity of the film.

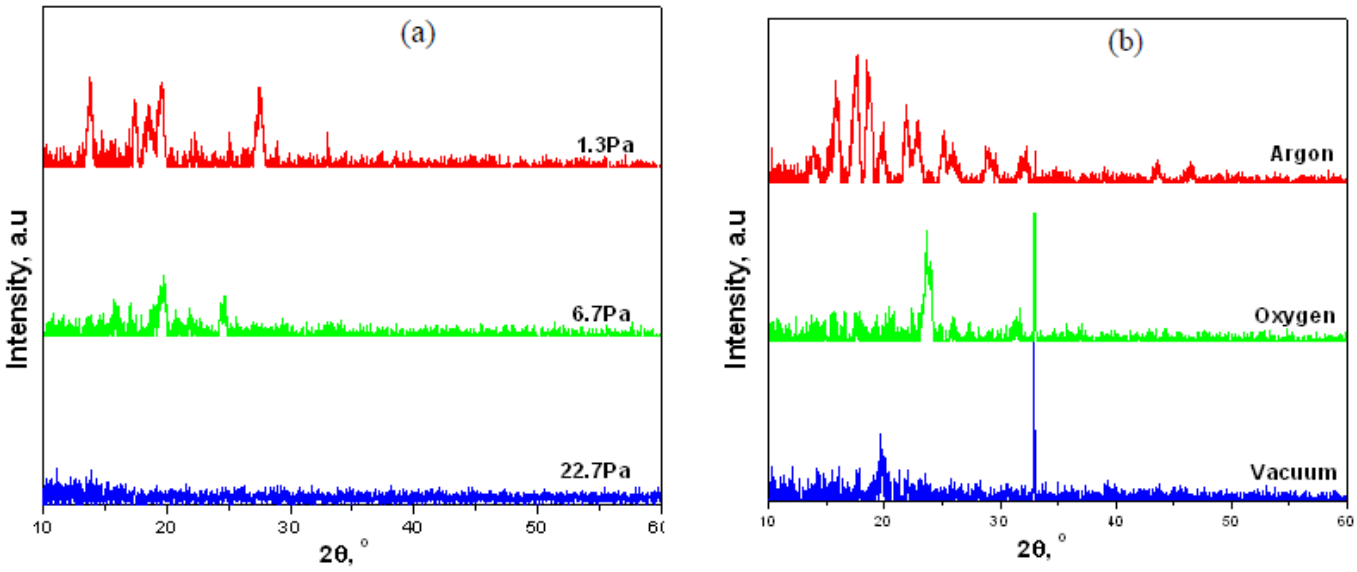

Fig. 5.8: XRD pattern of $Y_2SiO_5 : Ce^{3+}$ phosphor thin films (a) deposited at different oxygen pressures and (b) deposited in various background gas environments.

The XRD pattern (x_1-monoclinic polycrystalline phase) of the films deposited in various background gas atmospheres is shown in Figure 5.8(b). There is a high correlation with JCPDS card 74-1266. The oxygen and argon pressures were kept at 22.7 Pa during deposition for one hour. Relatively more diffraction peaks appeared for the film deposited using argon as a background gas. This shows that the film deposited using argon as a background gas is more crystalline than films deposited in oxygen and vacuum. This improvement in crystallinity is the cause of the higher TL intensity observed for the film prepared using argon as a background gas. The average crystallite size of the films determined from the most intense peaks using Scherrer's equation varied between 19.4-78.6 nm. The formation of x_1-monoclinic polycrystalline phase for all the films was expected at low deposition temperature ($350\,^\circ\mathrm{C}$) used during the experiment.

Conclusion

The TL properties and structure of $Y_2SiO_5:Ce^{3+}$ commercial phosphor powder and its corresponding thin films prepared by pulsed laser deposition were studied. For the phosphor powder, the TL intensity increases with an increase in UV exposure time for up to 20 minutes and then decreases. The TL intensity peak shifts slightly to higher temperature region for relatively high heating rates, but with reduced intensity peak. The decrease in TL intensity at high heating rates could be ascribed to thermal quenching effect, in which the efficiency of the luminescence decreases as the temperature increases due to opening up of competing non-radiative relaxation pathways. Important TL kinetic parameters, such as the activation energy (E) and the frequency factor (s) were calculated from the glow curves using variable heating rate (VHR) method. The variations of gas pressure and background gas atmosphere have also significant effect on the TL intensities and structure of the thin films. The highest TL intensity was obtained for the film deposited using argon as a background gas. Moreover, increase in oxygen pressure resulted in an increase in TL intensity of the films.

References

[1] S. McKeever, Thermoluminescence of solids (London, Cambridge University Press, 1983), pp. 1-50.

[2] M. Karmakar, Indian J. Phys. 84, 529 (2010).

[3] V. Pagonis, G. Kitis and C. Furetta, Numerical and Practical Exercises in Thermoluminecsnce (USA, Springer, 2006), pp. 1-100.

[4] P. Kumari, P. Baitha, J. Manam, Indian J. Phys. 89, 1297 (2015).

[5] E. Raja, B. Dhabekar, S. Menon, S. More, T. Rao, R. Kher, Indian J. Pure Ap. Phy. 47, 420 (2009).

[6] A. Singh, S. Singh, L. Singh, Indian J. Phys. 89, 41 (2015).

[7] M. Sahini, H. Wagiran, I. Hossain, M. Saeed, H. Ali, Indian J. Phys. (2014).

[8] J. Manam, S. Das, Indian J. Pure Ap. Phy. 47, 435 (2009).

[9] Y. Parganiha, J. Kaur, V. Dubey D. Chadrakar, Superlattice. Microst. 77, 152 (2015).

[10] A. Srivastava, C. Ronda, Luminescence from Theory to Applications (Germany, Wiley, 2007), pp. 10-100.

[11] D. Cooke et al., Appl. Phys. Lett. 88, 103 (2006).

[12] H. Huang, B. Yan, Solid State Commun. 132, 773 (2004).

[13] T. Bottger, C. Thiel, R. Cone, Y. Sun, Phys. Rev. B 79, 115104 (2009).

[14] B. Comaskey et al., Opt. Lett. 18, 2029 (1993).

[15] B. Lauritzen et al., Phys. Rev. Lett. 104, 080502(2010).

[16] Z. Cole et al., Appl. Phys. Lett. 81, 3525 (2002).

[17] Y. Ogura, M. Kondo, T. Morimoto, A. Notomi, T. Sekigawa, Mater. Trans. 42, 1124 (2001).

[18] H. Bryan, P. Gallagher, G. Berkstresser, J. Am. Ceram. Soc. 71, 42 (1988).

[19] M. Apricio, A. Duran, J. Am. Ceram. Soc. 83, 1351(2000).

[20] X. Qin, Y. Ju, S. Bernhard, N. Yao, Mater. Res. Bull. 42, 1440 (2007).

[21] J. Dolo et al., Appl. Phys. A 101, 655 (2010).

[22] K. Hillie, H. Swart, Appl. Surf. Sci. 183, 304 (2001).

[23] Y. Parganiha, J. Kaur, V. Dubey, D. Chandrakar, N. Suryanarayana, Research Chem. Intermed. 42, 2267 (2015).

[24] A. Meijerink, W. Schipper, G. Blasse, J. Phys. D: Appl. Phys. 24, 997 (1991).

[25] M. Kumar, G. Chourasiya, Meas. Sci. Technol. 20, 058001 (2009).

[26] M. Kumar, G. Chourasiya, B. Bhatt, C. Sunta, J. Lumin. 130, 1216 (2010).

[27] Q. Shi et al., Thin Solid Films, 520, 6845(2012).

[28] H. Yang, J. Korean Phys. Soc. 53, 1430 (2008).

[29] B. Cullity, Elements of X-ray Diffraction, Addison-Wesley publishing (USA) PP. 99.

[30] A. Dikovska, P. Atanasov, C. Vasilev, I. Dimitrov, T. Stoyanchov, J. Optoelectron. Adv. M. 7, 1329 (2005).

Chapter 6

Thermoluminescence and photoluminescence study of $KY_3F_{10}:Ho^{3+}$ commercial phosphor powder

6.1 Introduction

Potassium triyttrium decafluoride (KY_3F_{10}) has attracted much attention and has been extensively studied because of its excellent optical properties [1-2] and potential applications in a wide range of fields: laser applications [2], scintillation [3] and display devices [4-5]. It also possesses low-maximum phonon frequency leading to a large number of potential emitting levels as well as high luminescent efficiency [6-13]. Compared to other low phonon energy materials such as chlorides, bromides, or sulphides, the fluorides present a reasonably high thermal conductivity, a good enough mechanical hardness, and a high chemical stability [9-14]. The KY_3F_{10} phosphor is a single-site host material for rare-earth ions to occupy which ensure homogeneously broadened absorption and emission spectra. This last point is especially crucial to investigate the multipolar interactions between ions. In addition to all the aforementioned interesting properties, KY_3F_{10} has much higher energy transfer efficiency in it than other fluorides such as BaY_2F_8 and $LiYF_4$ [8], this makes it an interesting material for luminescence applications.

The KY_3F_{10} and family are usually doped with various trivalent rare earth ions such as $Eu^{2+}, Tb^{3+}, Pr^{3+}, Sm^{3+}$ in order produce phosphors with improved luminescence property for different applications [9-15]; though still these studies do not focus on its TL properties.

Holmium as an activator has significant advantage over other rare earth ions because of its high-gain cross section and long life time of $^5I_7$ upper level emission resulting in high energy storage capability and efficiency [16]. Although studies on the structural and optical properties of $KY_3F_{10}:Ho^{3+}$ crystals have been made, to the best of our knowledge, TL and PL studies of UV irradiated $KY_3F_{10}:Ho^{3+}$ phosphor powder has not been studied. In this work, therefore, the investigation of luminescence properties of $KY_3F_{10}:Ho^{3+}$ commercial phosphor is presented and important TL kinetic parameters such as activation energy (E) and the frequency factor (s) were determined.

6.2 Experimental details

Commercially available $KY_3F_{10}:Ho^{3+}$ standard phosphor powder from phosphor technology (UK) was stored in a transparent sample glass bottle for characterization. The crystal structure of this material was studied by X-ray diffraction (XRD) using a Bruker D8 advance X-ray diffractometer operating at 40 kV and 40 mA using $\mathrm{Cu\ k}\alpha = 0.15406$ nm. The morphology and composition were studied using high resolution Transmission Electron Microscope (TEM) and Energy Dispersive X-ray Spectrometer (EDS), respectively. The excitation and emission spectra as well as the PL decay lifetime were measured at room temperature using Cary Eclipse fluorescence spectrometer model: LS-55 with a built-in 150W xenon flash lamp. For TL measurements, the samples were prepared into discs of 5 mm in diameter and 1 mm thick. A UV source was used for TL excitation prior to heating. TL measurements were taken using a Riso model TL/OSL-DA-20 luminescence reader. The TL is detected using TL reader type TL1009I offered by Nucleonix systems Pvt. Ltd., India interfaced to a PC where the TL signals were analyzed. Samples were heated from 0 to 400 ^{o}C at various heating rates and for different UV doses. TL measurements were done immediately after stopping the UV exposure.

6.3 Results and discussion

6.3.1 Structural characterization

Figure 6.1 depicts the XRD pattern of $KY_3F_{10}:Ho^{3+}$phosphor powder. The pattern exhibits the existence of almost pure KY_3F_{10} phase with minimum impurity. The miller indices of the diffraction peaks were labeled according to the diffraction planes. It shows tetragonal structure with space group of Fm3m, a C_{4v} symmetry and lattice constants $a = 11.6$ Å and $c = 11.5$ Å and cell volume 1552.8 Å^3 match with JCPDS card No 27-0465. The average crystallite size was calculated from the most intense peaks using equation (5.2).

The average crystallite size of the phosphor was found to be 64 nm. Figure 6.2 shows the TEM micrograph of the sample which reveals the formation of polycrystalline material with irregular grain size and shape distributions. The average grain size is in sub-micrometer range possibly due to agglomeration of smaller grains which form thorough crushing and high temperature processing of the samples. The elemental analysis of the commercial $KY_3F_{10}:Ho^{3+}$ phosphor was performed using the EDS technique and the measured EDS quantitative data is shown in Table 6.1. There appeared no other emissions apart from K, Y, and F in the EDS results of the sample. The non existence of any amount of doped rare earth active ion of Ho^{3+} in the sample is clear indication that Ho^{3+}concentration in the

sample is below the sensitivity of the instrument. With in the limits of the EDS experimental error, the elements appear in ratios similar with the proportions of $KY_3F_{10}:Ho^{3+}$ phosphor material. EDS makes use of the x-ray spectrum emitted by a solid sample bombarded with a focused beam of electrons to obtain a localized chemical analysis. All elements from atomic number 4 (Be) to 92 (U) can be detected in principle, though not all instruments are equipped for 'light' elements (Z < 10). Part of the sample as small as 1 μm can be analyzed using this technique. Qualitative analysis involves the identification of the lines in the spectrum and is fairly straightforward owing to the simplicity of x-ray spectra. Quantitative analysis (determination of the concentrations of the elements present) entails measuring line intensities for each element in the sample.

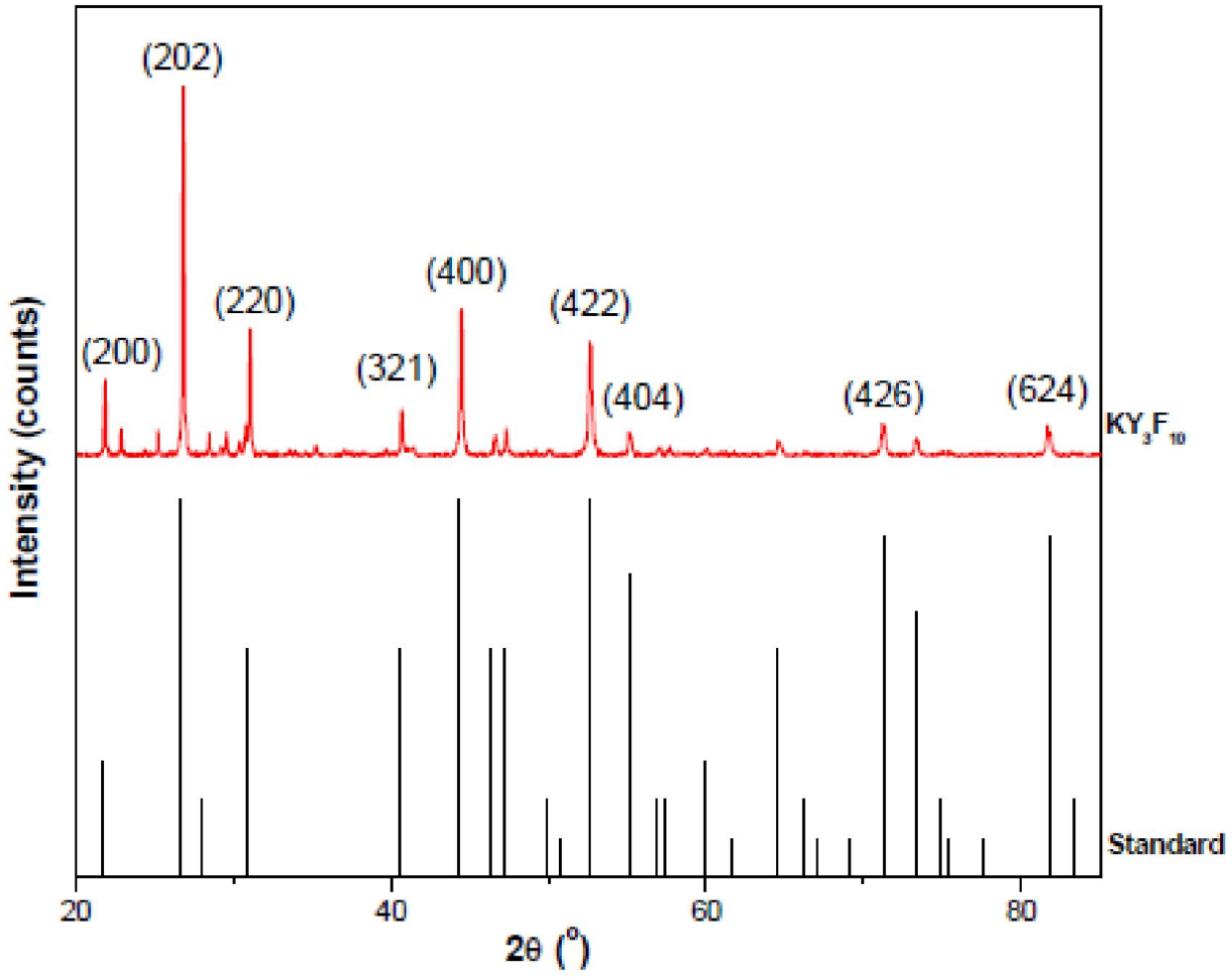

Fig. 6.1: X-ray powder diffraction of $\mathbf{KY_3F_{10}:Ho^{3+}}$ phosphor powder with miller indices of most prominent peaks. The spectrum of the standard is included for comparison.

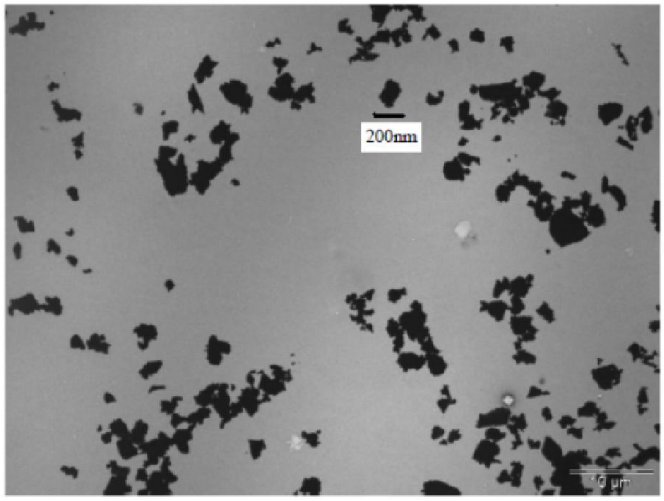

Fig. 6.2: TEM image of $KY_3F_{10}:Ho^{3+}$ phosphor powder.

Table 6.1: EDS results of $KY_3F_{10}:Ho^{3+}$ phosphor powder.

No.	Elements	Weight %
1	Potassium (K)	9.3%
2	Yttrium (Y)	54.8%
3	Fluorine (F)	35.9%

6.3.2 Thermoluminescence study

6.3.2.1 Effect of UV dose

Figure 6.3 shows the TL intensity of the phosphor powder (in photons per degree) for various UV exposure times, while fixing heating rate at $1.2\ ℃/s$. It is observed that the intensity peak from the powder increases with UV exposure time up to 20 minutes and then decreases as indicated in Figure 6.4. R. K. Tamrakar et al., investigated the TL intensity of $Gd_2O_3:Er^{3+}$ phosphor and found that the intensity increases up to 15 minutes UV exposure time and then decreases [17]. Chen et. al., Y. Parganiha et al. and N. Tewari et al., also reported such non-monotonic dose dependence of TL from different materials [18-20]. In this study the TL intensity is found to be linear with the UV dose up to 20 minutes as mentioned above. The early observation of the decrement in TL intensity at high UV doses, for example, by Charlesby and Partridge [21] and Jain et al. [22] was ascribed to radiation damage. Chen et al., [18], through their numerical simulation results, suggested a rather general and interesting model which does not assume radiation damage or destruction of trapping or recombination centers.

/

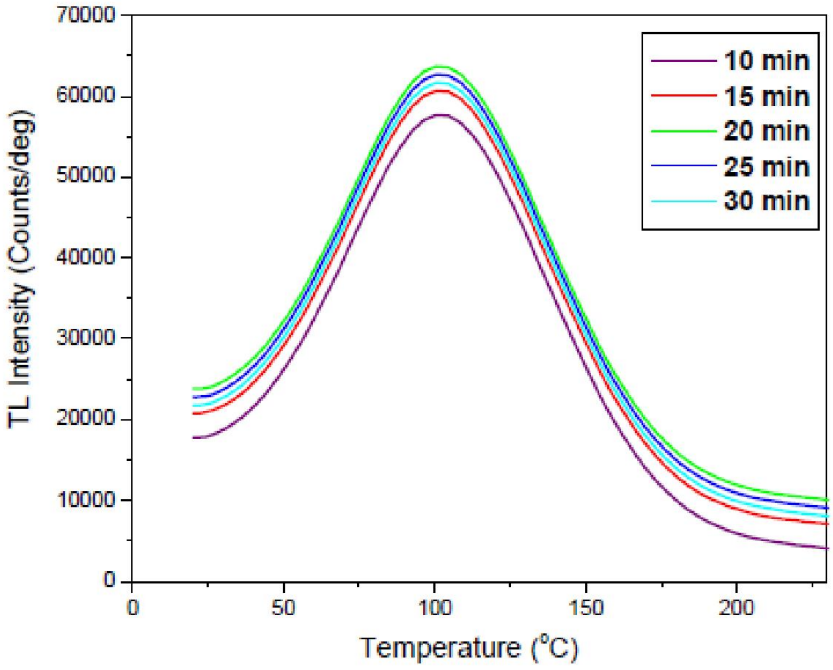

Fig. 6.3: The effect of UV exposure time on TL intensity of KY_3F_{10}: Ho^{3+}phosphor powder. As shown, the intensity increases up to 20 minutes of UV exposure time and then decreases.

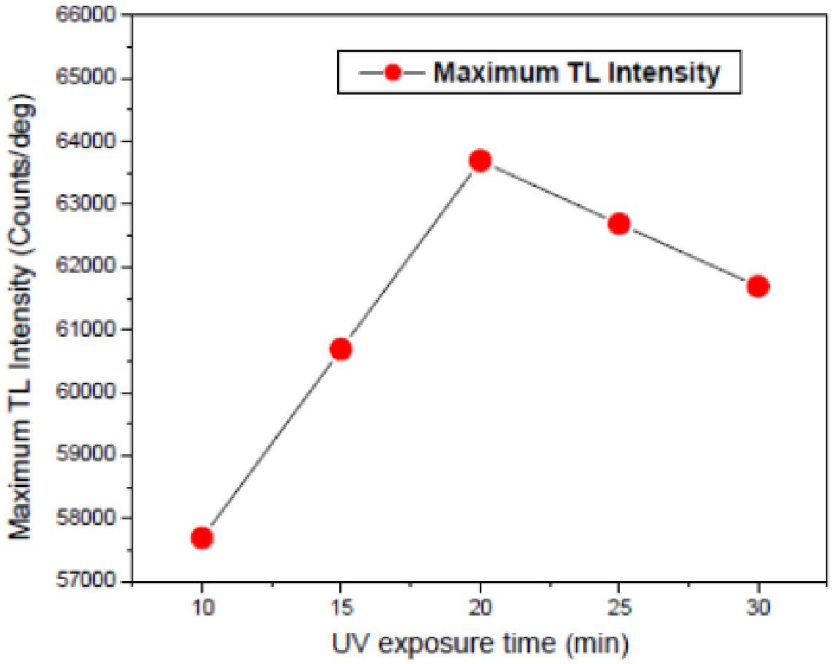

Fig. 6.4: Variation of the peak values of the glow curves (represented by the dots) with UV exposure time. Lower peak values were obtained for 25 and 30 minutes UV dose.

They considered two trapping states (one being thermally disconnected deep trap) and two kinds of recombination centers (one being a non-radiative center) which are practically present in any thermoluminescent material. According to Chen et al., the decrease of the TL signal can be attributed to the stronger competition with non-radiative centers at higher doses. In this study, the observed decrement in the TL peak intensity after 20 minutes could also be attributed to such strong competition at higher UV doses. In addition, there could be UV induced non-radiative recombination centers that could result in the decrease in the TL signal at higher doses. It is interesting to note that there was no observed shift of the intensity peak positions to high or low temperature region due to the variation of the UV dose.

6.3.2.2 Effect of heating rate

Heating rate (β) is an important parameter for the determination of the various kinetic parameters of TL glow curves. In literature it has been reported that the glow peak height decreases [23] or increases [24-26] with increasing heating rate. In some cases, the decrease in the glow peak height with increasing heating rate may wrongly be attributed to thermal quenching effect. M. Kumar et. al., sorted out the ambiguity on the effect of heating rate on TL glow curves by presenting the variation of the glow peak height as well as the area under the glow curve with increasing heating rates [26-28]. According to M. Kumar et al., the observation of decrease of the area under the TL-time plot or the area under $\frac{\mathrm{TL}}{\beta}$-temperature plot with increasing heating rate at constant dose is the correct way of predicting the presence of thermal quenching effect.

In this study, to analyze how the TL intensity varies with the heating rate, measurements were made at seven different heating rates of $0.5\ ^{0}\mathrm{C/s}, 0.8\ ^{o}\mathrm{C/s}, 1^{o}\mathrm{C/s}, 1.2\ ^{o}\mathrm{C/s}, 1.5\ ^{o}\mathrm{C/s}$, and $1.8\ ^{o}\mathrm{C/s}$ and $2\ ^{o}\mathrm{C/s}$. Figure 6.5 shows the TL intensity versus temperature of $KY_3F_{10}:Ho^{3+}$ for different heating rates and constant 10 minutes of UV dose. As expected, the intensity maximum shifted to higher temperatures as the heating rate was increased. Moreover, decrease of the glow peak height was observed the glow curves with increasing heating rate. This phenomenon does not necessarily indicate the presence of thermal quenching effect [27-28]. Therefore, evaluation of the area under TL-time or $\frac{\mathrm{TL}}{\beta}$-temperature plots becomes mandatory to check whether the decrease in the intensity of the glow peaks is due to thermal quenching effect or not. In this study, the area under TL-time plot is calculated for each heating rate at constant UV dose and it is found to be constant and independent of heating rates.

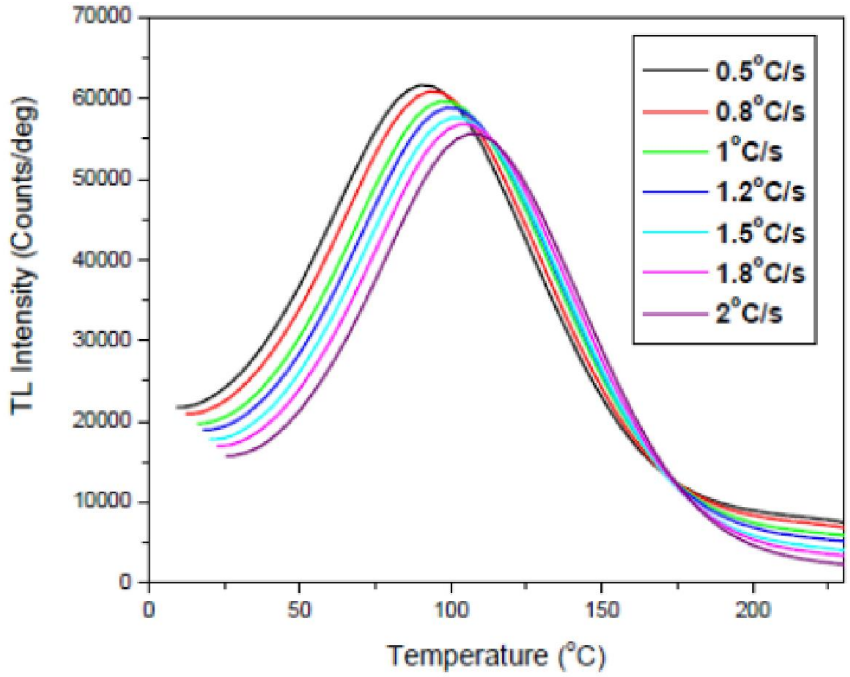

Fig. 6.5: TL Intensity versus temperature of KY_3F_{10}: Ho^{3+} for different heating rates. As indicated, the peak of the glow curves decrease and shift to higher temperature region with increasing heating rate. The initial non-zero values of the intensity indicate fluorescence during irradiation.

Thus, the observed decrement in intensity of each glow curve following increment in heating rate is not attributed to the thermal quenching effect. Moreover, in this study, the decrement in the intensity of TL glow curves with increase in heating rate is not significantly larger. In literature there are reports that in case of thermal quenching effects, the decrease in intensity is significantly larger [27-28]. The phenomenon of the observed non-zero initial TL intensity at low temperature is reported in literature [17]. It could be attributed to the UV induced shallow traps with peak temperatures at or below room temperature. Such radiation induced defects are also reported for different materials [17, 29].

The heating rate (β) can be related to the T_M of its corresponding intensity peak using an equation of the following form for first order kinetics [30]:

$$\frac{E}{kT_M{}^2} = s \times \exp\left(-\frac{E}{kT_M}\right) \qquad (6.1)$$

where k is the Boltzmann constant (in units of eV/K) and E is the activation energy (in units of eV).

The assumption of first order kinetics is justified by the fact that during exposure of the sample to varying UV doses, all glow peaks attained their maxima at the same temperature (see Fig. 6.3).

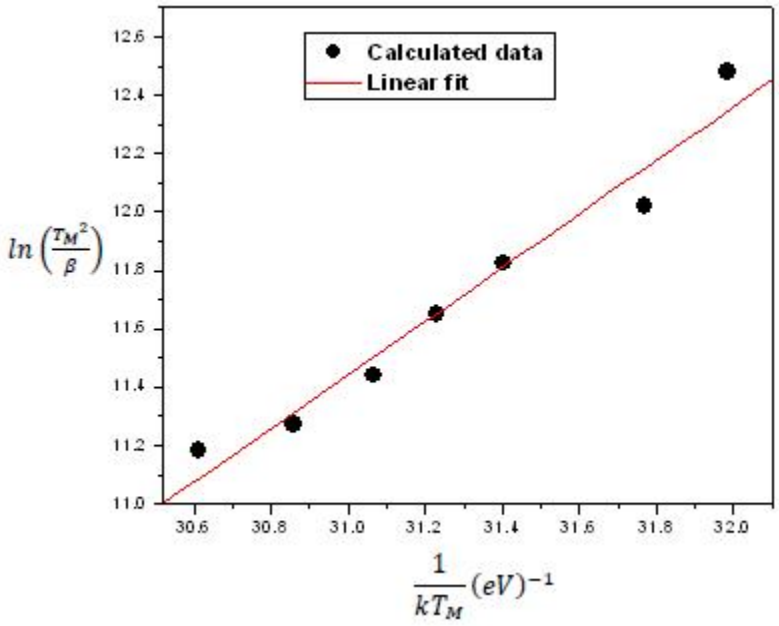

Fig. 6.6: Graph of calculation of $\ln\left(\frac{T_M^2}{\beta}\right)$ versus $\frac{1}{kT_M}$ as indicated by the dots. The line through the dots is the linear fit. The trap depth E is determined from the slop of this line and the frequency factor s is evaluated from the value of the intercept on $\ln\left(\frac{T_M^2}{\beta}\right)$ axis.

Change in the linear heating rate β results in the change of the temperature T_M of the maximum TL intensity of the peak: faster heating rates produce a shift in temperature relatively towards higher values of T_M as explained above. When $\ln\left(\frac{T_M^2}{\beta}\right)$ is plotted against $\frac{1}{kT_M}$, the resulting graph consists of a straight line of slope E and intercept (on $ln\left(\frac{T_M^2}{\beta}\right)$ axis) $ln\left(\frac{E}{Sk}\right)$. The value of the frequency factor s was determined from the value of this intercept. From the slope and intercept of the graph $\ln\left(\frac{T_M^2}{\beta}\right)$ and $\frac{1}{kT_M}$ in Figure 6.6, the kinetic parameters E and s were calculated. From the slope of the graph, $E = 0.918$ eV and from the value of the intercept $= \ln\left(\frac{E}{Sk}\right)$, $s = 2.65 \times 10^{11}\ s^{-1}$. This method is a very powerful and frequently used technique for determination of the TL kinetic parameters.

6.4 Photoluminescence study

Figure 6.7 shows the photoluminescence excitation and emission spectra of $KY_3F_{10}:Ho^{3+}$ phosphor powder. Green emission at about 540 nm was investigated at four main excitation wavelengths; namely, 362, 416, 454 and 486 nm. The highest PL intensity occurred at excitation of 454 nm. In addition, faint red (near infrared) emission was observed at 750 nm for all the excitations.

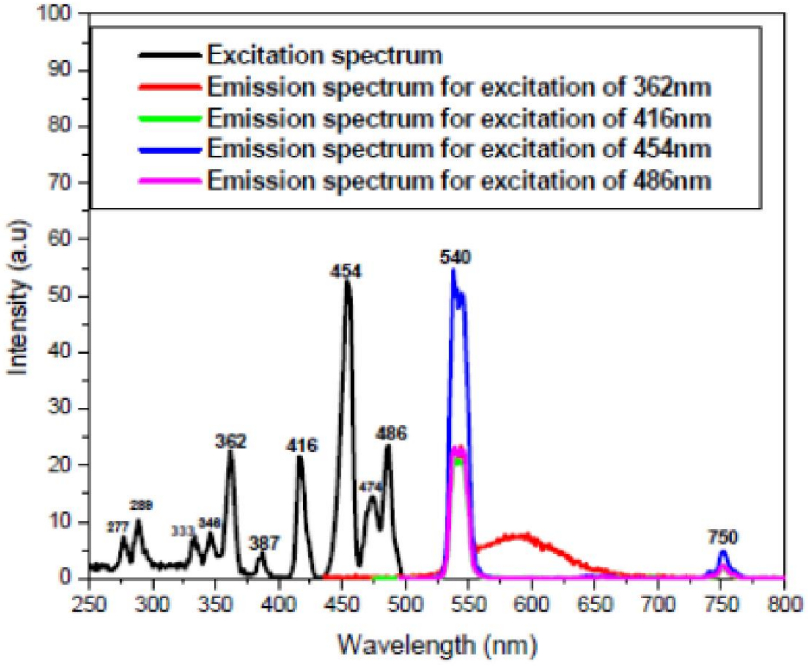

Fig. 6.7: PL excitation and emission spectra of $KY_3F_{10}:Ho^{3+}$ phosphor powder. Two major emission wavelengths (540 and 750 nm) are determined at four major excitation wavelengths as indicated. In addition, there is one broad emission centered about 600 nm (as shown for excitation of 362 nm).

As shown in Figure 8, we account the green emission at 540 nm to the $^5F_4$–$^5I_8$ and $^5S_2$–$^5I_8$ transitions and the faint red emission at 750 nm is due to the $^5F_4$ –$^5I_7$ and $^5S_2$–$^5I_7$ transitions. Such multiple emissions from other holmium doped phosphor are also reported in literature [31]. In addition to the emissions mentioned above, emission at 660 nm due to the $^5F_5$–$^5I_8$ transition of Ho^{3+} is reported in literature, for example, by Secu et al [32]. However, this emission is not observed in our case and the reason is not known. The broad emission centered around 600 nm (photon energy of ~2.1eV) for excitation of 362 nm is particularly interesting. This luminescence, appearing as a broad spectral peak, partly lies in the yellow and orange regions. This PL emission can not be from Ho^{3+} and its origin is not known.

The PL decay life time of the sample at excitation (λ_{ex}) of 454 nm and emission (λ_{em}) of 540 nm is given in Fig. 6.9. It is of the order of few milliseconds and hence it could be useful for scintillation. Scintillators with average life time up to few hundreds of ms have been reported by C. Cuesta et al [33]. The average PL life time measured in our case is 10.7 ms and is significantly larger as compared to that of other rare earth doped (Pr^{3+} for example) KY_3F_{10} which is of the order of few nano-seconds [3].

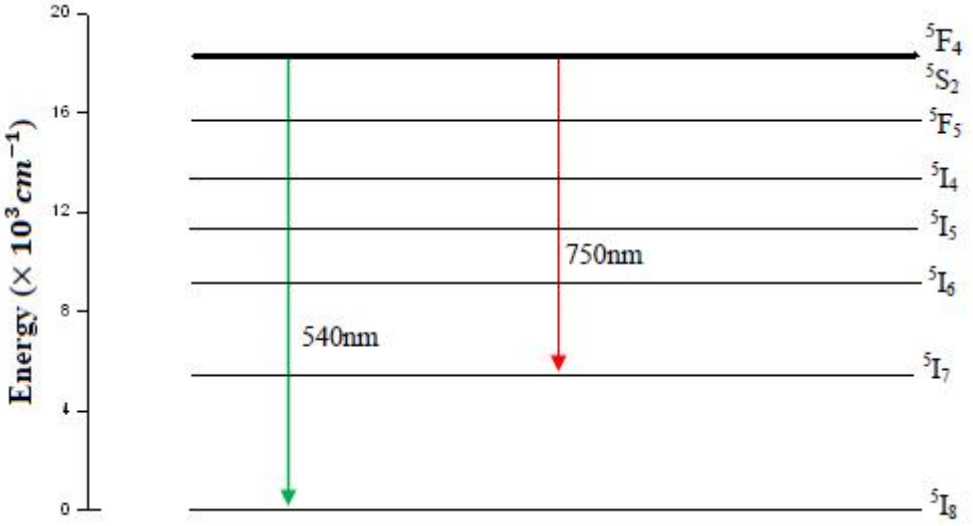

Fig. 6.8: Energy level diagram of Ho^{3+}. The observed transitions are indicated by arrows.

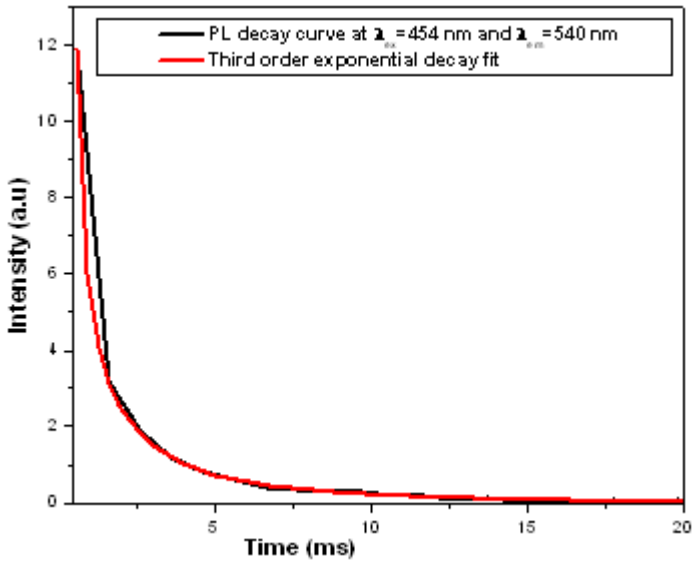

Fig. 6.9: The photoluminescence decay curve of KY_3F_{10}: Ho^{3+} phosphor powder.

Conclusion

In conclusion, the TL, PL, structure and morphology of $KY_3F_{10}:Ho^{3+}$ phosphor powder were studied. The TL intensity increases with increase in the UV exposure time up to 20 minutes and then decreases. The glow curves slightly shift to higher temperature region for relatively higher heating rate, but with reduced intensity peak and this behavior is not attributed to thermal quenching effect in this particular study. Important TL kinetic parameters; namely the activation energy (E) and the frequency factor (s) are calculated using variable heating rate method. The glow peaks obey first order kinetics. PL analysis shows that the green emission at 540 nm is ascribed to the $^5F_4$–$^5I_8$ and $^5S_2$–$^5I_8$ transitions and the faint red emission at 750 nm is due to the $^5F_4$ –$^5I_7$ and $^5S_2$–$^5I_7$ transitions. In addition to the sharp green emission at 540 nm, a broad emission centered at 600 nm was observed for excitation wavelength of 362 nm its origin is not known. The photoluminescence life time of the phosphor is of the order of few milliseconds and hence it could be useful for scintillation.

References

[1] K. Jin Kim, et al., J. Cryst. Growth 299, 171 (2007).

[2] M. Mujaji, Jon-Paul R. Wells, J. Phys.: Condens. Matter 21, 1 (2009).

[3] T. Yanagida, Y. Fujimoto, K. Fukuda, Jpn. J. Appl. Phys 53, 1 (2014).

[4] A. Rapaport, J. Milliez, F. Szipocs, M. Bass, A. Cassanho, H. Jenssen, Appl. Opt. 43, 6477 (2004).

[5] Z. Jin-Su, Z. Hai-Yang, S. Jan-Shi, C. Li-Hong, L. Xiang-Ping, C. Bao-Jiu, Chin. Phys. Lett. 29, (2012).

[6] F. Cheng et al., Chin. Phys. Lett. 28 (2011).

[7] P. Porcher, P. Carlo, J. Chem. Phys. 68, 4183 (1978).

[8] A. Braud, S. Girard, J. L. Doualan, M. Thuau, R. Moncorge, A. M. Tkachuk, Phys. Rev. B 61, 5280(2000).

[9] J. Zhang et al., J. Appl. Phys, 106, 34915 (2009).

[10] S. Veronesi, D. Parisi, F. Marchetti, M. Tonelli, J. Phys. Chem. Solids, 71, 913 (2010).

[11] A. Rapaport, J. Milliez, F. Szipocs, M. Bass, A. Cassanho, H. Jenssen, Appl. Opt. 43, 6477 (2004).

[12] C. Andraud, J. Denis, B. Blanzat, A. Vedrine, Chem. Phys. Lett. 101, 357 (1983).

[13] G. Boulon, J. Gacon, D. Trottier, A. Vedrine, Phys. Status Solidi B 93, 775 (1979).

[14] J. Zhang, Z. Hai-Yang, S. Sun-Shi, C. Li-Hong, L. Xiang-Ping, C. Bao-Jiu, Chinese Phys. Lett. 29, (2012).

[15] M. Diaf et al, Can. J. Phys. 77, 693 (1999).

[16] Y. Kalisky, The Physics and Engineering of Solid State Lasers, 2006.

[17] R. Tamrakar, D. P. Bisen, I. P. Sahu, N. Brahme, J. Radiat. Res. Appl. Sci. 7, 437 (2014).

[18] R. Chen, D. Lo, J. L. Lawless, Radiat. Prot. Dosim. 119, 33 (2006).

[19] Y. Parganiha, J. Kaur, V. Dubey, D. Chandrakar, Superlattice Microst. 77, (2015).

[20] N. Tiwari, R. Kuraria, R. Tamrakar, J. Radiat. Res. Appl. Sci. 7, 542 (2014).

[21] A. Charlesby, R. H. Partridge, Proc. Roy. Soc. A 271, 170 (1963).

[22] V. Jain, S. P. Kathuria, A. K. Ganguly, J. Phys. C Solid State 8, 2191(1975).

[23]L. Jiang, Y.L. Zhang, C.Y. Li, J.Q. Haq, Q. Su, J. Lumin. 128, 1904 (2008).

[24] M. Akselrod, V.S. Kortov, D.J. Kravetsky, V.I. Gotlib, Radiat. Prot. Dosim. 33, 119 (1990).

[25] M. Akselrod, N.A. Larsen, V. Whitley, S.W.S. McKeever, J. Appl. Phys. 84, 3364 (1998).

[26] M. Akselrod, V.S. Kortov, D.J. Kravetsky, V.I. Gotlib, Radiat. Prot. Dosim. 32, 15 (1990).

[27] M. Kumar, G. Chourasiya, B. C. Bhatt, C.M. Sunta, J. Lumin. 130, 1216 (2010).

[28] M. Kumar, G. Chourasiya, Meas. Sci. Technol. 20, (2009).

[29] S. Deshpande, S. Dhoble, W. Pokale, B. Deshmukh, R. Pode, T. Gundurao, Nucl. Instrum. Meth. B 134, 385 (1998).

[30] S.W.S. McKeever, Thermoluminescence of solids, Cambridge Solid State Science Series, Oklahoma State University, 1988.

[31] A. Pandey and V. K. Rai, Dalton Trans. 42, 11005 (2013).

[32] M. Secu, M. Cernea, B. Vasile, J. Nanopart. Res. 13, 3123 (2011).

[33] C. Cuesta, Opt. Mater. 36, 316 (2013).

Chapter 7

The effect of argon gas pressure on structural, morphological and photoluminescence properties of pulsed laser deposited $KY_3F_{10}:Ho^{3+}$ thin films

7.1. Introduction

Display market is one of the fastest growing segments of the electronics industry and investment on this market was valued at USD 114 billion in 2014, and is expected to reach USD 157 billion by 2020 [1]. Several breakthroughs have been made in this technology in the past couple of decades [2]. In the future, there is a big trend of relying on high resolution display devices for the production of high technology materials. The growth in the popularity of such devices is mainly due to the improvements in their quality, affordability and versatility in applications [1]. Moreover, the development of high resolution display devices such as cathode-ray tubes (CRTs), electroluminescent devices, plasma display panels, and field emission displays (FEDs) requires highly efficient luminescent phosphor materials such as thin film phosphors. The unique advantage of displays based on thin film phosphors is that they are characterized by high contrast and resolution, good thermal conductivity as well as a high degree of uniformity and better adhesion [3–6].

Fluoride materials are promising candidates for such display devices due to their low phonon energies [7]. This reduces the non-radiative quenching phenomena so that high luminescence efficiency can be obtained; which is required for any display devices [7]. Potassium triyittrium decafluoride (KY_3F_{10}) is very attractive material because of many reasons: Firstly, it is easy to be synthesized (for example, by using Czochralski pulling technique in laboratory) and secondly, it possesses good optical, thermal and mechanical properties which are comparable to other fluoride materials such as $LiYF_4$ [7-9]. It also melts congruently and suitable for doping with rare earth ions. Moreover, it is isotropic crystal and this facilitates its spectroscopic characteristics [9]. In addition to all the aforementioned interesting properties, the much higher energy transfer efficiency in it than other fluorides such as BaY_2F_8 and $LiYF_4$ makes it an interesting material for further study in luminescence applications [10]. On top of the exciting properties of this host material, doping with holmium has significant advantage over other rare

earth ions because of its high-gain cross section and long life time of $^5I_7$ upper level emission resulting in high energy storage capability and efficiency [11].

Thin films of $KY_3F_{10}:Ho^{3+}$ phosphor can be prepared using one of the thin film deposition techniques called pulsed laser deposition (PLD). PLD is a well-known and versatile technique for the growth of thin films. Using this technique, thin films can be grown over a wide temperature range and under the presence of different background gases. The temperature and the background gas play two important roles in the growth of thin films during PLD [12-15]. Firstly, they are critical parameters that determine the final step of the film formation. Secondly, they determine the amorphous or the crystalline nature of the deposited films. The study on the influence of substrate temperature on structure, morphology and photoluminescence intensity of $KY_3F_{10}:Ho^{3+}$ is carried out elsewhere. However, the effect of pressure on the properties of its thin films is not investigated to the best of our knowledge.

Therefore, in this study, we report the influence of gas pressure on the structural, morphological and photoluminescence properties of $KY_3F_{10}:Ho^{3+}$ thin film phosphor prepared by PLD at various argon gas pressures: 0.5Torr, 1Torr and 1.7 Torr while keeping all other parameters constant. The aim of this study is to identify optimal argon gas pressure that will result in better structure, morphology and high luminescence intensity for potential applications in future display devices.

7.2 Experimental details

The experiment was performed by using Nd-YAG laser (266 nm, pulse duration of 9.3 ns, repetition rate of 10 Hz) on (100) silicon substrate. The laser fluence was kept at $1.2\ J/cm^2$. The vacuum chamber was then pumped to a base pressure of 5.6×10^{-5} mbar before introducing argon. Different argon gas pressures (0.5 Torr, 1 Torr and 1.7 Torr) were used in the experiment. The temperature, the laser energy and the target-to-substrate distance, respectively were 500^oC, 40 mJ and 5.2 cm. The target was made from commercial $KY_3F_{10}:Ho^{3+}$ powder pressed at 6 MPa. The crystal structure of the films was analyzed by X-ray diffraction (XRD) using Bruker D8 advance X-ray diffractometer operating at 40 kV and 40 mA using Cu kα = 0.15406 nm. The morphology was studied using Field Emission Scanning Electron Microscope (FE-SEM) and Atomic Force Microscope (AFM) with scanAsyst in tapping mode. The elemental composition and ratios of the films were investigated using Energy Dispersive X-ray Spectrometer (EDS) and X-ray Photoelectron spectroscopy (XPS). The photoluminescence excitation and emission spectra were measured at room temperature using Cary Eclipse fluorescence spectrometer model: LS-55 with a built-in xenon flash lamp.

7.3 Results and discussion

7.3.1 Structural and morphological properties

The deposition pressure strongly affects the degree of crystallinity of films. The XRD spectra of $KY_3F_{10}:Ho^{3+}$ thin films deposited at 500 ^oC at different argon gas pressures is shown in Figure 7.1. The miller indices of the prominent peaks are shown. The films crystallized in tetragonal polycrystalline phase of KY_3F_{10} (in agreement with JCPDS card No 27-0465). The diffraction peaks observed at 2θ values of 26.61, 28.06, 40.55, 44.29 and 52.58^o are relatively intense for the film deposited at a pressure of 1 Torr as compared to that of the films deposited at pressures of 0.5 and 1.7 Torr. The pressure dependence of the crystalline quality of the films is checked from pressure dependence of the FWHM illustrated in Figure 7.2 using the dominant (113) diffraction peak. The full-width half-maximum (FWHM) of this peak is 0.15247, 0.10780 and 0.13384^o for the films deposited at pressures of 0.5, 1 and 1.7 Torr respectively. The value of the FWHM is minimum for the film deposited at pressure of 1 Torr.

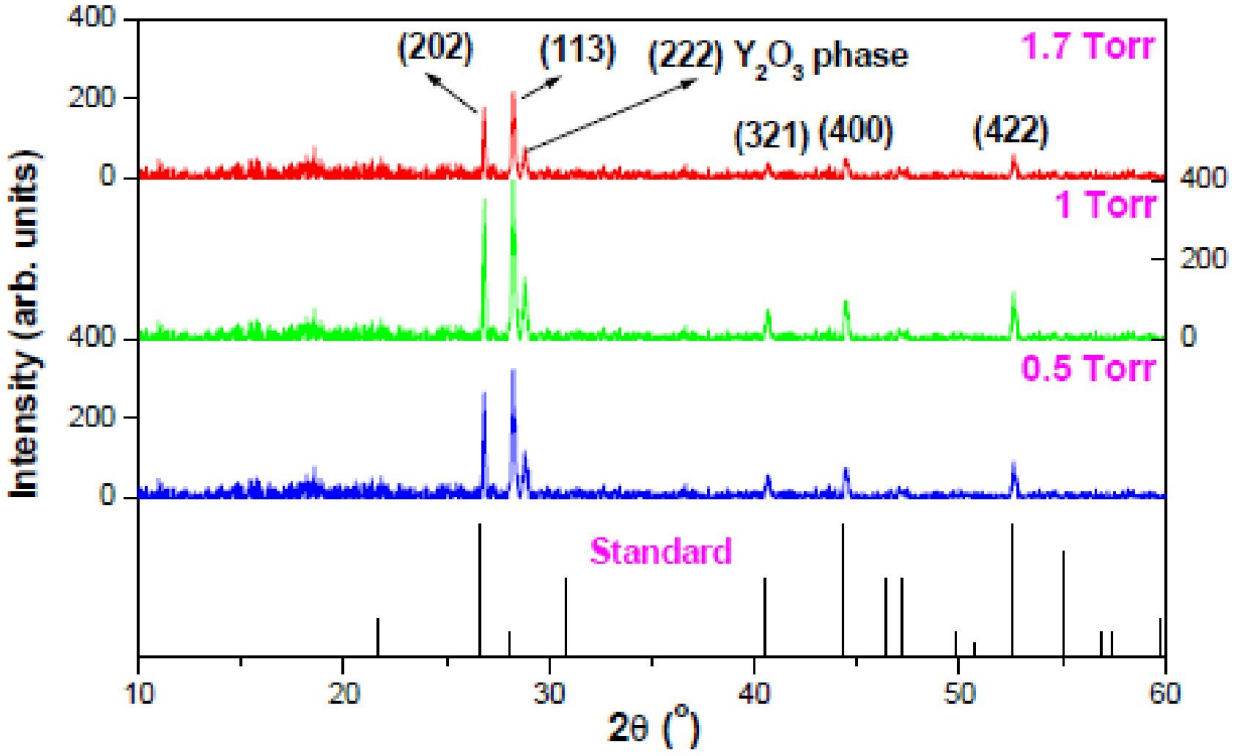

Fig. 7.1: XRD pattern of $KY_3F_{10}:Ho^{3+}$ thin films deposited under various pressures.

This shows that the crystalline quality of the film is improved at argon gas pressure of 1 Torr at the fixed substrate temperature of 500^{o}C. There was no observed shift in diffraction peaks of the films following change in argon gas pressure.

The average crystallite size has been computed from the full width half maximum (FWHM) of the most intense peaks using equation (5.2).

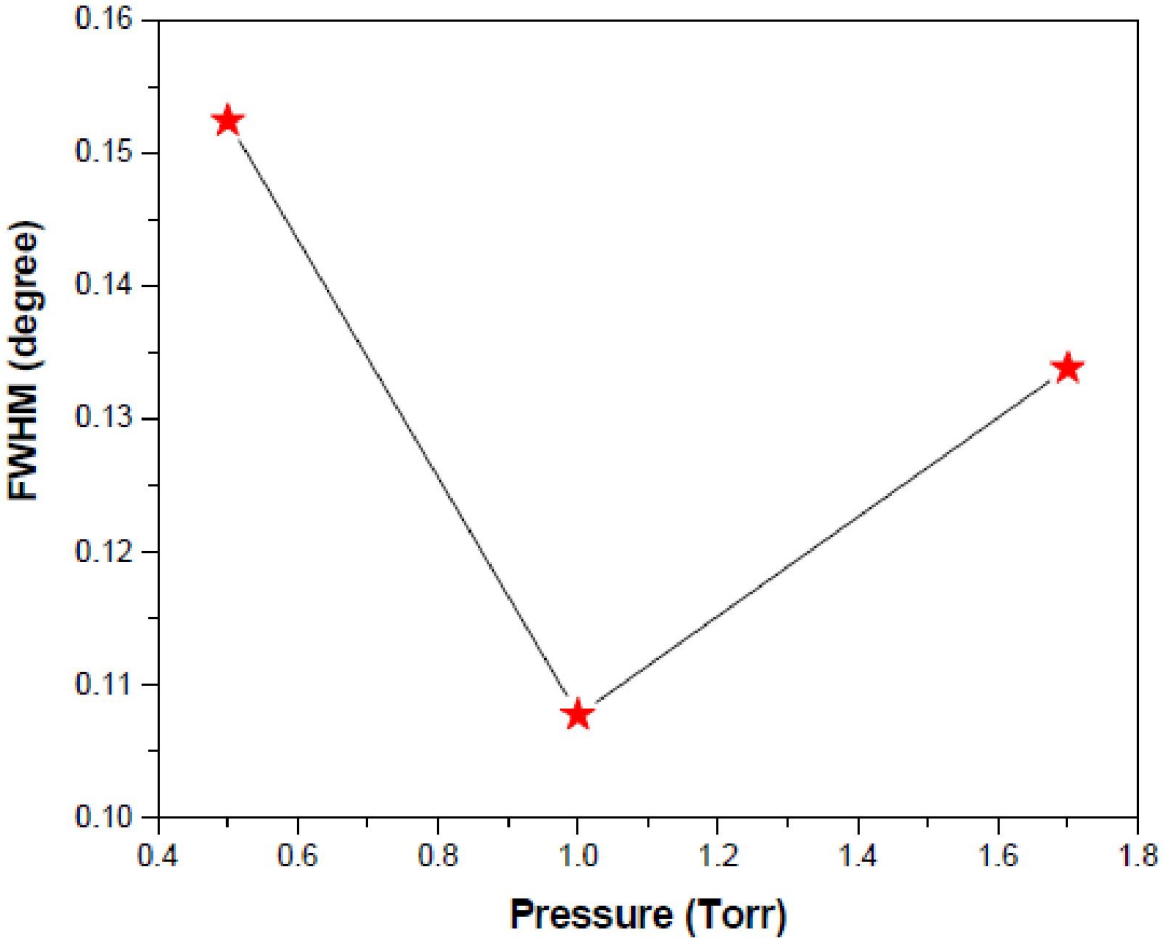

Fig. 7.2: The pressure dependence of the FWHM of the dominant (113) peak.

The crystallite size of the deposited films varied between 53.7-57.3 nm. Figure 7.3 shows the FE-SEM images of the as-prepared thin films at argon gas pressures of 0.5, 1 and 1.7 Torr. It can be seen from the figures that the sample deposited at 0.5 Torr is relatively flat (smooth) and less agglomerate. When the background pressure was increased to 1 and 1.7 Torr, an increase in surface roughness and agglomeration was observed; the roughest and most agglomerate surface being obtained at 1.7 Torr. Such increase in surface roughness at higher background gas pressures is also reported in literature [17-19]. The increase in surface roughness of the films at higher deposition pressure was further confirmed by the AFM results (not shown here). The RMS roughness over a 1 μm × 1 μm standard region increases as the deposition pressure rises from 0.5 Torr to 1.7 Torr.

The deposition pressure has also an influence on film stiochiometry. P. Orgiani et al reported that the background gas pressure plays significant role in determining the transport properties and chemical composition of thin films prepared by PLD [20]. According to P. Orgiani et al the increase in pressure might selectively affect both the energy and the efficiency of the single species transfer to the growing film. Similar results of selective species transfer under a certain deposition conditions were reported by J. Gonzalo et al [12] and hence thin film stoichiometry congruent to the target may not be obtained under some conditions.

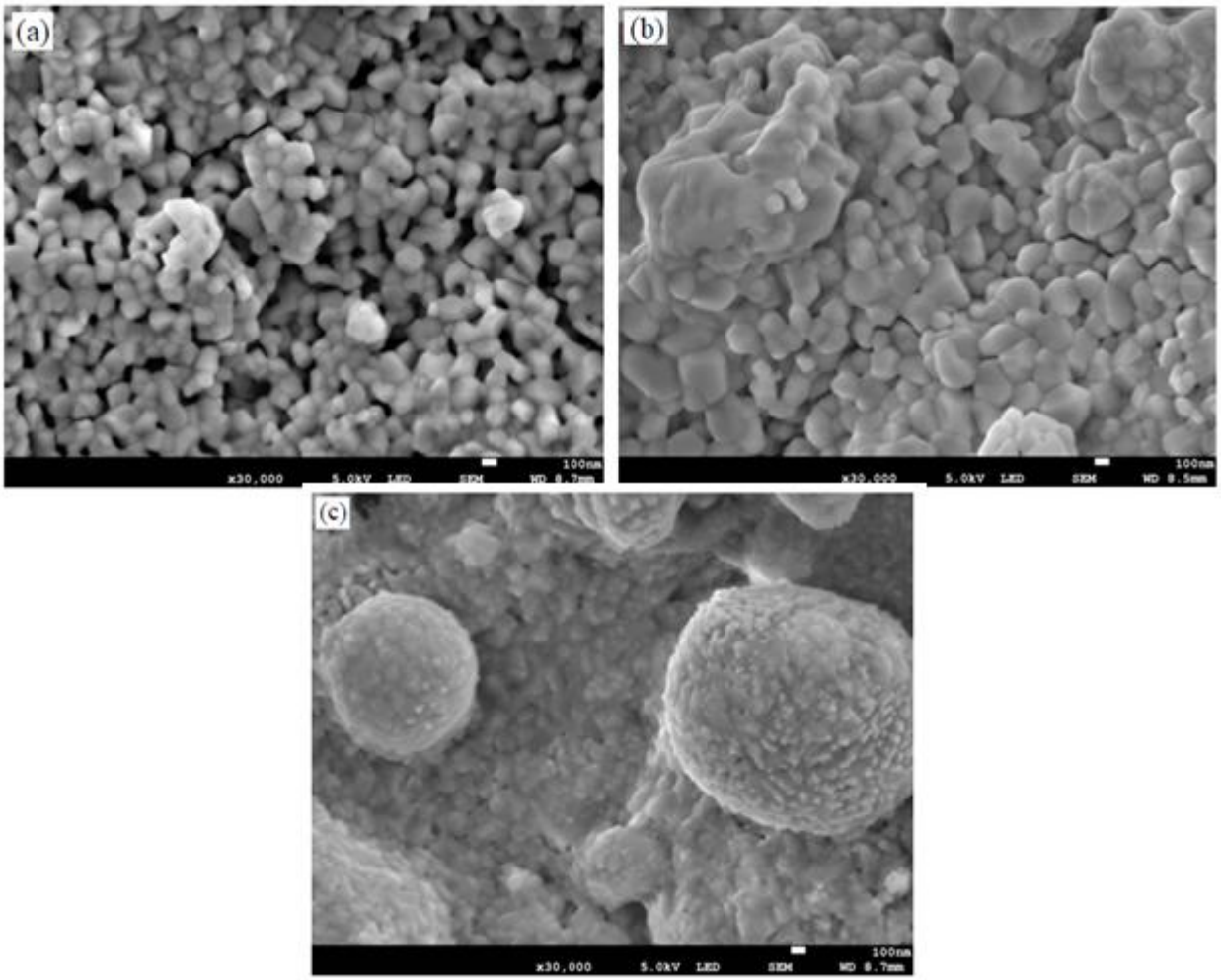

Fig. 7.3: FE-SEM images of the films deposited at (a) 0.5Torr, (b) 1Torr, (c) 1.7Torr.

Figure 7.4 shows the XPS spectrum of the film deposited at pressure of 1.7 Torr. The K:Y:F elemental ratios obtained from XPS analysis are 0.9:3.68:8.74, 0.52:3.83:7.5, 0.38:3.51:6.2 at pressures of 0.5, 1 and 1.7 Torr respectively. All the results show Y-excess and lack of K and F in the chemical

composition of the deposited films. It is worth noting that the Y-excess is not a monotonic function of the deposition pressure and is maximum at a pressure of 1 Torr. The ratios show deviation from the target composition of 1:3:10. Therefore, the stoichiometry of the target was not attained for all the deposition pressures.

It was observed that the ratios Y:K and Y:F were influenced by change in argon partial pressure. According to P. Orgiani et al, the ratio between light and heavy elements is dramatically influenced by background pressure [20] and our results are in good agreement with this report. Figures 7.5 and 7.6 show, respectively the EDS spectra and elemental mapping of the films investigated. The EDS spectra show the presence of all the elements except Ho. The absence of Ho in the EDS and XPS spectra shows that concentration of Ho must be very low.

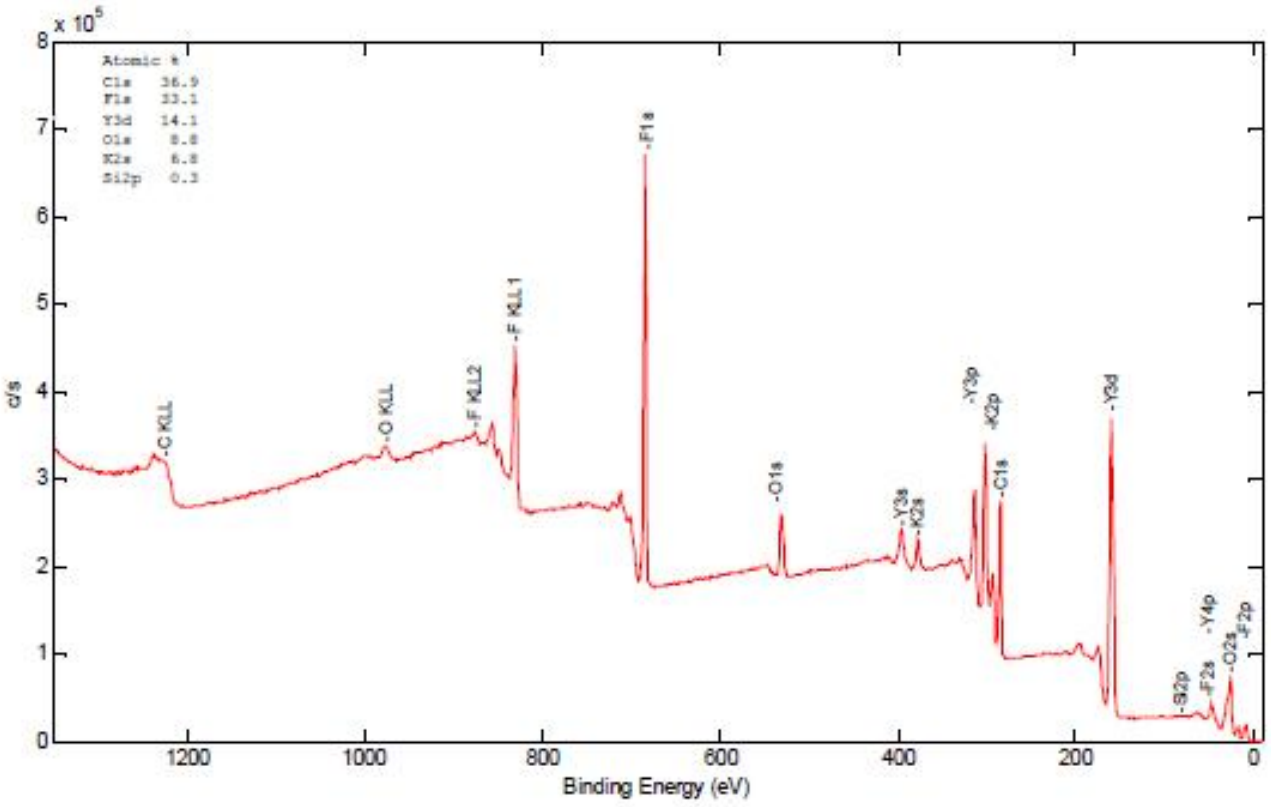

Fig. 7.4: XPS spectrum of the film deposited at pressure of 1.7 Torr.

The fact that all the deposited films show lack of K and F can be explained in terms of two factors. The first factor is the decrease in their deposition rate due to deceleration and off-target scattering by the background gas molecules [12, 21]. The second factor is that K has low sticking coefficient [22] and F is more volatile than K and Y. As a result some re-sputtering of K and re-evaporation of F from the

substrate might have occurred. Therefore, the fact that stoichiometric transfer of target composition can be achieved for most materials does not insure that all the elements get incorporated in to the growing film at the same rate [22].

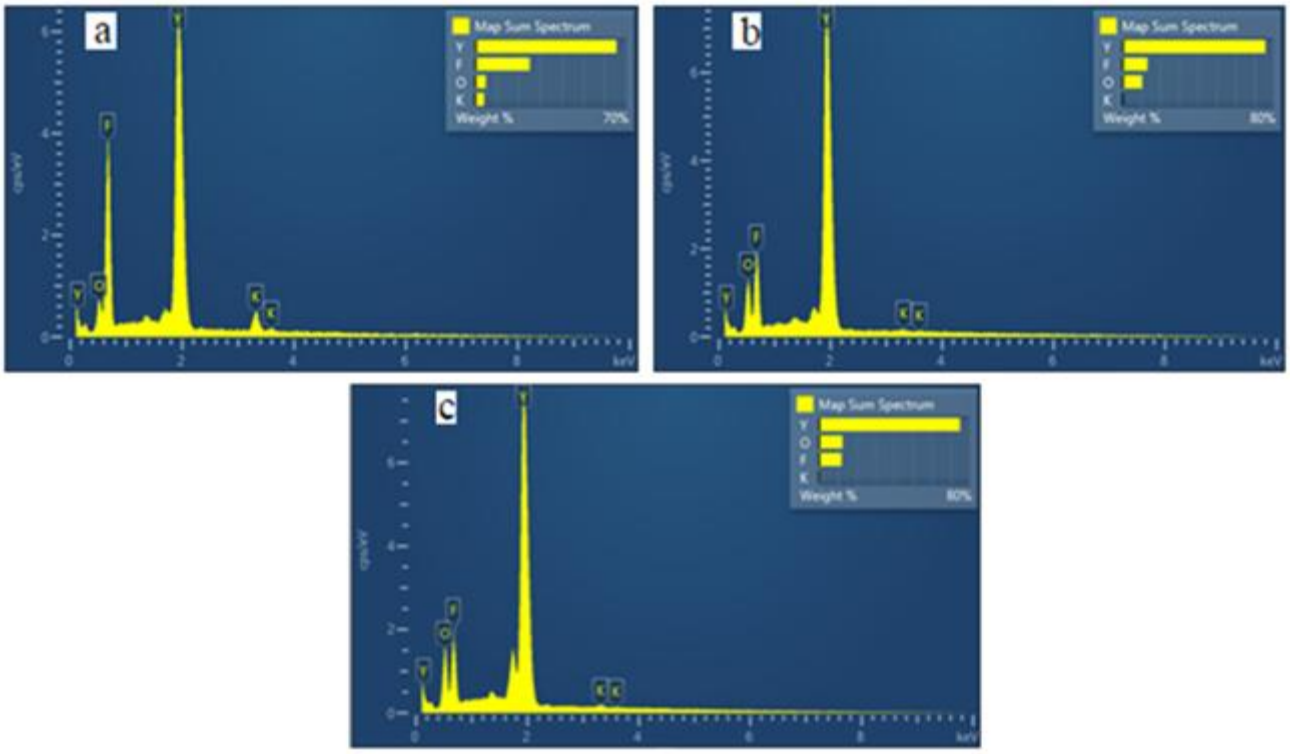

Fig. 7.5: EDS spectra of the films deposited at (a) 0.5Torr, (b) 1Torr, (c) 1.7Torr.

J. Gonzalo et al. reported that if the background gas pressure is high, some of the plasma species may loss their kinetic energy before reaching the surface of the substrate which in turn decreases the deposition rate [12, 21]. In this case, the deposition condition depends on the masses of the individual species [12]. In other words, the mass of Y is approximately twice of the mass of Ar and Y doesn't seem to be much affected by the scattering due to Ar molecules. This means that the relative amount of the heavier species (Y in this case) that travel along the normal to the substrate will be higher than that of the lighter species at relatively higher pressures. This could be one cause for the observed Y-excess in the films. The other reason for the observed Y-excess could be the fact that Y is less volatile than K and F.

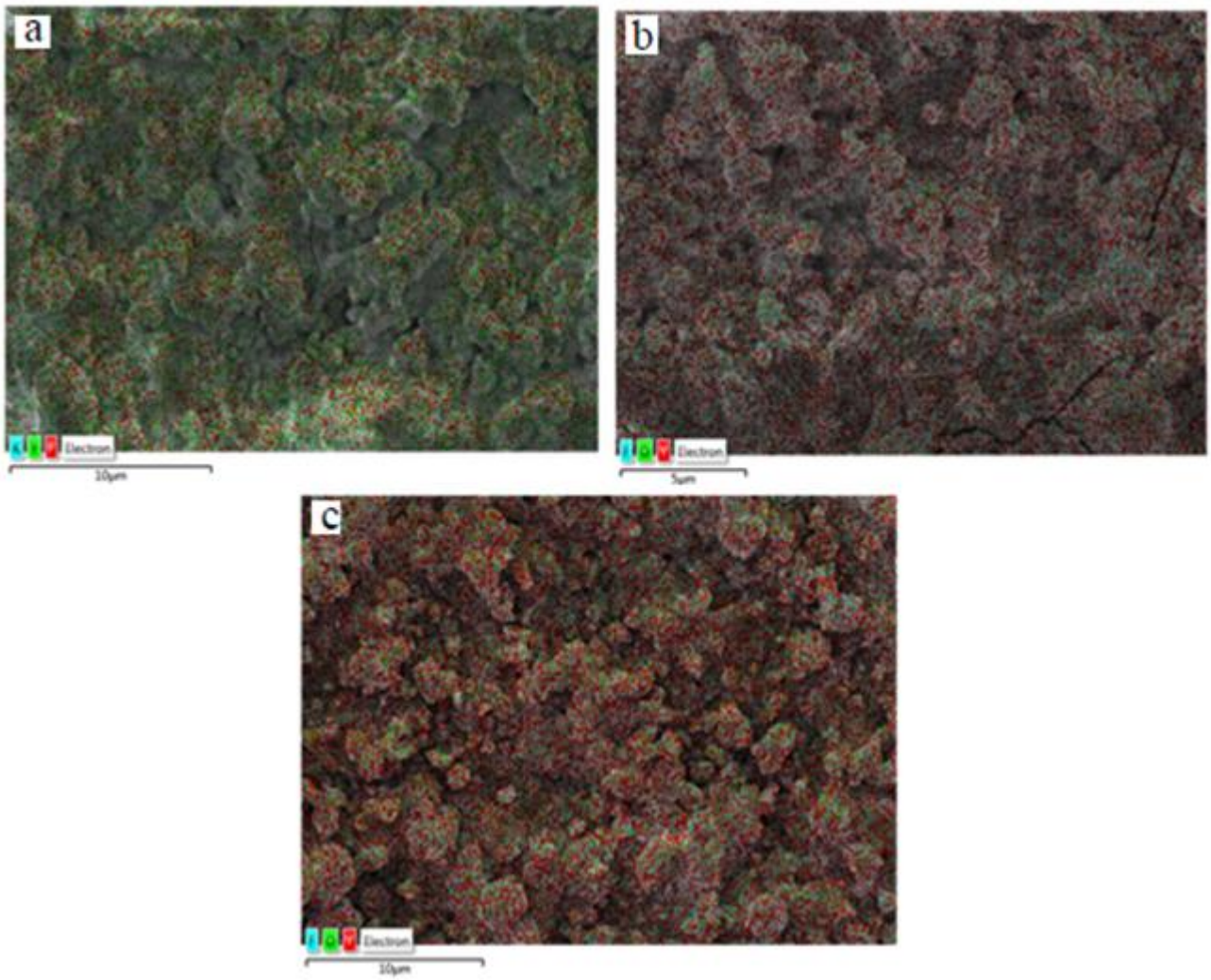

Fig. 7.6: EDS elemental mapping of the films deposited at (a) 0.5 Torr, (b) 1 Torr and (c) 1.7 Torr.

7.3.2 Photoluminescence properties

Figure 7.7 shows the normalized PL excitation and emission spectra of $KY_3F_{10}:Ho^{3+}$ phosphor thin film deposited at pressures of 1.7 Torr. Green emission at 540 nm was probed using three main excitation wavelengths; namely, 362, 416 and 454 nm. In addition, faint red (near infrared) emission was observed at 750 nm for all the excitations. The highest PL intensity occurred at excitation of 454 nm. The green emission at 540 nm is ascribed to the $^5F_4$–$^5I_8$ and $^5S_2$–$^5I_8$ transitions and the faint red emission at 750 nm is due to the $^5F_4$ –$^5I_7$ and $^5S_2$–$^5I_7$ transitions of Ho^{3+}. Similar results were obtained for the films deposited at 0.5 and 1 Torr. Such multiple emissions from other holmium doped phosphor are also

reported in literature [23-24]. Figure 7.8 shows the PL emission spectra of the films deposited at 0.5, 1 and

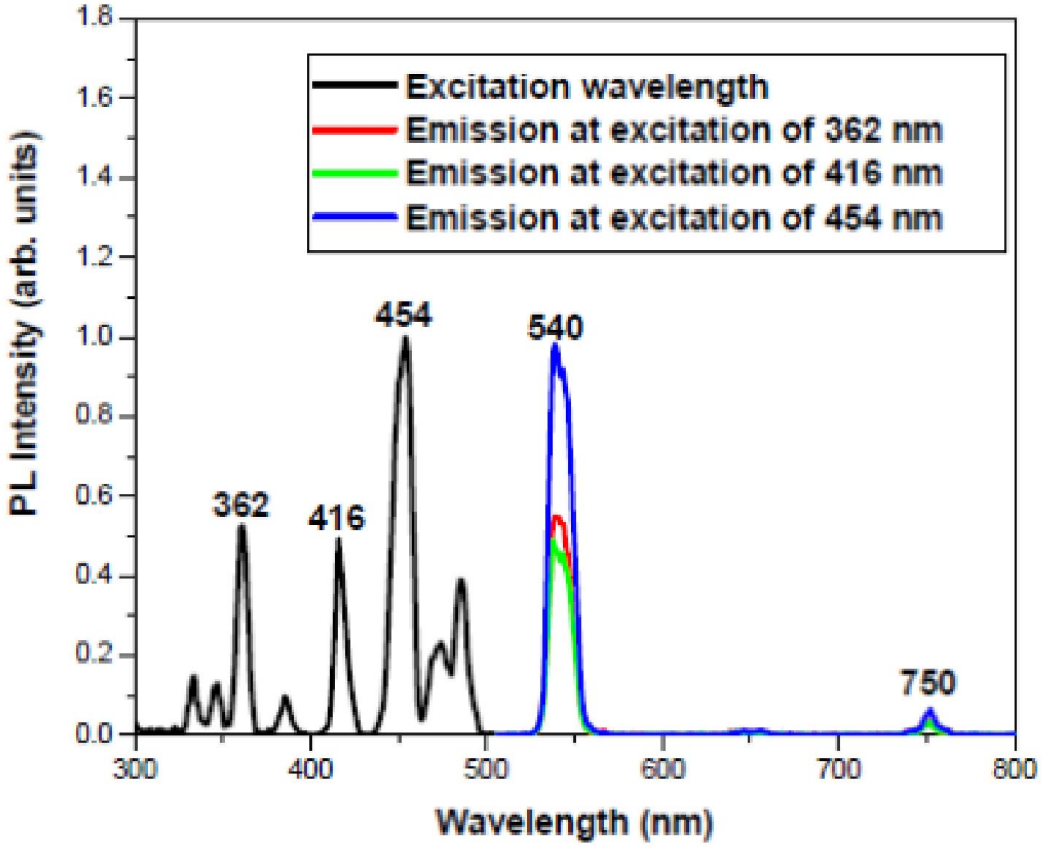

Fig. 7.7: Normalized PL excitation and emission spectra of $KY_3F_{10}:Ho^{3+}$ thin film prepared at 1.7 Torr.

1.7 Torr at excitation of 454 nm. It can be observed that enhancement in the intensity of the PL was observed with increasing the background gas pressure from 0.5 Torr to 1 and 1.7 Torr. Improvement in PL intensity was observed for all the films at excitations of 362 and 416 nm with increase in deposition pressure. In this study, the improved luminescence intensity at higher gas pressures is attributed to the increment in the surface roughness at such higher pressures. Surface roughness has been observed in various studies to increase with increase in background gas pressure during pulsed laser deposition of films. The rough surface reduces the total internal reflection thereby enhancing luminescence intensity [17-19]. Enhancement in luminescence of thin films due to enhanced surface roughness at higher background gas pressures was reported in literature [17-19].

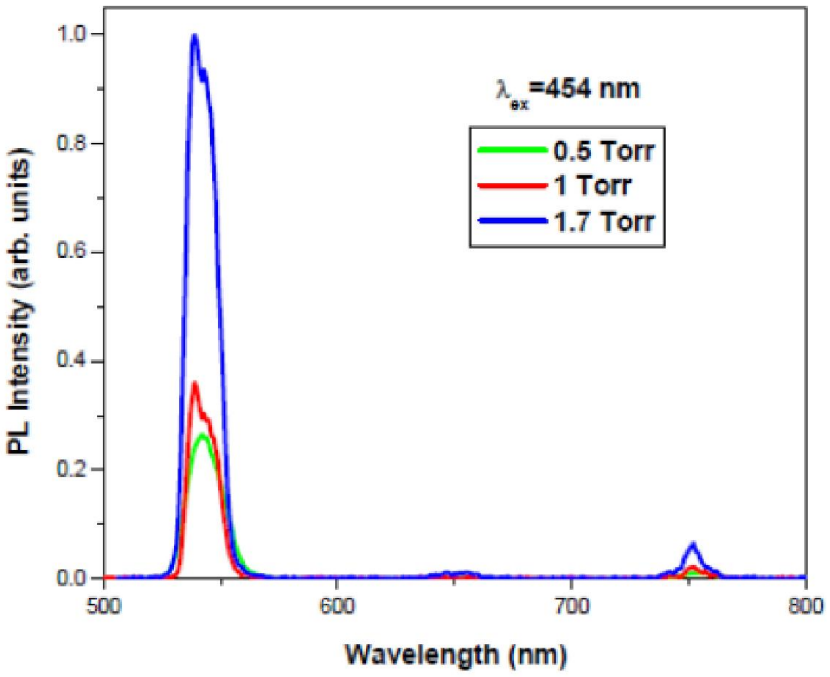

Fig. 7.8: Normalized PL emission spectra of KY_3F_{10}: Ho^{3+} thin films prepared at 0.5, 1 and 1.7 Torr.

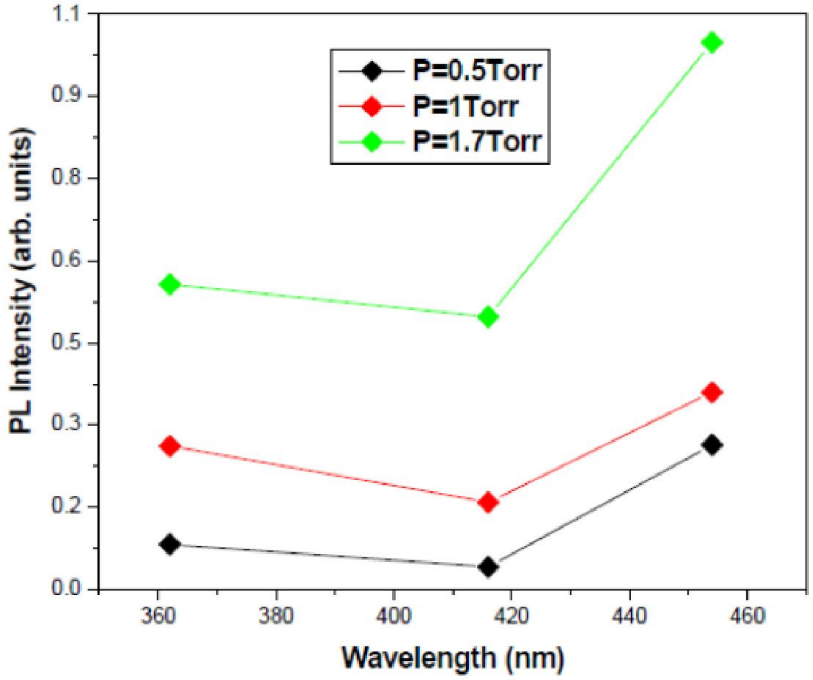

Fig. 7.9: Variation of emission peaks with pressure for excitation wavelengths of 362, 416 and 454 nm.

The PL intensity is directly proportional to the population of electrons involved in a given transition. Variation of the emission peaks maxima with pressure is shown in Figure 7.9 for excitation wavelengths of 362, 416 and 454 nm. It is clearly seen that higher emission peaks were observed at higher

background gas pressures for all excitation wavelengths. The variation of the dominant emission peak at 540 nm against pressure is also shown in Figure 7.10 for excitation of 454 nm.

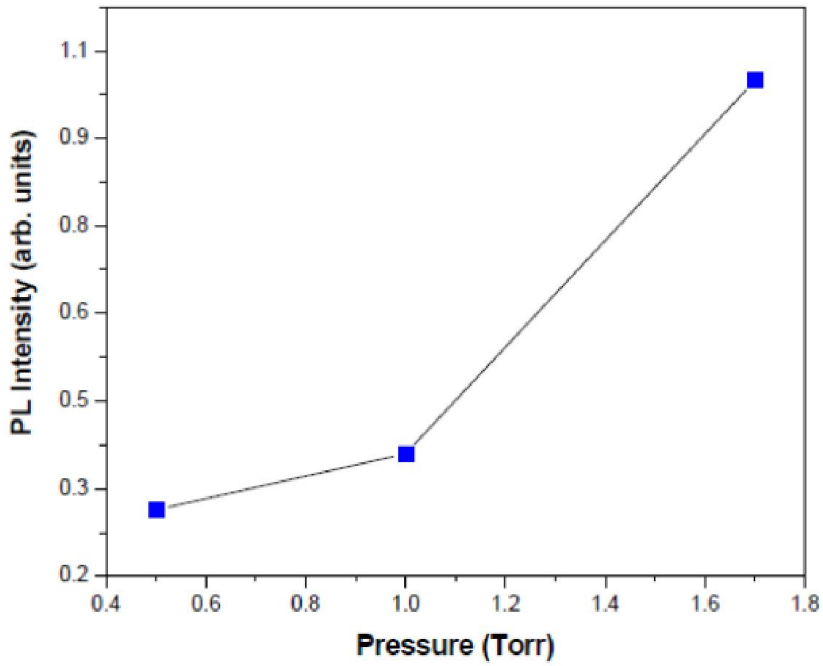

Fig. 7.10: Variation of the most intense emission peak with pressure for excitation wavelengths of 454 nm.

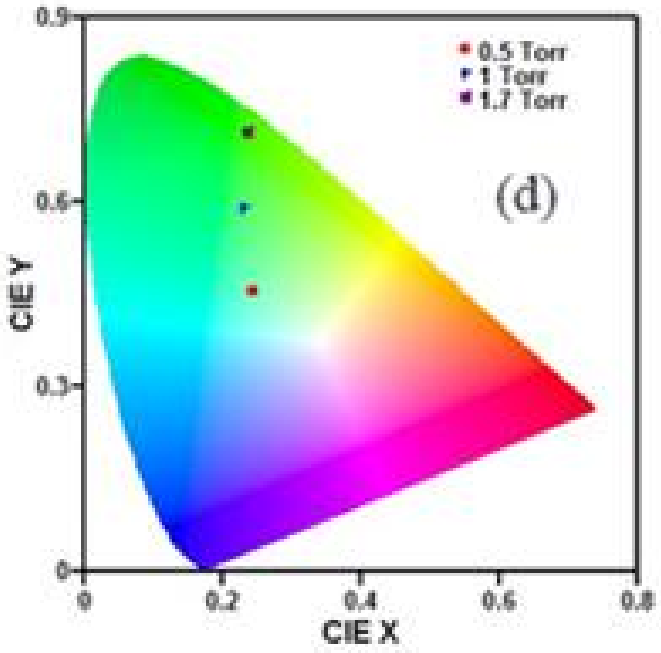

Fig. 7.11: The value of the chromaticity coordinates of $KY_3F_{10}:Ho^{3+}$ thin films.

The values of the chromaticity coordinates of $KY_3F_{10}:Ho^{3+}$ thin films have been estimated from the 1931 Commission Internationale de l'Eclairage (CIE) system using the excitation wavelength of 454 nm (Figure 7.11). This system helps us visualize the variation in color emitted from samples and the coordinates are measured as (x,y). Though the values are found in green region for all the thin films, relatively intense green emission was observed from those deposited under relatively higher background gas pressure. The energy level diagram of Ho^{3+} in KY_3F_{10} with the observed transitions is also shown in Figure 7.12.

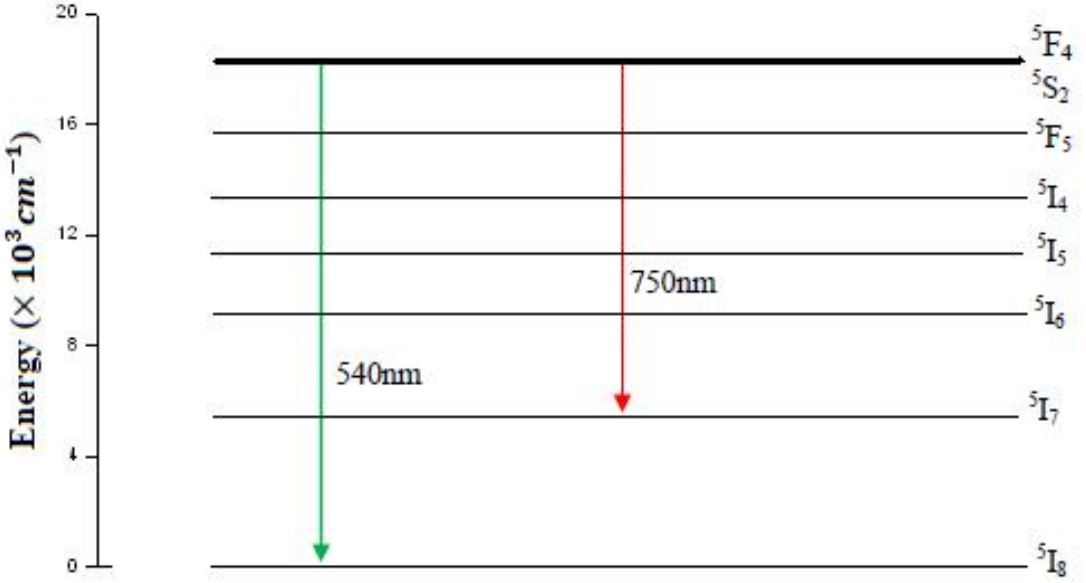

Fig. 7.12: Energy level diagram of Ho^{3+} in KY_3F_{10}. The observed transitions are indicated by arrows.

Conclusion

The influence of argon gas pressure on the structural, morphological and PL properties of commercially obtained $KY_3F_{10}:Ho^{3+}$ phosphor powder thin films were investigated. The crystallite size of the deposited films varied between 53.7-57.3 nm. It is observed that surface roughness of the deposited films increase with an increase in background argon gas pressure. All the deposited films show Y-excess. The photoluminescence emission peaks of the films increases with increasing the deposition pressure and this is attributed to the increase in surface roughness at such higher deposition pressures. Green PL emission at 540 nm was investigated at three main excitation wavelengths; namely, 362, 416 and 454 nm. The green emission at 540 nm is ascribed to the $^5F_4$–$^5I_8$ and $^5S_2$–$^5I_8$ transitions and the faint red emission at 750 nm is due to the $^5F_4$ –$^5I_7$ and $^5S_2$–$^5I_7$ transitions.

References

[1] http://www.marketsandmarkets.com/Market-Reports/display-panel-market 213105372.html.

[2] M. Leskela, Journal of alloys and Compounds, 275, 702 (1998).

[3] H.C. Swart, E. Coetzee, J.J. Terblans, O.M. Ntwaeaborwa, P.D. Nsimama, F.B. Dejene, J.J. Dolo, Appl. Phys. A 101, 633 (2010).

[4] A.M. Chinie, S. Georgescu, A. Mateescu, A. Stefan, Rom. J. Phys. 51, 827 (2006).

[5] D. Kim, W. Kang, J. Bull. Korean Chem. Soc. 25, 12 (2004).

[6] J.Y. Choe, D. Ravichandran, S.M. Blomquist, D.C. Morton, K.W. Kirchner, M.H. Ervin, U. Lee, J. Appl. Phys. Lett. 78 (2001) 24.

[7] S. Khiari, F. Bendjedaa, M. Diaf, Optics and Photonics Journal 3, 13 (2013).

[8] L. S. Chamberlain, L. R. Corruccini, Phys. Rev. B 71 (2005) 024434 (7pp).

[9] A. Braud, P. Y. Tigreat, J. I. Doualan, R. Moncorge, Appl. Phys. B 72, 909 (2001).

[10] A. Braud, S. Girard, J. L. Doualan, M. Thuau, R. Moncorge, A. M. Tkachuk, Phys. Rev. B 61, 5280 (2000).

[11] Y. Kalisky, The Physics and Engineering of Solid State Lasers, 2006.

[12] J. Gonzalo, R. Gomez San Roman, J. Perriere, C. N. Afonso, R. Perez Casero , Appl. Phys. A 66, 487 (1998)

[13] S. S. Yi, J. S. Bae, B. K. Moon, J. H. Jeong, I. W. Kim, H. L. Park, Appl. Phys. A 76, 433 (2003).

[14] S.T.S. Dlamini, H.C. Swart, J.J. Terblans, O.M. Ntwaeaborwa, Solid State Sciences 23 (2013).

[15] J. S. Bae, K.S. Shim, S.B. Kim, J.H. Jeong, S.S. Yi, J.C. Park, J. Cryst. Growth 264, 290 (2004).

[16] Z. Zhang, C. Bao, S. Ma, L. Zhang, S. Hou, Journal of the Australian Ceramic Society, 48, 214 (2012).

[17] K. Hillie, H. Swart, Applied Surface Science 183, 304 (2001).

[18] Y. Ogura, M. Kondo, T. Morimoto, A. Notomi, T. Sekigawa, Mater. Trans. 42, 1124 (2001)

[19] J. J. Dolo, O. M. Ntwaeaborwa, J. J. Terblans, E. Coetsee, B. F. Dejene, M. M. Biggs, H. C. Swart, Appl. Phys. A, 101, 655 (2010).

[20] P. Orgiani, R. Ciancio, A. Galdi, S. Amoruso, and L. Maritato, Appl. Phys. Lett. 96, 032501 (2010).

[21] M. Acosta, I. Riech, E. Martin-Tovar, Advances in Condensed Matter Physics, Volume 2013, Article ID 970976.

[22] D. P.Norton, Materials Science and Engineering R 43, 239 (2004).

[24] A. Pandey, V. Kumar, Dalton Trans. 42, 11005 (2013).

Chapter 8

Pulsed laser deposited $KY_3F_{10}:Ho^{3+}$ thin films: Influence of target to substrate distance

8.1 Introduction

Fluoride materials are promising candidates for display devices based on thin film phosphors because of their low phonon energies. This reduces the non-radiative quenching phenomena so that high luminescence efficiency can be obtained, which is required for any display devices [1-2].

Because of its good optical, thermal and mechanical properties which are comparable to other fluoride materials such as $LiYF_4$, potassium triyttrium decafluoride (KY_3F_{10}) has attracted much attention. In addition, it is reported that this material has much higher energy transfer efficiency in it than other fluoride materials such as BaY_2F_8 and $LiYF_4$ [3]. Moreover, doping with holmium has significant advantage over other rare earth ions because of its high-gain cross section and long life time of $^5I_7$ upper level emission resulting in high energy storage capability and efficiency [4].

The unique advantage of displays based on thin film phosphors is that they are characterized by high contrast and resolution, good thermal conductivity as well as a high degree of uniformity and better adhesion [5-8]. Thin films of $KY_3F_{10}:Ho^{3+}$phosphor can be prepared using one of the thin film deposition techniques called pulsed laser deposition (PLD). PLD is a thin film deposition technique which has been popular, versatile and highly flexible method for the thin film growth of various materials. Using this technique the advantage of controlling thin film stoichiometry accurately can be achieved by controlling deposition parameters. The target to substrate distance (d_{ts}) is one of the most critical factors which affects the quality of films in PLD. The hemispherical expansion of the laser induced plasma plume increases with increasing d_{ts}. This reduces the particle flux of the target species over the substrate area which affects the quality of the film [9].

Therefore, in this paper, we report the influence of target to substrate distance on the structural, morphological and PL properties of $KY_3F_{10}:Ho^{3+}$ thin films prepared by PLD. The aim of this

study is to identify optimal d_{ts} value that will result in better structure, morphology and high PL intensity of this material for potential applications in future display devices.

8.2 Experimental details

Preparation of $KY_3F_{10}:Ho^{3+}$ thin films is carried out by using Nd-YAG laser (266 nm, pulse duration of 10ns, repetition rate of 2 Hz). The laser fluence is kept at $1.2\ J/cm^2$. The vacuum chamber is pumped to a background pressure of 4×10^{-5} mbar before introducing argon. The films are grown at different target to substrate distances of 4, 5 and 6.7 cm on (100) silicon substrate. The gas pressure is kept at 1.7 Torr and the substrate temperature is 600 ^oC. The targets are made from commercial $KY_3F_{10}:Ho^{3+}$ powder pressed in to pellets. The crystal structure of the films is analyzed by X-ray diffraction (XRD) using Bruker D8 advance X-ray diffractometer operating at 40 kV and 40 mA using Cu Kα = 0.15406 nm. The morphology of the films is studied using Field Emission Scanning Electron Microscope (FE-SEM) and Atomic Force Microscope (AFM) with ScanAsyst in tapping mode. Energy Dispersive X-ray Spectrometer (EDS) is employed to analyze the elemental composition of the deposited films. The PL excitation and emission spectra are measured at room temperature using Cary Eclipse fluorescence spectrometer model: LS-55 with a built-in 150 W xenon flash lamp. The optical properties of the films are studied using UV-VIS spectrometer in the wavelength range of 250-800 nm. The values of the chromaticity coordinates of the phosphor thin films have been estimated from the 1931 Commission Internationale de l'Eclairage (CIE) system using the excitation wavelength of 454 nm.

8.3 Results and discussion

8.3.1 Structural and morphological properties

Figure 8.1 depicts the XRD pattern of the films deposited at different target to substrate distances for constant deposition temperature of 600 ^oC and argon gas pressure of 0.5 Torr. The miller indices of the prominent peaks are shown. This result indicates that the films crystallized in tetragonal structure of KY_3F_{10} (in agreement with JCPDS card No 27-0465).

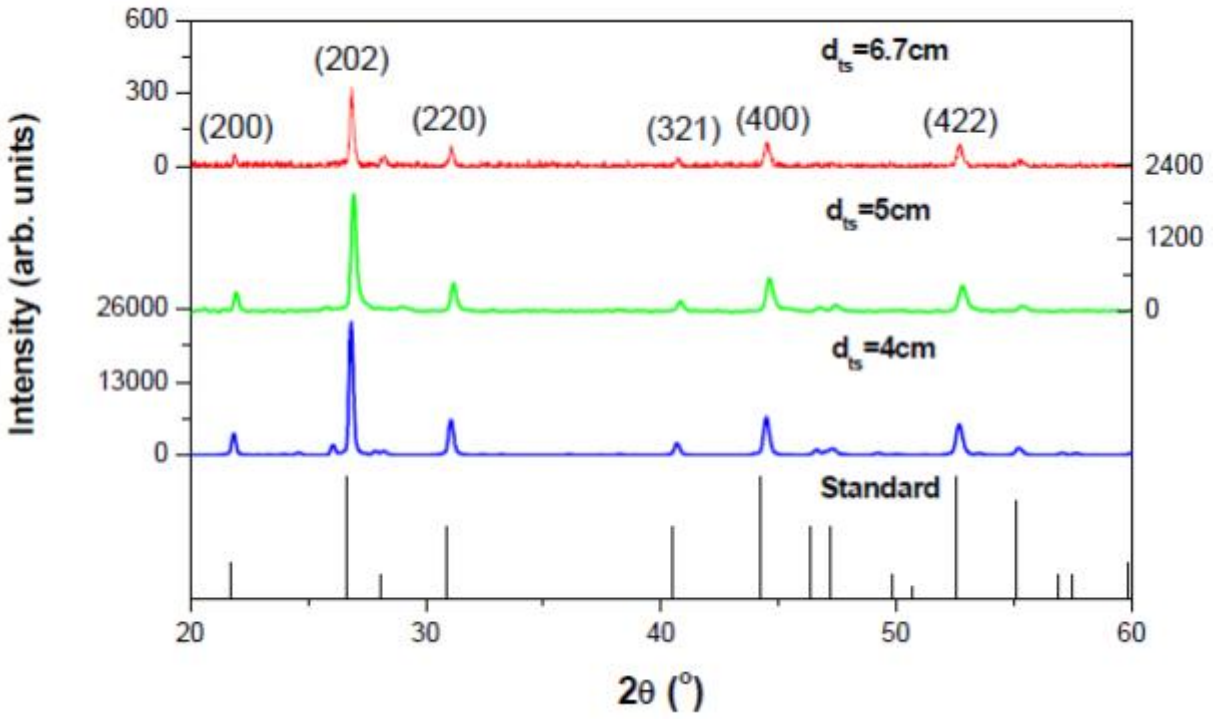

Fig. 8.1: XRD pattern of $KY_3F_{10}:Ho^{3+}$ thin films prepared at different target to substrate distances. The standard is included for comparison.

The film deposited at $d_{ts} = 4$ cm has relatively the highest diffraction peaks among all samples, suggesting that better crystalline quality was obtained at this particular value of d_{ts}. We present the change in the degree of crystallinity of the films in terms of the actual surface temperature of the films which is because of two factors. The first factor is the substrate heating by the heater and the second factor is the kinetic energy of the vapor species striking the surface. Since the substrate heating by the heater is kept constant at 600 ^{o}C, the second factor might have influenced the structure of the films. At lower values of d_{ts}, fewer collisions occur within the plasma and the target species strike the substrate with relatively high kinetic energy. In other words, the vapor species travelling for relatively larger distances will make higher number of collisions with the background gas molecules and hence have lower kinetic energy when reaching the substrate as compared to the species travelling for shorter distance. Therefore, the substrate located at $d_{ts} = 4$ cm has the highest actual surface temperature and adatom mobility resulting in improved crystallinity with increased grain size as compared to those located at

$d_{ts} = 5$ and 6.7 cm. The largest grain size obtained at $d_{ts} = 4$ cm is attributed to Ostwald ripening process [10].

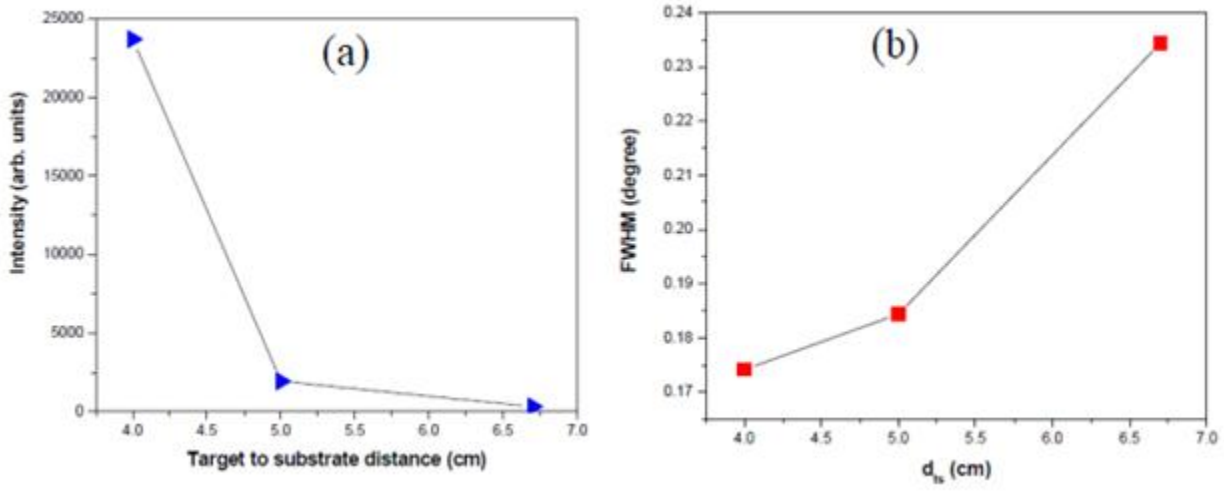

Fig. 8.2: (a) Intensity of the (202) diffraction peak in the XRD pattern of films as a function of d_{ts} , (b) d_{ts} dependence of the FWHM of the dominant (202) diffraction peak.

Further information about the crystalline quality of the deposited films can be obtained from the d_{ts} dependence of the FWHM shown in Figure 8.2(b) using the dominant (202) diffraction peak. The increment in FWHM at $d_{ts} = 5$ and 6.7 cm compared to its value at $d_{ts} = 4$ cm indicates the decrease in crystallinity with rise in d_{ts} [11-12].

This degradation in crystalline quality of the films at higher values of d_{ts} could be attributed to the lowering of the species kinetic energy due to prolonged collisions with background gas molecules. The average crystallite size has been computed from the full width half maximum (FWHM) of the dominant peaks using equation (5.2):

The average crystallite size of the films varied between 30 and 40 nm and decreases with increasing d_{ts} as shown in Figure 8.3. All the 2θ values of the diffraction peaks are slightly shifted to higher angles as compared to the powder (JCPDS 27-0465). This causes a slight decrement in d-values according to Bragg diffraction equation $n\lambda = 2d\sin\theta$, indicating the existence of compressive strain in the deposited films. The strain (ε) developed in the prepared films was evaluated from the following relation [13].

$$\varepsilon = \frac{\beta}{4\tan\theta} \qquad (8.1)$$

As shown in Figure 8.3, the relatively larger strain developed in the film deposited at $d_{ts} = 6.7$ cm (Table 8.1) caused cracking of the film. The lattice parameters a and c were calculated using the Bragg diffraction equation and the lattice equation for tetragonal structure.

$$\frac{1}{d_{hkl}{}^2} = \frac{h^2 + k^2}{a^2} + \frac{l^2}{c^2} \qquad (8.2)$$

where d_{hkl} is the interplanar distance and h, k, l are the miller indices. The evaluated values of a, c and cell volume, respectively, are $a = 7.6\text{Å}$, $c = 10.8\text{Å}$ and $V = 623.8\text{Å}^3$. The evaluated lattice parameters are close to the standard values $a = 8.161\,\text{Å}$, and $c = 11.53\,\text{Å}$. Quantitative information concerning the preferential crystallite orientation was obtained from the texture coefficient ($TC(hkl)$). It represents the texture of a particular plane and its deviation from unity implies a preferred growth. $TC(hkl)$ is defined as,

$$TC(hkl) = \frac{I(hkl)/I_0(hkl)}{N^{-1}\sum_N (I(hkl)/I_0(hkl))} \qquad (8.3)$$

where $I(hkl)$ is the measured intensity of (hkl) diffraction peak, $I_0(hkl)$ is the standard intensity of JCPDS and N is the total number of diffraction peaks considered in the analysis. The value of $TC(202)$ for the (202) peak of all the films is greater than unity indicating preferential growth of $KY_3F_{10}:Ho^{3+}$ crystal along C-axis.

The film thickness (t) is also an important parameter in the study of film properties. The thickness of the films is estimated using a weight difference method employing a sensitive electronic microbalance and is given by [14],

$$t = \frac{m_2 - m_1}{\rho A} \qquad (8.4)$$

where m_1 and m_2 respectively, are the masses of the substrate before and after deposition, ρ is the density of the film material (g/cm^3) and A is the area of the film (cm^2). The evaluated film thicknesses are $t = 724, 605$ and 452 nm for $d_{ts} = 4, 5$ and 6.7 cm respectively.

Table 8.1: Film thickness, average crystallite size, FWHM for the dominant (202) peak and the strain developed in the prepared films.

d_{ts} (cm)	Film thickness (nm)	Average crystallite size (nm)	FWHM (for the dominant (202) peak)	Strain (using the dominant (202) peak)
4	724	40	0.17417	0.18277
5	605	37	0.18439	0.19350
6.7	452	30.2	0.23432	0.24589

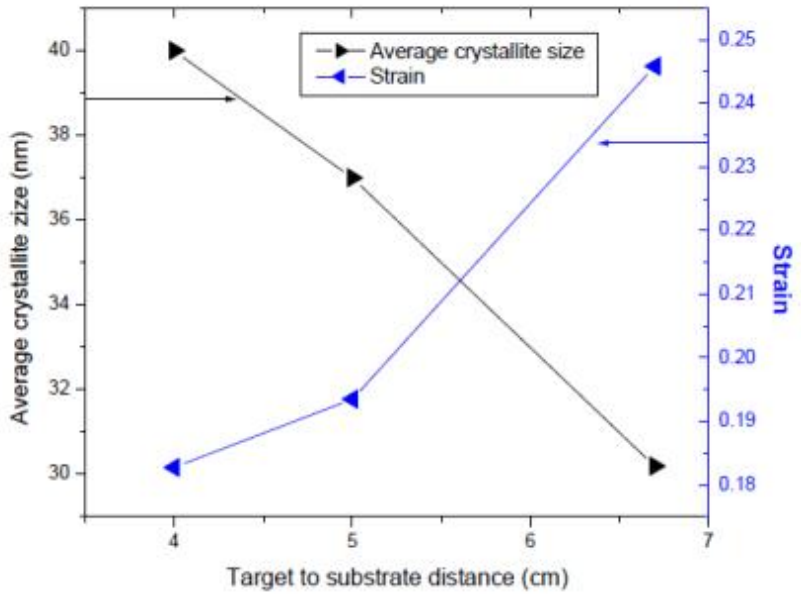

Fig. 8.3: Average crystallite size and strain as a function of target to substrate distance.

The decrease in film thickness for relatively larger d_{ts} values could be attributed to the decrease in deposition rate at such larger distances. The hemispherical expansion of the laser induced plasma plume increases with increasing d_{ts}. This reduces the particle flux of the target species over the substrate area which lowers the deposition rate [9]. Figure 8.4 shows the FE-SEM images of the films with clearly different morphologies. The image of the film deposited at $d_{ts} = 4$ cm shows clear grains of the film with well defined shapes. It is clearly visible that the images consist of grains with very small as well as large sizes and the larger grains decrease in size as the value of d_{ts} is increased. The morphology of the highly crystalline film deposited at $d_{ts} = 4$ cm is further investigated by AFM.

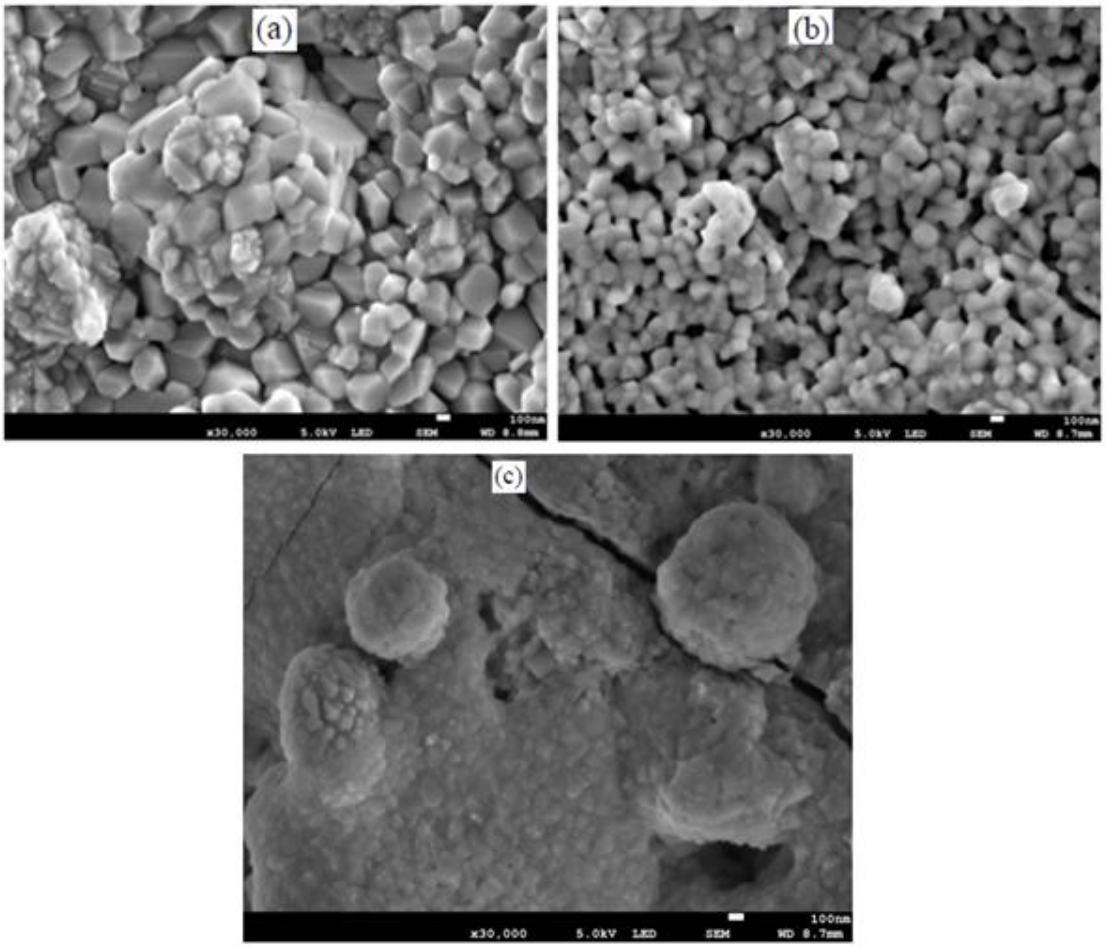

Fig. 8.4: FE-SEM images of the films deposited at (a) $d_{ts} = 4$ cm, (a) $d_{ts} = 5$ cm, (a) $d_{ts} = 6.7$ cm.

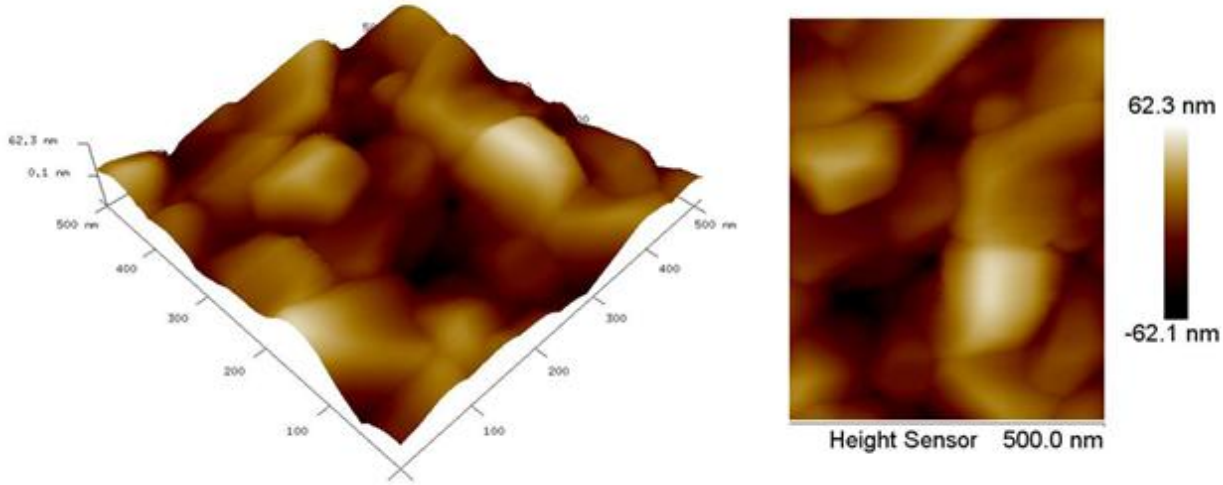

Fig. 8.5: AFM images of the film deposited at $d_{ts} = 4$ cm.

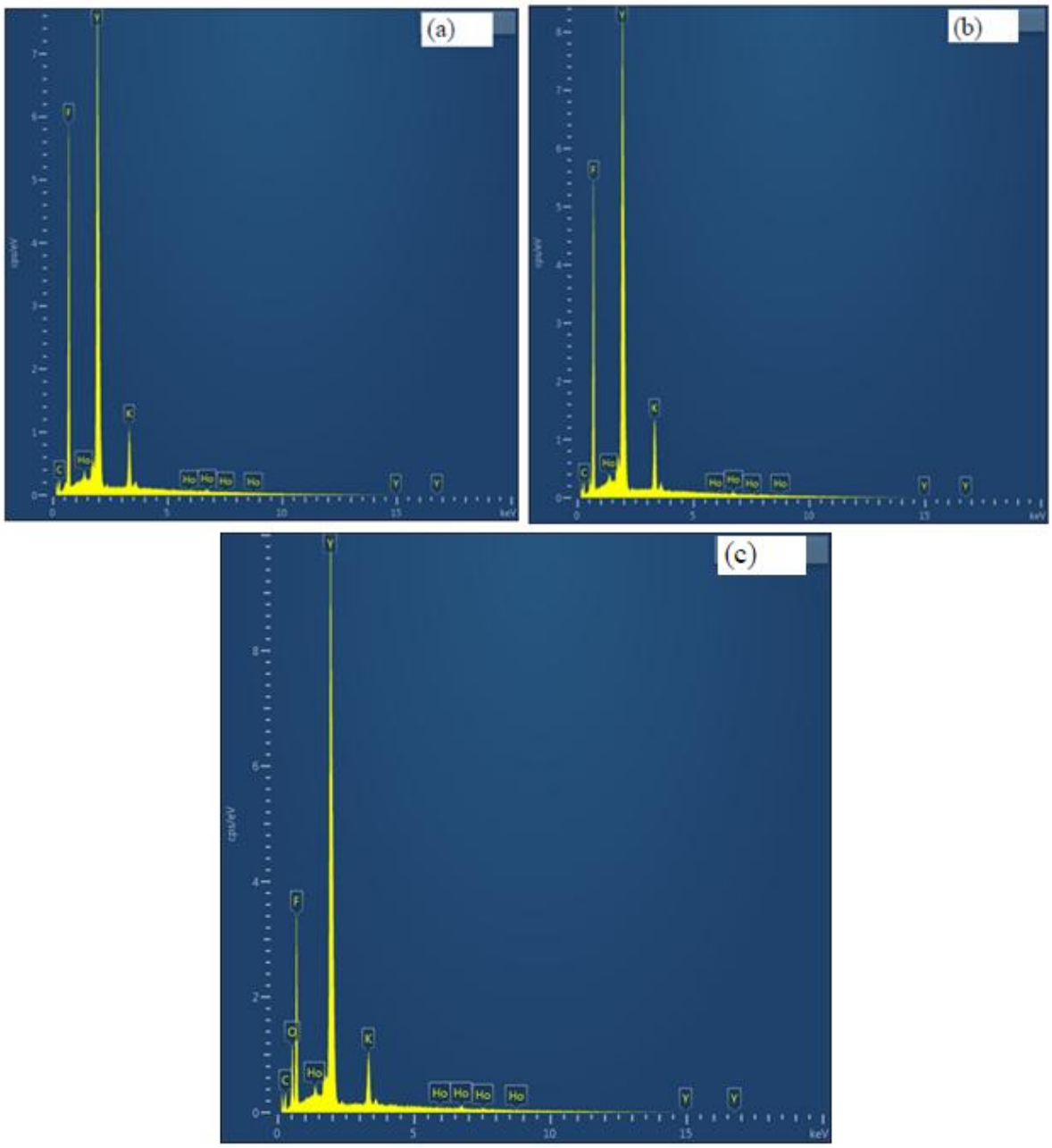

Fig. 8.6: EDS spectra of the films deposited at (a) $d_{ts} = 4$ cm, (a) $d_{ts} = 5$ cm, (a) $d_{ts} = 6.7$ cm.

The 3D and 2D AFM images of this film are shown in Figure 8.5. The observed root mean square (RMS) roughness of this film over 0.5 μm × 0.5 μm region is 17.6 nm. Figure 8.6 shows the EDS spectra of the deposited films. It is clear that all the constituent elements of the target are also present in the films. Common impurities such as carbon and oxygen also appeared in the

spectra. The source of carbon could be the carbon tape used during measurements and oxygen might have reacted with the films during their removal from the chamber.

8.3.2 Photoluminescence properties

Figure 8.7(a) shows the normalized PL emission spectra of $KY_3F_{10}:Ho^{3+}$ thin films deposited at $d_{ts} = 4$ cm for different excitations. Green emission at about 540 nm was investigated at four excitation wavelengths; namely: 362, 416, 454, and 486 nm. In addition, faint red emission was observed at 750 nm for all excitations.

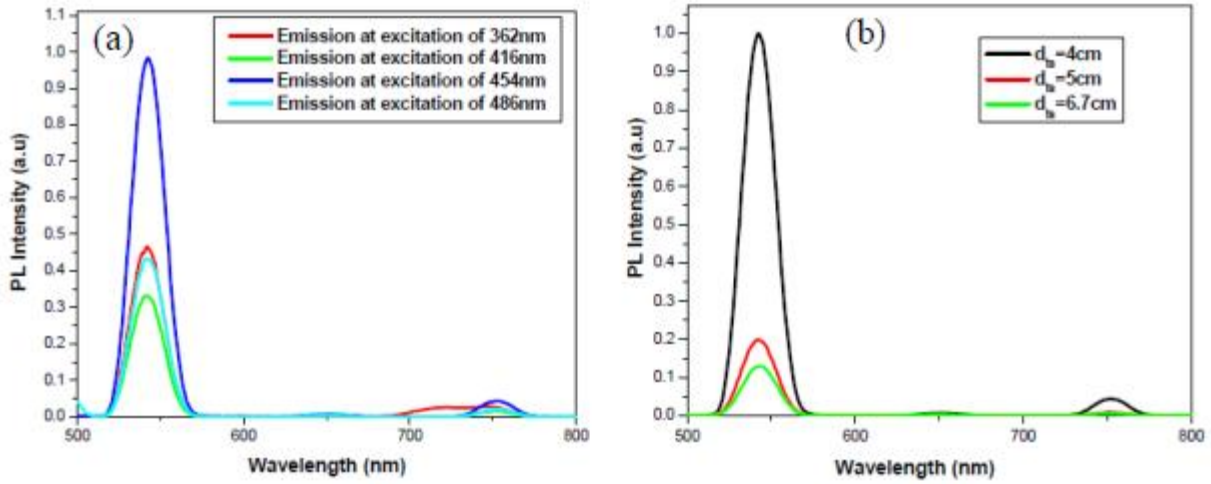

Fig. 8.7: Normalized (a) PL emission spectra of $KY_3F_{10}:Ho^{3+}$ thin films deposited at $d_{ts} = 4$ cm, (b) PL emission spectra of the films monitored at excitation of 454 nm.

The green emission at 540 nm is attributed to the $^5F_4$–$^5I_8$ and $^5S_2$–$^5I_8$ transitions while the faint red emission at 750 nm is due to the $^5F_4$–$^5I_7$ and $^5S_2$–$^5I_7$ transitions of Ho^{3+} (Figure 8.8). Such multiple emissions from other holmium doped phosphor are also reported in literature [15]. The peak maximum of the emission spectra first decreases and increases rapidly at excitation of 454 nm and then decreases again. This shows that excitation wavelength of 454 nm should be used for more efficient emission in the possible device applications of thin films of this material. Similar results were obtained for the films deposited at $d_{ts} = 4$ and 6.7 cm.

Figure 8.7(b) shows the normalized PL emission spectra of the films monitored at excitation of 454 nm. As shown, the highest PL emission was obtained for the film deposited at $d_{ts} = 4$ cm. This could be attributed to the improved crystalline quality of the film deposited at this particular value of d_{ts}.

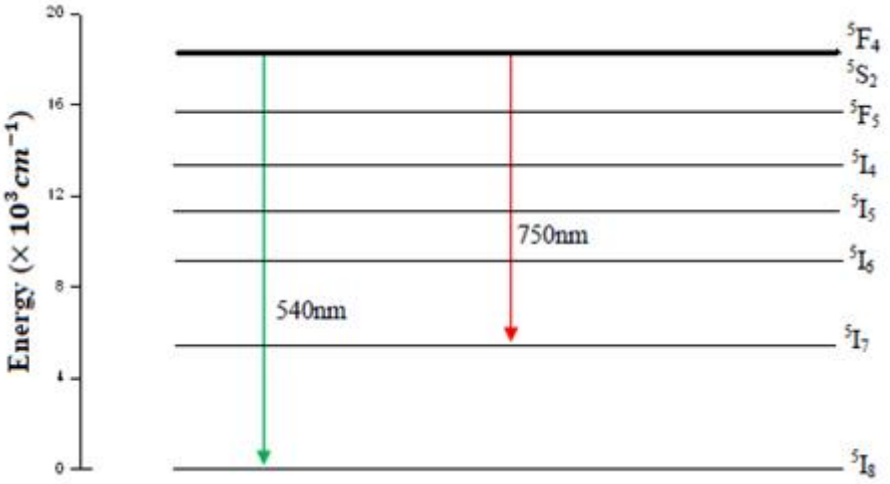

Fig. 8.8: Energy level diagram of Ho^{3+} in KY_3F_{10}. The arrows indicate the observed transitions.

The variation of emission peaks with target to substrate distance is shown in Figure 8.9(a) for excitation wavelengths of 362, 416, 454 and 486 nm. It can be observed that higher emission peaks were observed at lower values of d_{ts} for all excitation wavelengths.

The values of the chromaticity coordinates of $KY_3F_{10}: Ho^{3+}$ thin films have been estimated from the 1931 Commission Internationale de l'Eclairage (CIE) system using the excitation wavelength of 454 nm (Figure 8.9(b)).

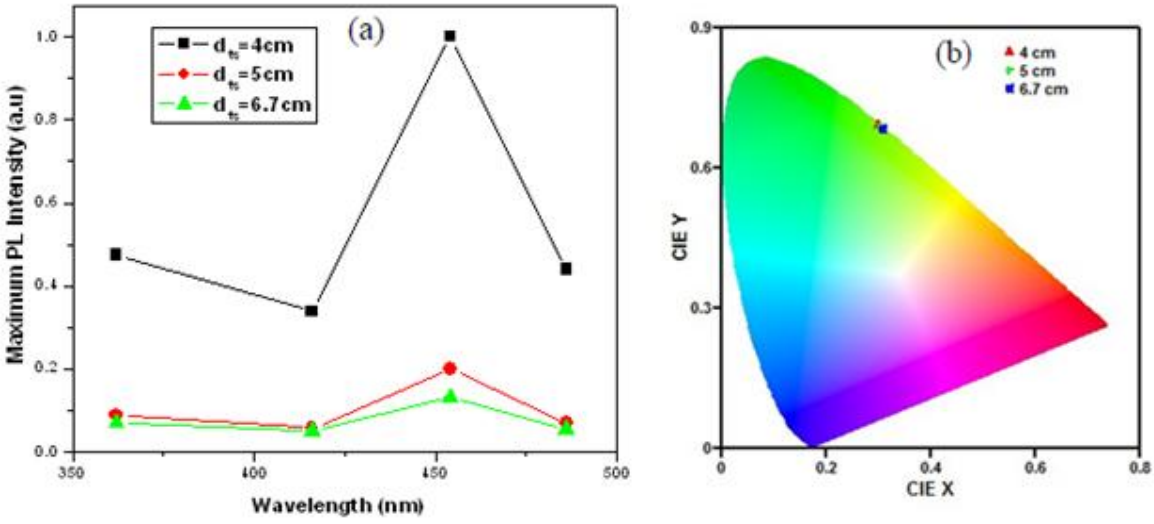

Fig. 8.9: (a) Variation of emission peaks maxima corresponding to the excitation wavelengths, (b) CIE coordinates for each value of d_{ts}.

This system helps us visualize the variation in color emitted from samples and the coordinates are measured as (x,y). Though the values are found in green region for all the thin films, slight shift to deep green region was obtained for the film deposited at $d_{ts} = 4$ cm.

8.3.3 Optical properties

The optical properties of $KY_3F_{10}:Ho^{3+}$ thin films grown at different target to substrate distances were measured at room temperature in the wavelength range of 250-800 nm. Figure 8.10 shows the reflectance (R) spectra of the films. As can be seen from the Figure, the prepared films are characterized with low reflectance (less than 30%) for wavelength values greater than 400 nm (visible region) regardless of the target to substrate distance. Moreover, it is worth noting that the reflectance increases with increasing film thickness. The absorption spectra of the films are also shown in Figure 8.11. All the films are characterized by high absorption in the visible region. The band gap of KY_3F_{10} host material is of the order of 10 eV and this corresponds to a wavelength of about 124 nm. Therefore, the lower wavelength region of the reflectance (absorbance) spectrum is not observed as the employed UV-VIS spectrometer functions in the wavelength range of 250-800 nm.

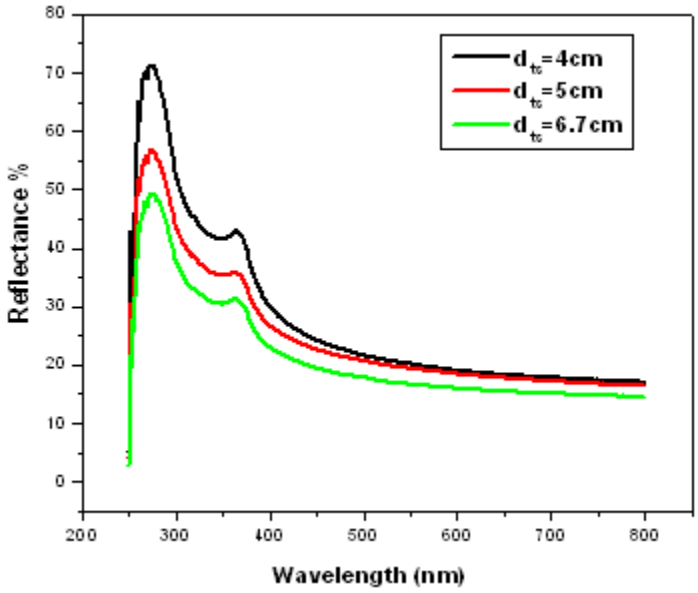

Fig. 8.10: Reflectance spectra of the films deposited at different target to substrate distances.

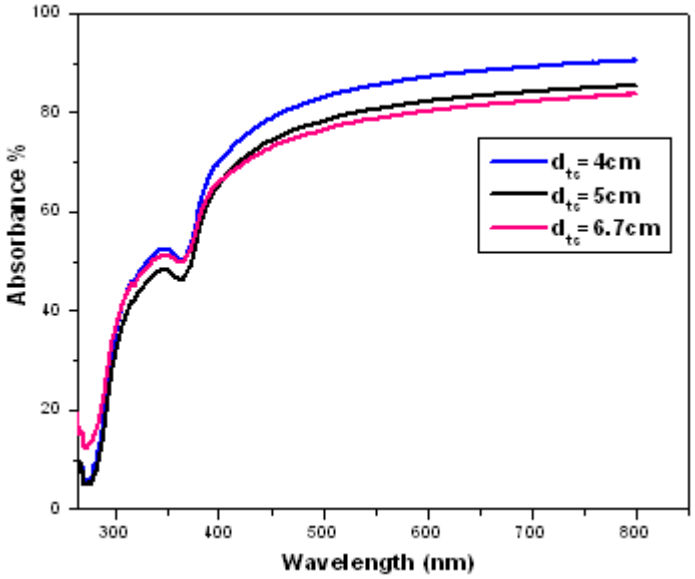

Fig. 8.11: Absorption spectra of the deposited films.

8.4 Conclusion

The effect of target to substrate distance on structural, morphological and PL properties of pulsed laser deposited $KY_3F_{10}:Ho^{3+}$ thin films is investigated. The degradation in crystalline quality is observed at larger values of d_{ts} during deposition. The estimated thickness of the films decreases with increasing d_{ts} and this could be attributed to the decrease in deposition rate at such larger distances. Green emission at 540 nm is investigated at four excitation wavelengths; namely: 362, 416, 454 and 486 nm. In addition, faint red emission is observed at 750 nm for all excitations. The highest PL intensity is observed for the film deposited at 4 cm and this is attributed to the improved crystalline quality of the film. The highest PL emission is observed for excitation of 454 nm for all the deposited films. This shows that excitation wavelength of 454 nm should be used for more efficient emission in the possible device applications of thin films of this material.

References

[1] L. S. Chamberlain, L. R. Corruccini, Phys. Rev. B 71, 024434 (2005).

[2] K. Jin Kim, et al., J. Cryst. Growth 299, 171 (2007).

[3] A. Braud, S. Girard, J. L. Doualan, M. Thuau, R. Moncorge, A. M. Tkachuk, Phys. Rev. B 61, 5280 (2000).

[4] Y. Kalisky, The Physics and Engineering of Solid State Lasers, USA, 2006.

[5] M. Leskela, J. Alloy. Compd. 275, 702 (1998).

[6] A.M. Chinie, S. Georgescu, A. Mateescu, A. Stefan, Rom. J. Phys. 51, 827 (2006).

[7] K. Sohn, D. H. Park, J. G. Yoo, J. S. Kim, Jpn. J. Appl. Phys. 44, 1787 (2005).

[8] J. S. Bae, J. P. Kim, U. C. Choi, J. Korean Phys. Soc. 49, 616 (2006).

[9] A. T. T. Mostako, Alika Khare, Appl. Nanosci. 2, 189 (2012).

[10] M. Acosta, I. Riech, and E. Martín-Tovar, Adv. Cond. Matter Phys. 2013, 1 (2013).

[11] J.-H. Kim, S. Lee, H.-S. Im, Appl. Phys. A 69, 629 (1999).

[12] Z. Zhang, C. Bao, S. Ma, L. Zhang and S. Hou, J. Aust. Ceram. Soc. 48, 214 (2012).

[13] S. Ting, J. Nanomat. 2012, 1 (2012).

[14] S. Jassim, A. Zumaila, G. Abdella, Results in Physics 3, 173 (2013).

[15] A. Pandey and V. K. Rai, Dalton Trans. 42, 11005 (2013).

Chapter 9

Enhanced emission and improved crystallinity of $KY_3F_{10}:Ho^{3+}$ thin films grown at high deposition temperature

9.1. Introduction

Fluoride based materials are very attractive since they possess a reasonably high thermal conductivity, good enough mechanical hardness, and high chemical stability compared with other low phonon energy materials such as chlorides, bromides, or sulphides [2-8]. In particular, potassium triyttrium decafluorde (KY_3F_{10}) host material has much higher energy transfer efficiency in it than other fluorides such as BaY_2F_8 and $LiYF_4$ [7] and this makes it an interesting material for luminescence applications.

Because of its excellent material properties potassium triyttrium decafluorde doped with holmium phosphor ($KY_3F_{10}:Ho^{3+}$) has attracted much attention and extensively studied [1-5]. It is used for various applications in a wide range of fields such as for optical studies [2-3], laser applications [3], scintillation [4], and displays [5-6].

Doping of KY_3F_{10} host with holmium has significant advantage over other rare earth ions because Ho^{3+} ion has high-gain cross-section and long life-time of $^5I_7$ upper level emission that results to high efficiency and energy storage capacity [8]. Though this material is extensively studied in powder form [1-8], its thin films are not yet much investigated to the best of our knowledge.

In device applications such as field emission displays (FED), thin film phosphor materials are more advantageous than powders in reducing outgassing problems as well as having high resolution and contrast [9]. Therefore, the study of thin film phosphors is equally important as that of their powder counterparts.

In the preparation of thin films, different deposition techniques such as pulsed laser deposition (PLD), chemical vapor deposition, and magnetron sputtering can be used. Among these methods PLD method has been a popular, versatile and highly flexible thin film deposition technique for a wide range of materials. The method is based on the interaction of a high power density laser beam with a solid target so that the laser energy can easily be controlled externally [10].

The quality of the films deposited on a substrate is dependent on the deposition parameters, such as background gas pressure, temperature and the type of background environment. In the previous published articles [10-12], it is reported that during the films growth process, the background gas pressure and the substrate temperature are the two major critical parameters that determine (i) the final step of the film formation and (ii) the amorphous or the crystalline nature of the deposited films.

In this paper, the influence of temperature on structural, morphological and photoluminescence properties of thin films of $KY_3F_{10}:Ho^{3+}$ deposited over a wide temperature ranging from 50 - 600 ^oC on silicon substrate are investigated. Though similar growth mechanism can be obtained at low (including room temperature) and high temperature depositions for most materials [13-15], a completely different growth mechanism and film quality were obtained for $KY_3F_{10}:Ho^{3+}$at low and high temperature regions. This shows that the growth mechanism and the film quality during PLD process do not only depend on the deposition parameters mentioned above, but also on the type of material ablated as well.

9.2. Experimental details

The $KY_3F_{10}:Ho^{3+}$ thin films were deposited using PLD technique. Nd-YAG laser (wavelength of 266 nm, pulse duration of 9.3 ns, repetition rate of 10 Hz), with the laser fluence kept at $1.2\ J/cm^2$) is used to grow $KY_3F_{10}:Ho^{3+}$ thin films on (100) Si substrate in argon environment. Before introducing the argon, the vacuum chamber is pumped to a background pressure of 5.6×10^{-5} mbar. A commercially available $KY_3F_{10}:Ho^{3+}$ powder is used to prepare the target by compressing it at 6 MPa. Keeping the gas pressure at constant value of 1.7 Torr and the target-to-substrate distance at 5.2 cm, the thin films are grown at substrate temperatures of 50, 100, 350, 400, 500, and 600 °C. XRD analysis by Bruker D8 advance X-ray diffractometer (operating at 40 kV, 40 mA, and Cu k_α = 0.15406 nm) is employed to determine the crystal structure of the films. Field Emission Scanning Electron Microscope (FE-SEM) and Atomic Force Microscope (AFM) with ScanAsyst in tapping mode are used to analyze the morphology of the films. The elemental composition of the films is studied using Energy Dispersive X-ray Spectrometer (EDS). X-ray Photoelectron Spectroscopy (XPS) is employed to investigate the surface states. The measurement of the room temperature PL excitation and emission spectra are performed by using a Cary Eclipse Fluorescence Spectrometer (model: LS-55 with a built-in 150 W Xenon

flash lamp). For the excitation wavelength of 454 nm, the chromaticity coordinates of the prepared thin films are estimated from the 1931 Commission Internationale de l'Eclairage (CIE) system.

9.3 Results and discussion:

9.3.1 Structural and morphological properties

Figure 9.1 depicts the XRD pattern of $KY_3F_{10}:Ho^{3+}$ thin films grown at different substrate temperatures for a constant deposition pressure of 1.7 Torr in argon atmosphere. It is observed that for the films deposited above the substrate temperature of 350 ^oC, the degree of crystallinity is enhanced with an increase in deposition temperature.

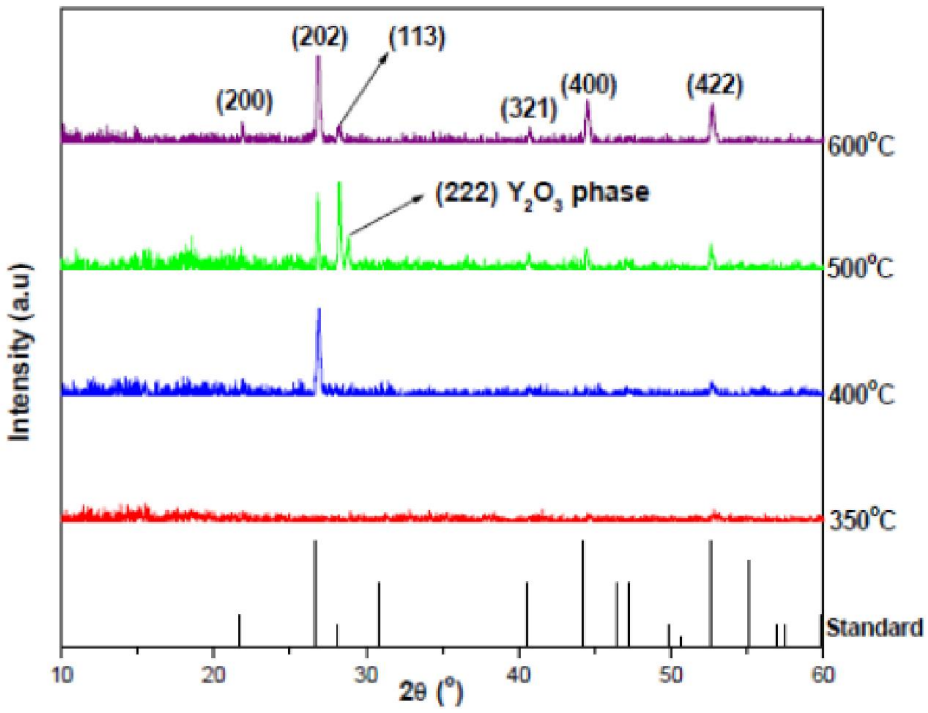

Fig. 9.1: XRD spectra of $KY_3F_{10}:Ho^{3+}$ thin films deposited at constant argon gas pressure of 1.7 Torr for various deposition temperatures. For comparison, the spectrum of the standard is included.

The labels shown in Fig, 9.1 are according to the miller indices of the diffraction peaks of the planes. The films crystal structure is found be tetragonal form of KY_3F_{10} which is in agreement with JCPDS card No 27-0465.

For low substrate temperatures between 50 – 350 ^oC, no diffraction peaks are visible (not plotted) which indicates that the deposited thin films are amorphous. When the deposition

temperature increases to 400 ^{o}C and above the diffraction peaks becomes visible, That is, at 400 ^{o}C the (202) diffraction peak is visible while at 500 ^{o}C, in addition to the (202) the (113) diffraction peak becomes visible. Further, increasing the deposition temperature to 600 ^{o}C three relatively intense diffraction peaks, namely the (202), (400) and (422) as well as three less intense peaks corresponding to the (200), (113) and (321) diffraction planes are observed. Consequently, it may be concluded that the degree of crystallinity of the prepared thin films is improved with an increase of the deposition temperature. The (113) peak, which is normally not observed for the film deposited at 400 ^{o}C and much less intense for the film deposited 600 ^{o}C, becomes dominant for the one deposited at 500 ^{o}C. This could be because of the change in the preferred orientation of the films with change in deposition temperature.

The improved of the crystallinity of the samples with an increase in substrate temperature can be explained in terms of the dependence of the mobility of the atoms as a function of temperature. That is, for relatively low temperatures, the vapor species have a low surface mobility and will be located at different positions on the surface. However, as the substrate temperature is high enough, the particles arriving at the substrate surface will have higher thermal energy that results to an increase in the mobility of the ad-atoms. This, in turn, makes the particles coalesce with each other to form the nucleation centers, thereby increasing the quality of the thin films.

Table 9.1: The FWHM of the dominant (202) peaks, the calculated average crystallite size, and the strain developed in the samples for different temperatures.

Substrate temperature (^{o}C)	2θ (^{o})	FWHM	Average crystallite size (nm)	Strain
400	26.893	0.20940	39	0.2189
500	26.834	0.16131	51	0.1691
600	26.873	0.10966	74	0.1148

The average crystallite size (D) of the samples is determined from the full width at half maximum (FWHM) of the most intense (202) diffraction peaks using equation (5.2).

The strain (ε) developed in the prepared films is calculated using the following relation: [16]

$$\varepsilon = \frac{\beta}{4\tan\theta} \qquad (9.1)$$

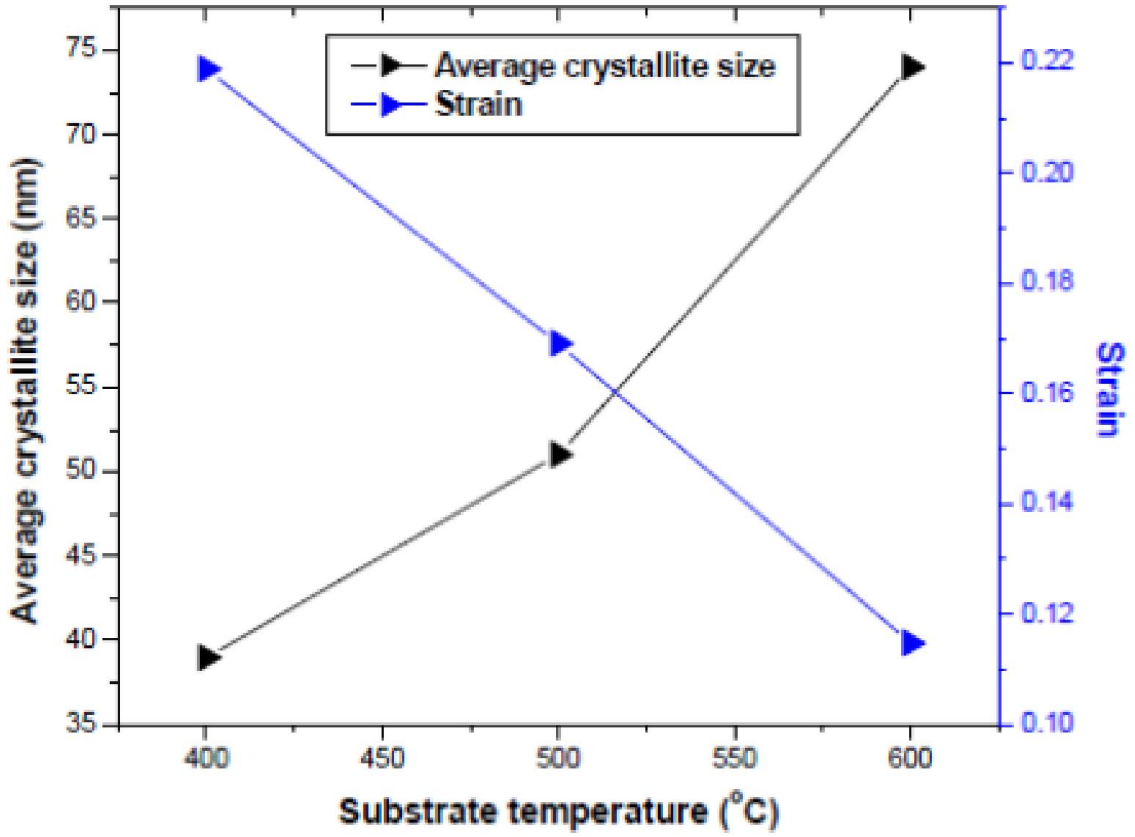

Fig. 9.2: The substrate temperature versus average crystallite size and strain for $KY_3F_{10}:Ho^{3+}$ thin films.

The calculated crystallite sizes and the strain parameter at different temperatures are displayed in Table 9.1. The crystallite sizes are in the range of 39 - 74 nm, whereas the corresponding strain varies between 0.2189 and 0.1148. Similar results showing an increase in crystallite size with substrate temperature were reported in literatures [17-21]. The substrate temperature versus

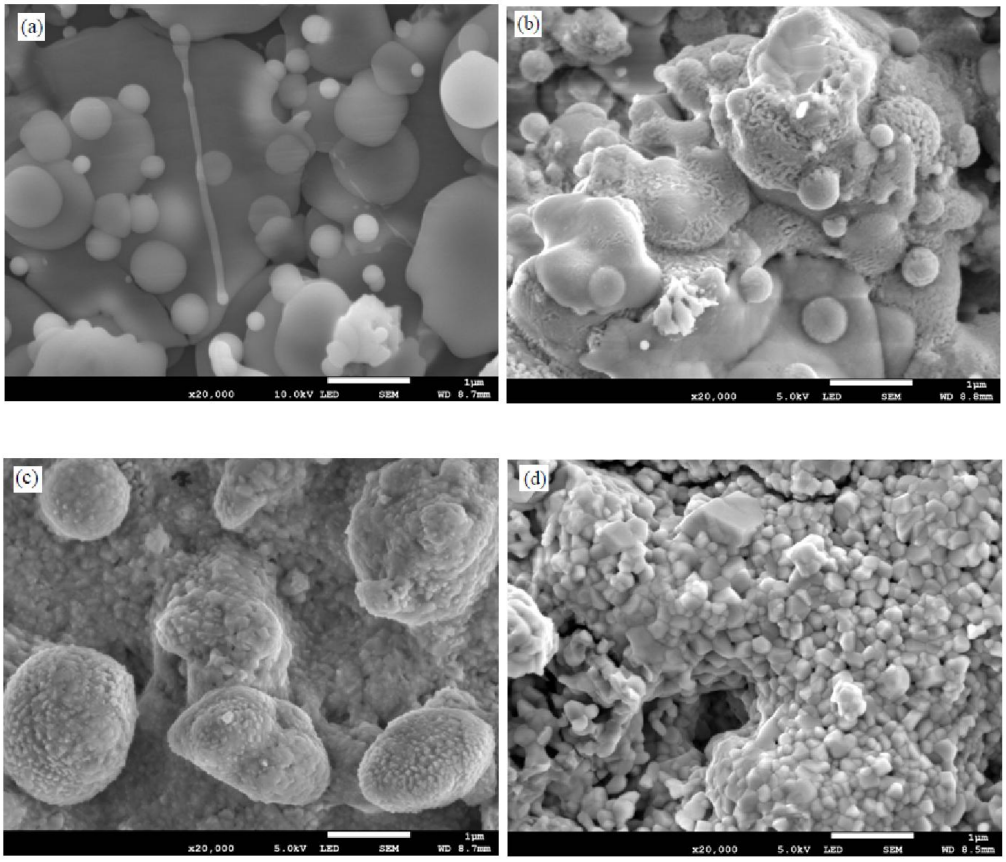

Fig. 9.3: FE-SEM images of the thin films deposited at (a) 350 ^{o}C, (b) 400 ^{o}C, (c) 500 ^{o}C, (d) 600 ^{o}C.

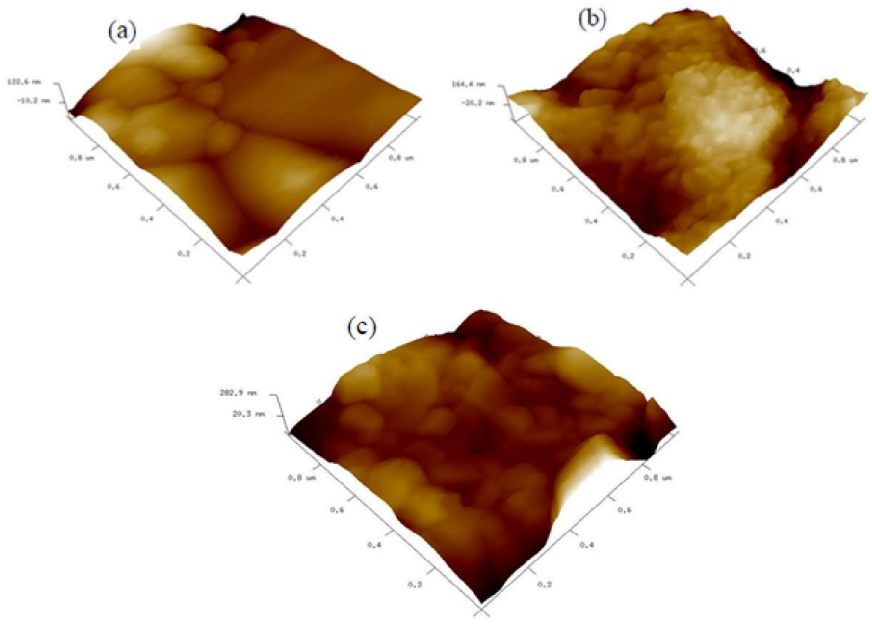

Fig. 9.4: AFM images of the thin films deposited at (a) 400 ^{o}C, (b) 500 ^{o}C, (c) 600 ^{o}C.

average crystallite size and strain is depicted in Fig. 9.2. It can be clearly observed from this Figure that the strain developed in the films decreases with increasing substrate temperature in an approximately linear relation, while the average crystallite size increases.

The morphology of the prepared thin films is analyzed using FE-SEM. Figure 9.3 shows the FE-SEM images of the deposited films. It is observed that for the film that is deposited at 50 ^{o}C, the morphology is dominated by the presence of loosely packed small and large droplet-like structures. Similar structures are observed for the films grown at substrate temperature of 100 ^{o}C and 350 ^{o}C. For the film deposited at 400 ^{o}C, smaller irregular and denser structures appear to be superimposed over the droplet-like structures. A further increase in substrate temperature to 500 ^{o}C results in the formation of different morphology consisting of mainly irregular large structures which seems to be composed of relatively tiny irregular particles.

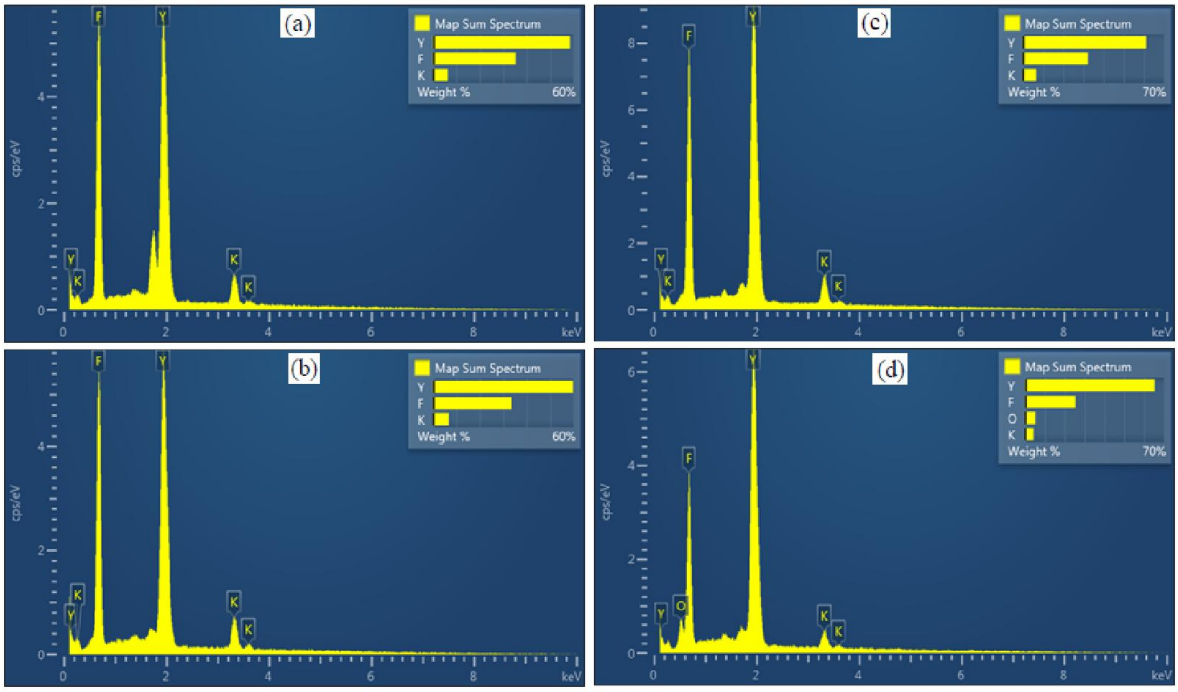

Fig. 9.5: EDS spectra of the thin films deposited at (a) 350 ^{o}C, (b) 400 ^{o}C, (c) 500^{o}C, and (d) 600 ^{o}C.

Furthermore, at the substrate temperature of 600 ^{o}C, the morphology becomes more ordered consisting aggregates of regular structures with straight edges and corners. This confirms that the crystallinity of the films is significantly enhanced with an increase in deposition temperature. The AFM images shown in Figure 9.4 are also in agreement with FE-SEM images. It can be

deduced from the images that there is a continuous improvement of the structure from droplet like ones to grains with well-defined shape as the substrate temperature increases to 600 ^{o}C showing improvement in crystallinity.

The chemical compositions of the deposited films is analyzed using EDS and are depicted in Fig. 9.5. It shows that all the constituent elements of the powder are present in the films with the exception of holmium. The absence of the Ho^{3+} ion indicates that its concentration in the sample is below the sensitivity of the instrument.

The observed K:Y:F elemental ratios are 1:3.4:9.7, 1.1:3.8:9.3, 1.1:3.5:9.6 and 0.9:3.8:9.3 for the films deposited at 350, 400, 500 and 600 ^{o}C, respectively. As compared with the target composition of 1:3:10, the elemental ratios show decrease in K and F elements and an increase in Y for all the films. This may be due to the high background gas pressure (1.7 Torr) which causes some of the plasma species to loss their kinetic energy before reaching the surface of the substrate because of frequent collisions with the gas molecules. This phenomenon has the effect of decreasing the deposition rate [10, 22]. Particularly, for $KY_3F_{10}:Ho^{3+}$ phosphor thin films the deposition condition mainly depends on the masses of the individual species. It is because that the relative amount of the heavier species (Y in this case) that travel normal to the substrate will be higher than that of the lighter species at relatively higher pressures. This could be the reason why yttrium is found to have a relatively higher elemental ratio than the other two in the composition of the deposited films. In other words, the mass of Y which is approximately twice that of the mass of Ar seems to enable Y not to be much affected by the scattering due to Ar molecules.

X-ray Photoelectron Spectroscopy (XPS) is employed to further investigate the surface state of the film deposited at 600 ^{o}C. Figure 9.6 (a-b) shows the high resolution XPS spectra of $KY_3F_{10}:Ho^{3+}$ with peaks of Y 3d and F 1s. High resolution Gaussian peak fits were performed to get the identities of these peaks. Figure 9.6a shows the fitted high resolution Y 3d XPS peak. There are two fitted peaks assigned to Y $3d_{5/2}$ situated at 157.24 and 159.18 eV, and the other two peaks assigned to Y $3d_{3/2}$ situated at 159.24 and 161.18 eV. Figure 9.6b shows the high resolution F 1s XPS peak with two fitted peaks at 684.71 and 686.45 eV. The summary of XPS peak position, binding energy and area distribution of the film is given in Table 9.2.

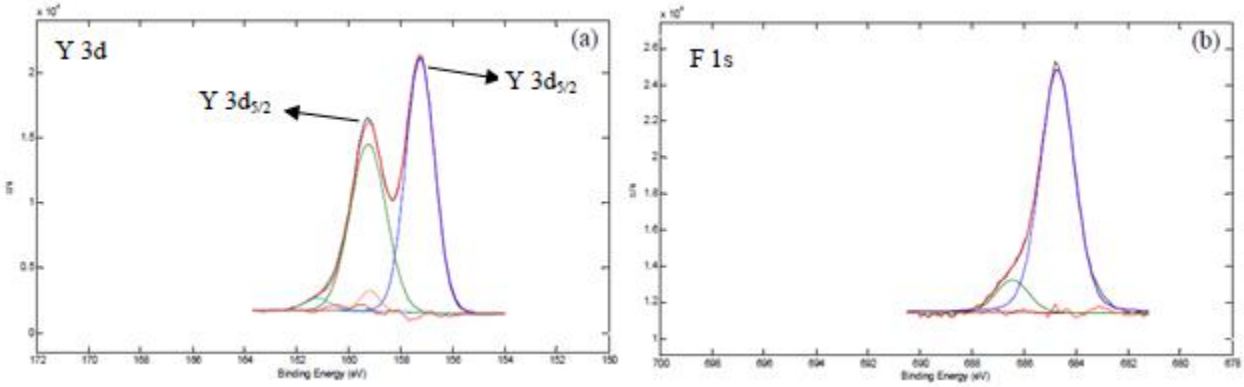

Fig. 9.6: (a) Y 3d, and (b) F 1s XPS spectra of the film deposited 600°C.

Table 9.2: XPS peak position, binding energy and area distribution of $KY_3F_{10}:Ho^{3+}$ thin film deposited at 600 °C.

$KY_3F_{10}:Ho^{3+}$	Binding energy (eV)	Area contribution (%)	Chemical compound
Y 3d	157.24	52.55	Y in $KY_3F_{10}:Ho^{3+}$
	159.18	3.00	YF_3
	159.24	42.04	Y in $KY_3F_{10}:Ho^{3+}$
	161.18	2.40	Y_2O_3
F 1s	684.71	89.61	F in $KY_3F_{10}:Ho^{3+}$
	686.45	10.39	F in $KY_3F_{10}:Ho^{3+}$

9.3.2 Photoluminescence properties

The PL excitation and emission spectra of $KY_3F_{10}:Ho^{3+}$ thin films deposited at temperatures of 400, 500 and 600 °C are depicted in Figure 9.7(a-c), respectively. It is observed that for all the substrate temperatures, the maximum PL intensity occurred at excitation of 454 nm. In particular, the green emission at the wavelength of 540 nm is studied for the excitation wavelengths of 362, 416, and 454 nm. Moreover, for all excitations a faint red (near infrared) emission was observed at 750 nm. This faint red emission is attributed to the $^5F_4 - ^5I_7$ and $^5S_2 - ^5I_7$ transitions, whereas the green emission spectrum observed at 540 nm wavelength is due to the $^5F_4 - ^5I_8$ and $^5S_2 - ^5I_8$ transitions. It is worth noting that such multiple emissions from other holmium doped phosphors are also reported [23].

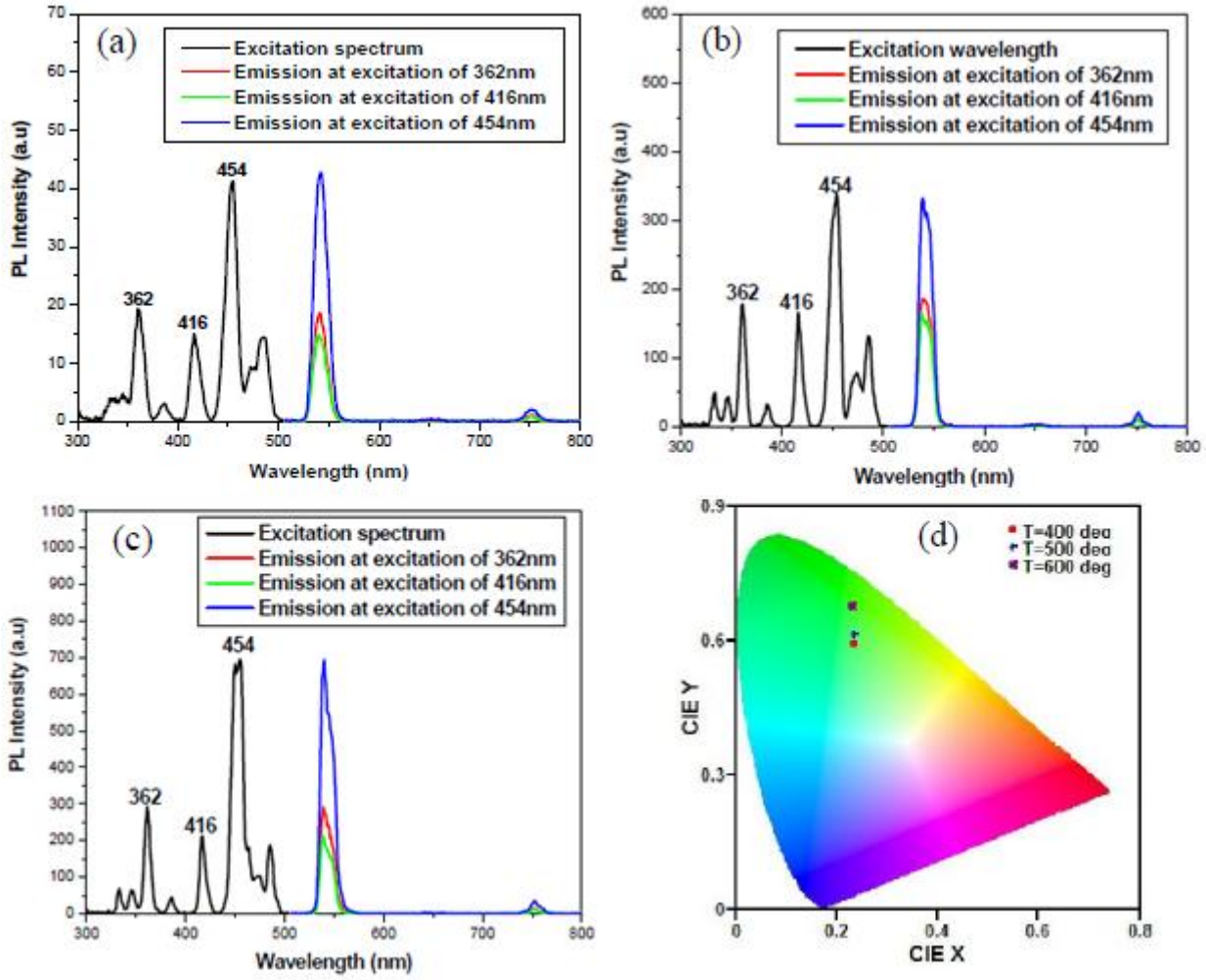

Fig. 9.7: PL excitation and emission spectra of $KY_3F_{10}:Ho^{3+}$ phosphor powder thin films prepared at (a) 400 ^oC, (b) 500 ^oC, (c) 600 ^oC and (d) the corresponding variation in chromaticity coordinates.

Moreover, the values of the chromaticity coordinates of $KY_3F_{10}:Ho^{3+}$ thin films that have been estimated from the 1931 Commission Internationale de l'Eclairage (CIE) system for the excitation wavelength of 454 nm are depicted in Figure 9.7d. The CIE system enables us to visualize the variation in color that is emitted from prepared samples. The values of the chromaticity coordinates, often expressed as (x,y), are (0.235, 0.594), (0.245, 0.615), and (0.245, 0.678) for the thin films deposited at 400, 500, and 600 ^oC, respectively. These values indicates that that a relatively intense green emission is expected to be seen for the thin films deposited under relatively higher substrate temperature, in agreement with that observed in Figure 9.7(a-c).

Figure 9.8 shows the variation of emission peaks that correspond to the three excitation wavelengths of 362, 416, and 454 nm. It can be observed that the intensity of PL emission significantly improves with an increase of the substrate temperature. This could be attributed to the improved crystallinity of the films at higher temperatures. In general, higher substrate temperatures during deposition results to an increase in the surface mobility of the atomic species in the films thereby improving the crystallinity, which in turn enhances the luminescence intensity.

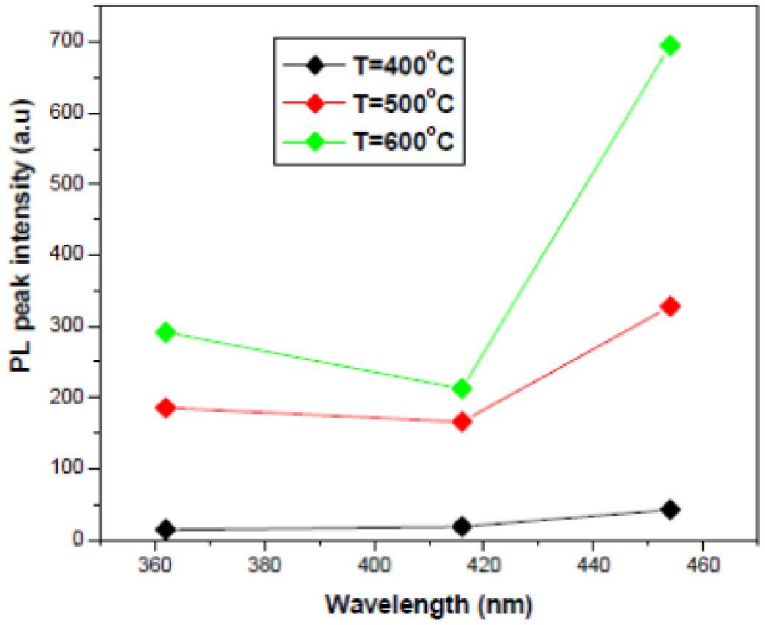

Fig. 9.8: Variation of emission peaks corresponding to excitation wavelengths of 362, 416 and 454 nm with temperature.

Conclusion

The structural, morphological and PL properties of $KY_3F_{10}:Ho^{3+}$ thin films have been studied in a wide temperatures range. The crystallite size of the deposited films varied between 39-74 nm depending on the substrate temperature. Yttrium is the dominant composition in the deposited films and this is attributed to its higher mass as compared to potassium and fluorine. Green PL emission at 540 nm was investigated at three main excitation wavelengths; namely, 362, 416 and 454 nm. In addition, faint red (near infrared) emission was observed at 750 nm for all the excitations. The emission peaks of the films increases with increasing the substrate temperature

and this is attributed to the improved crystallinity of the films at such higher substrate temperatures. The green emission at 540 nm is ascribed to the $^5F_4$–$^5I_8$ and $^5S_2$–$^5I_8$ transitions and the faint red emission at 750nm is due to the $^5F_4$ –$^5I_7$ and $^5S_2$–$^5I_7$ transitions.

References

[1] D. S. Pytalev, E. P. Chukalina, M. N. Popova, G. S. Shakurov, B. Z. Malkin, S. L. Korableva, Phys. Rev. B 86, 1 (2012).

[2] S. Khiari, F. Bendjedaa, M. Diaf, Optics and Photonics Journal 3, 13 (2013).

[3] M. Mujaji, Jon-Paul R. Wells, J. Phys.: Condens. Matter 21, 1 (2009).

[4] T. Yanagida, Y. Fujimoto, K. Fukuda, Jpn. J. Appl. Phys 53, 1 (2014).

[5] A. Rapaport, J. Milliez, F. Szipocs, M. Bass, A. Cassanho, H. Jenssen, Appl. Opt. 43, 6477 (2004).

[6] Z. Jin-Su, Z. Hai-Yang, S. Jan-Shi, C. Li-Hong, L. Xiang-Ping, C. Bao-Jiu, Chin. Phys. Lett. 29, 1 (2012).

[7] A. Braud, S. Girard, J. L. Doualan, M. Thuau, R. Moncorge, A. M. Tkachuk, Phys. Rev. B 61, 5280 (2000).

[8] Y. Kalisky, The Physics and Engineering of Solid State Lasers, USA, 2006.

[9] C. Benvenuti, P. Chiggiato, F. Cicoira, V. Ruzinow, Vacuum 50, 57 (1998).

[10] J. Gonzalo, R. Gomez San Roman, J. Perriere, C. N. Afonso, R. Perez Casero , Appl. Phys. A 66, 487 (1998).

[11] N. G. Debelo, F. B. Dejene, K. T. Roro, M. P.Pricilla, C. Oliphant, Appl. Phys. A, 122, 1 (2016).

[12] S. S. Yi, J. S. Bae, B. K. Moon, J. H. Jeong, I. W. Kim, H. L. Park, Appl. Phys. A 76, 433 (2003).

[13] S. Aoqui, H. Miyata, T. Ohshima, T. Ikegami, K. Ebihara, Thin Solid Films 407, 126 (2002).

[14] A. Og. Dikovska, P. Atanasov, C. Vasilev, I. Dimitrov, T. Stoyanchov, Journal of Optoelectronics and Advanced Materials 7, 1329 (2005).

[15] J. Lackner, Surface and Coatings Technology 163, 300 (2003).

[16] S. Ting, Journal of Nanomaterials 2012, 1 (2012).

[17] M. Begam, N. Rao, S. Kaleemulla, M. Shobana, N. Krishna, M. Kuppan, J. Nano. Elec. Phys. 5, 03019 (2013).

[18] K. Wu, M. Chem, Thin Solid Films 516, 3808 (2008).

[19] J. J. Dolo, O. M. Ntwaeaborwa, J. J. Terblans, E. Coetsee, B. F. Dejene, M. M. Biggs, H. C. Swart, Appl. Phys. A 101, 655 (2010).

[20] Z. Wei, W. Ya, C. XiangMing, Chinese Science Bulletin 58, 3398 (2013).

[21] M. A. El Khakani. B. Le Drogoff, M. Chaker, Journal of Materials Research 14, 3241 (1999).

[22] T. Scharf, H. U. Krebs, Appl. Phys. A 75, 551 (2002).

[23] A. Pandey and V. K. Rai, Dalton Trans. 42, 1 (2013).

Chapter 10

Cathodoluminescence properties of $KY_3F_{10}:Ho^{3+}$ thin films

10.1 Introduction

Cathodoluminescence (CL) is a luminescence phenomenon which occurs because of irradiation with beam of electrons [1-2]. When a crystal is bombarded by a stream of high-energy electrons in a scanning electron microscope (SEM) or other suitable instrument, CL emission is observed. Studying the origin of CL in artificial crystals is important because of their economic importance in the manufacture of television screens, computer monitors, and the like. CL is a technique which has been conventionally used to investigate some characteristics of specimens, such as trace impurities and lattice defects, as well as to investigate crystal distortion [3-4]. The emission of photons from a sample undergoing bombardment by high-energy electrons is related to the presence of electron traps within the band gap between the conduction and valence energy bands. De-energizing electrons, falling back from the excited state in the conduction band to the valence band, are attracted and held momentarily by these traps. Some of the energy lost when electrons vacate traps, and continue their fall to the valence band, is converted into photons.

Recently, CL study of Ce^{3+}activated silicate commercial phosphors has attracted much attention because of its application in various display devices such as Cathode Ray Tube (CRT) and Television screen [5-6]. However, since Ho^{3+} has several high lying metastable levels (as compared to Ce^{3+}) giving rise to transitions at various wavelengths from infrared (IR) to ultraviolet (UV) region, studying the luminescence properties of Ho^{3+} activated phosphors seems more advantageous. This is to fill the gap that highly efficient phosphor materials are required for the development of high resolution display devices mentioned above. Moreover, the unique advantage of displays based on thin film phosphors is that they are characterized by high contrast and resolution, good thermal conductivity as well as a high degree of uniformity and better adhesion [7–11]. In addition, fluoride materials are promising candidates for display devices based on thin film phosphors because of their low phonon energies. This contributes a lot in obtaining high luminescence efficiency by reducing the non-radiative quenching phenomena [12-13].

The unique advantage of Potassium triyttrium decafluoride (KY_3F_{10}) is that it has good optical, thermal and mechanical properties which are comparable to other fluoride materials such as $LiYF_4$. It also melts congruently and suitable for doping with rare earth ions. Moreover, it has higher energy transfer efficiency in it than other fluorides such as BaY_2F_8 and $LiYF_4$ which makes it an interesting material for further study [14]. Thin films of this material can be prepared using one of the thin film deposition techniques called pulsed laser deposition (PLD).

PLD is a thin film deposition technique which has been popular, versatile and highly flexible method for the thin film growth of various materials. In PLD, the background gas pressure is one of the critical parameters that determine the final step of the film formation. Moreover, it also determines the amorphous or crystalline nature of the deposited films [15-17]. It is reported that the pressure of the background gas highly influences the CL properties of thin films; more intense CL emission being obtained at high pressures. Therefore, in this paper, the structural, morphological, CL and photoluminescence (PL) properties of $KY_3F_{10}:Ho^{3+}$ thin films deposited at high and low background argon gas pressures are reported.

10.2 Experimental details

The experiments were performed by Nd-YAG laser (266 nm, pulse duration of 10 ns, repetition rate of 2Hz). The laser fluence was kept at $1.2 J/cm^2$. The vacuum chamber was pumped to a background pressure of 4×10^{-5} Torr before introducing argon. The gas pressures used were 5 mTorr and 2 Torr while the substrate temperature was kept at 500^{o}C. The targets were made from commercial $KY_3F_{10}:Ho^{3+}$ powder pressed in to pellets. The structure and phase purity of the films were analyzed by X-ray diffraction (XRD) using Bruker D8 advance X-ray diffractometer operating at 40kv and 40mA using Cu Kα = 0.15406nm and the elemental composition of the thin film was studied using Energy Dispersive X-ray Spectrometer (EDS). The morphology was studied using Field Emission Scanning Electron Microscope (FE-SEM) and Atomic Force Microscope (AFM). The PL excitation and emission spectra were measured at room temperature using Cary Eclipse fluorescence spectrometer model: LS-55 with a built-in 150W xenon flash lamp. SEM-CL was used to study the CL properties of the grown films.

10.3 Results and discussion

10.3.1 Structural and morphological properties

Figure 10.1 depicts the XRD pattern of the deposited films and the miller indices of the prominent peaks. This result indicates that the films crystallized in monoclinic structure of KY_3F_{10} (in agreement with JCPDS card No 27-0465).

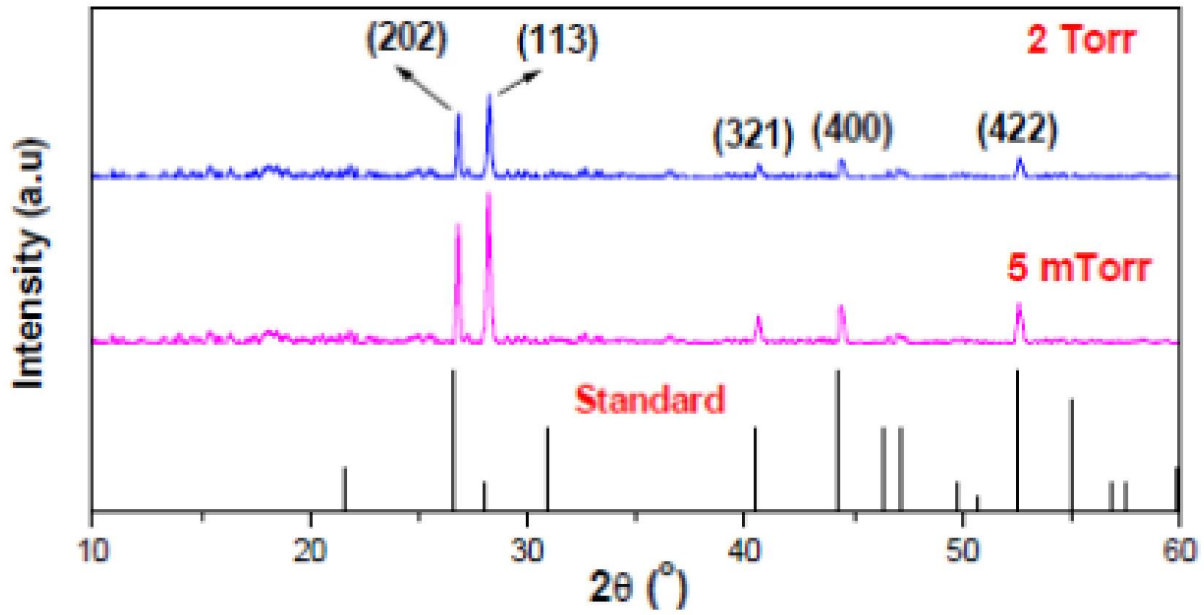

Fig. 10.1: XRD pattern of KY_3F_{10}: Ho^{3+} films deposited at pressures of 5 mTorr and 2 Torr.

The average crystallite size has been computed from the full width at half maximum (FWHM) of the prominent (202) and (113) peaks using equation (5.2).The average crystallite size of the films varied between 62 and 21nm for the films deposited at 5 mTorr and 2 Torr respectively.

Quantitative information concerning the preferential crystallite orientation was obtained from the texture coefficient ($TC(hkl)$). It represents the texture of a particular plane and its deviation from unity implies a preferred growth. $TC(hkl)$ is defined as [18-19],

$$TC(hkl) = \frac{I(hkl)/I_0(hkl)}{N^{-1}\sum_N (I(hkl)/I_0(hkl))} \qquad (10.1)$$

where $I(hkl)$ is the measured intensity of (hkl) diffraction peak, $I_0(hkl)$ is the standard intensity of JCPDS and N is the total number of diffraction peaks considered in the analysis. The

value of $TC(113)$ for the (113) peak of the two films is greater than unity indicating preferential growth of $KY_3F_{10}:Ho^{3+}$ crystal along C-axis.

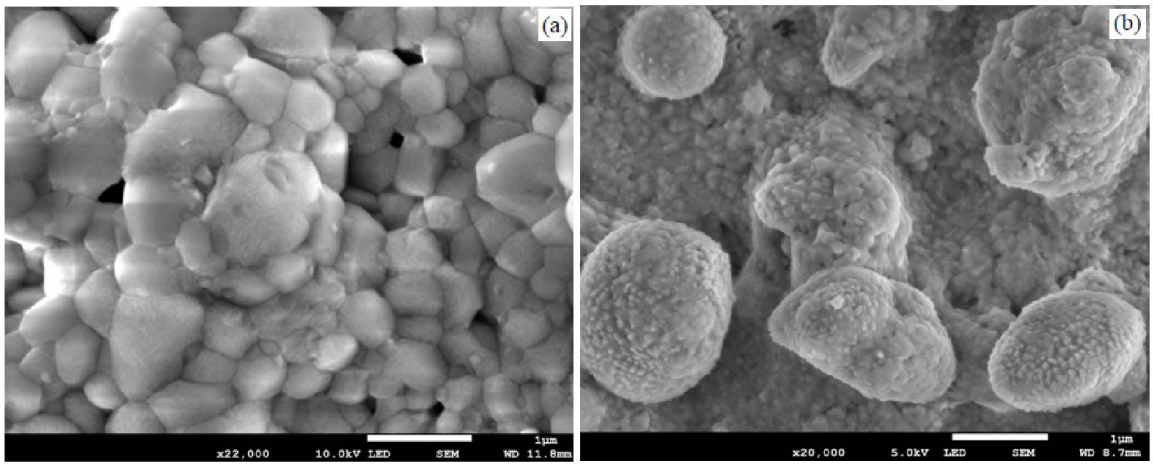

Fig. 10.2: FE-SEM images of the films deposited at (a) 5 mTorr, and (b) 2 Torr.

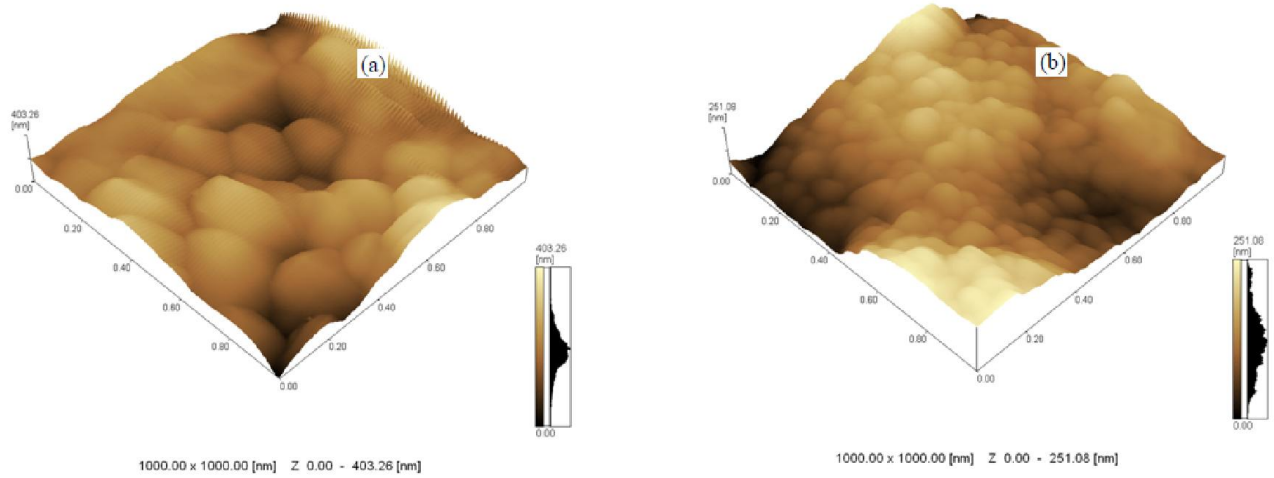

Fig. 10.3: AFM images of the films deposited at (a) 5 mTorr, and (b) 2 Torr.

Figure 10.2(a) and (b) shows the FE-SEM images of the films deposited at pressures of 5 mTorr and 2 Torr. From the images, it can be observed that the film deposited at low pressure of 5 mTorr has well defined grain shapes with larger sizes. However, the film deposited at 2 Torr has more agglomerated small grain sizes not grown to some definite shape. The same effect has been observed from AFM images shown in Figure 10.3(a-b). Therefore, the film deposited at low pressure has improved crystalline structure as compared to that deposited at high pressure.

Figure 10.4(a-b) shows the EDS spectra of the prepared films which show deviation from the target composition. P. Orgiani et al reported that the background gas pressure plays significant role in determining the transport properties and chemical composition of thin films prepared by PLD [20]. According to P. Orgiani et al the increase in pressure might selectively affect both the energy and the efficiency of the single species transfer to the growing film. Similar results of selective species transfer under a certain deposition conditions were reported by J. Gonzalo et al [21] and hence thin film composition congruent to the target may not be obtained under some conditions.

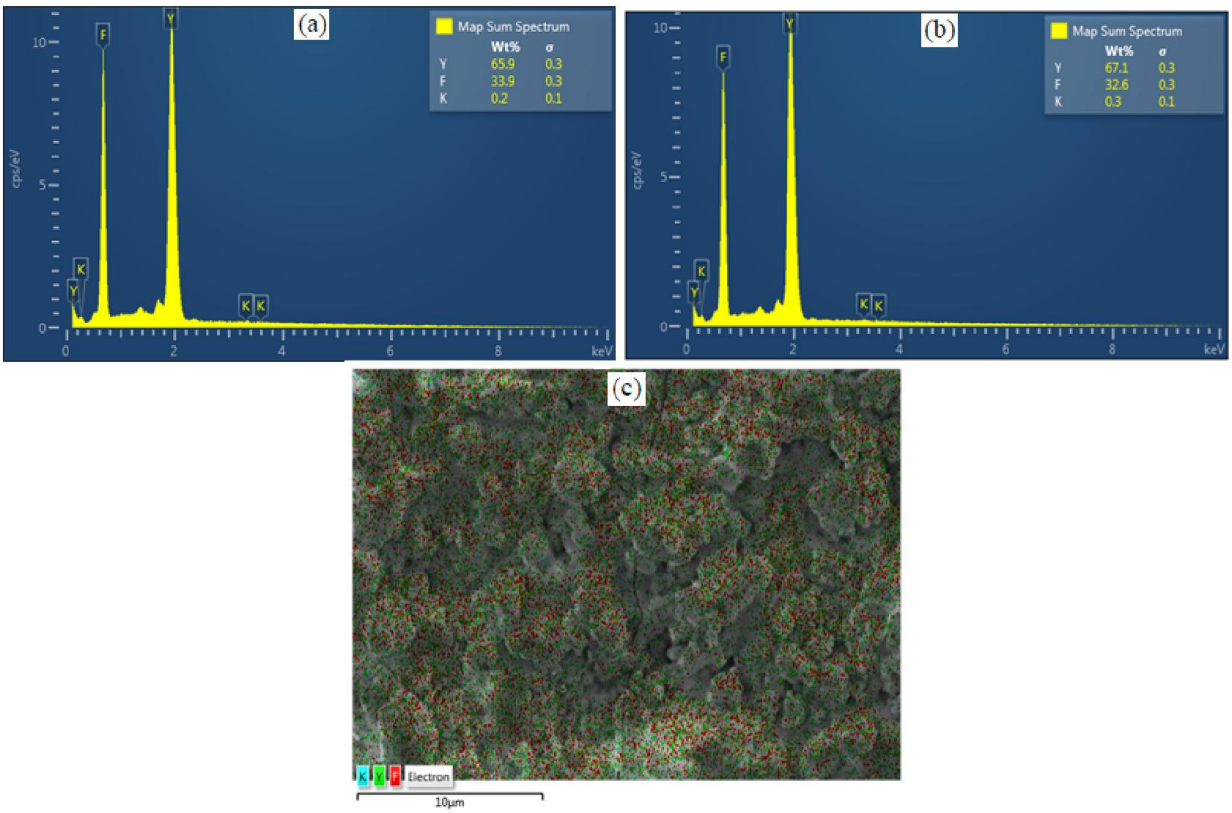

Fig. 10.4: The EDS spectra of $KY_3F_{10}:Ho^{3+}$ films deposited at (a) 5 mTorr, and (b) 2 Torr; (c) shows the elemental mapping of the film deposited at 5 mTorr.

Figure 10.4(c) shows the elemental mapping of the film deposited at a pressure of 5 mTorr. It shows Y-excess and similar result has been obtained for the film deposited at 2 Torr. J. Gonzalo et al. reported that if the background gas pressure is high, some of the plasma species may loose their kinetic energy before reaching the surface of the substrate which in turn decreases the deposition rate [21-22]. In this case, the deposition condition depends on the masses of the

individual species [21]. In other words, the mass of Y is approximately twice of the mass of Ar and Y doesn't seem to be much affected by the scattering due to Ar molecules. This means that the relative amount of the heavier species (Y in this case) that travel along the normal to the substrate will be higher than that of the lighter species at relatively higher pressures. This could be one cause for the observed Y-excess in the films.

10.3.2. Luminescence properties

Figure 10.5(a-b) shows the PL excitation and emission spectra of $KY_3F_{10}:Ho^{3+}$ thin films. The PL spectra show an intense green emission at about 540nm. In addition, red emissions were observed around 650 and 750nm. The green emission at 540 nm is ascribed to the $^5F_4$–$^5I_8$ and $^5S_2$–$^5I_8$ transitions, the red emission around 650 nm is assigned to the $^5F_5$ –$^5I_8$, transition and the other red emission around 750 nm is due to the $^5F_4$ –$^5I_7$, $^5S_2$–$^5I_7$ transitions of Ho^{3+}. Such multiple emissions from other holmium doped phosphor is also reported in literature [23].

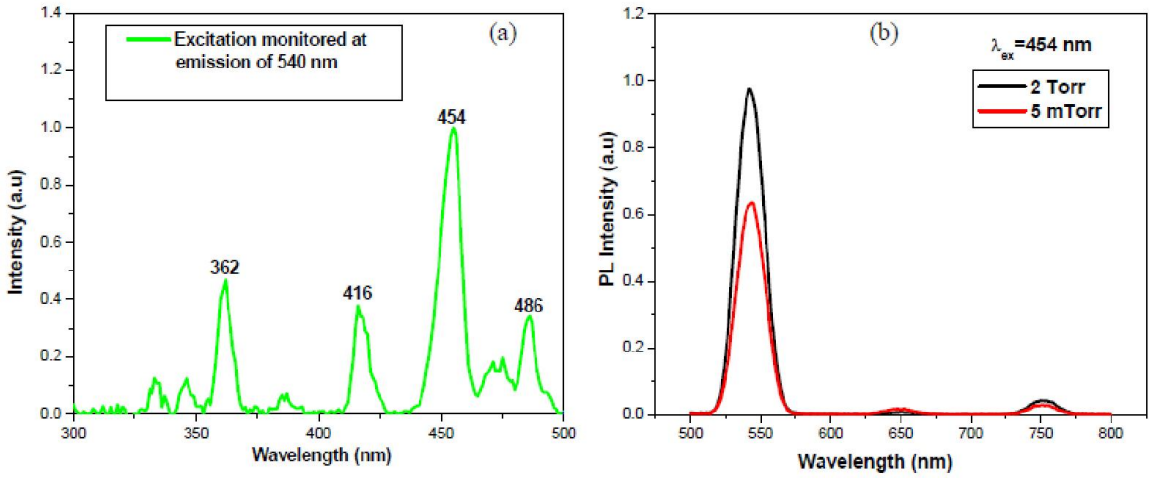

Fig. 10.5: The PL (a) excitation, and (b) emission spectra of $KY_3F_{10}:Ho^{3+}$ thin films.

Significant increment in the intensity of the PL was observed as the deposition pressure is increased from 5 mTorr to 2 Torr. This could be attributed to the small grain size obtained at high deposition pressure of 2 Torr. C. T. Tsai, et al, reported that as the grain size is decreased, the ratio of surface to volume of the grain is increased leading to enhancement of PL intensity of the deposited films [24].

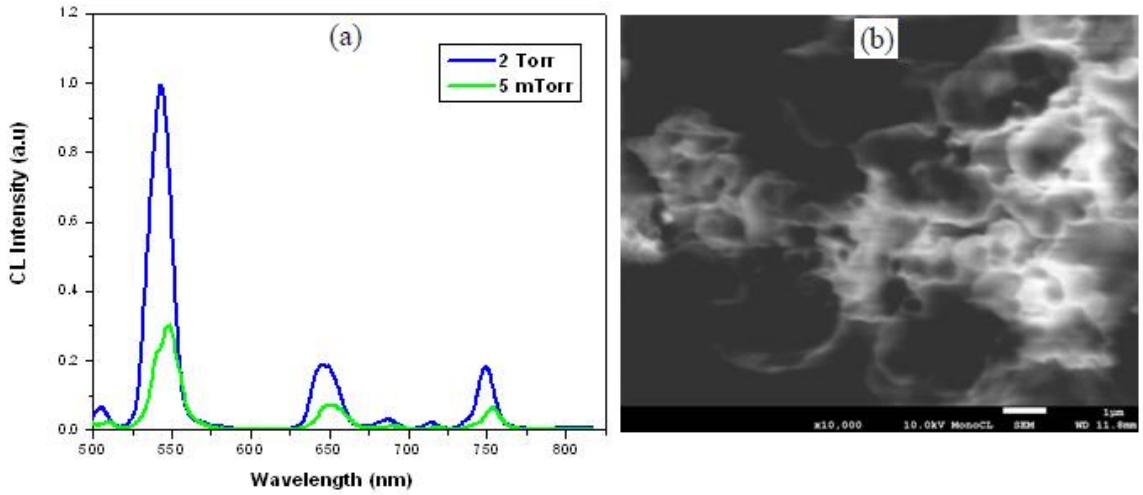

Fig. 10.6: The (a) CL spectra of the prepared films, and (b) CL image of the film deposited at 2 Torr.

The CL emission spectra are similar to those of the PL with the main peak at 540 nm, except the slight shift of the emission peaks to high wavelength region for the film deposited at 5 mTorr (Figure 10.6(a)). This suggests that the electron beam did not change the electron energy level configuration or transitions of the activator ion in the film. Moreover, Figure 10.6(b) shows the CL image of the deposited film (at 2 Torr) with non-uniform distribution of luminescent centers.

Conclusion

The structural, morphological and luminescence properties of $KY_3F_{10}:Ho^{3+}$ thin films deposited under high and low argon gas pressures are investigated. Improved crystalline structure with well defined grain shapes is obtained for films deposited at low gas pressure. The elemental composition of both films show Y-excess. Green PL emission at 540nm was investigated at excitation wavelength of 454 nm. In addition, red emissions were observed around 650 and 750nm. The green emission at 540 nm is ascribed to the $^5F_4 – ^5I_8$ and $^5S_2 – ^5I_8$ transitions, the red emission around 650 nm is assigned to the $^5F_5 – ^5I_8$, transition and the other red emission around 750 nm is due to the $^5F_4 – ^5I_7$, $^5S_2 – ^5I_7$ transitions of Ho^{3+}. The CL image shows non uniform distribution of luminescent centers in the deposited films. Moreover, the CL emission spectra are similar to those of the PL with the main peak at 540 nm, suggesting that the electron beam did not change the electron energy level configuration or transitions of the activator ion in the film.

References

[1] C. M. Sunta, Unravelling Thermoluminescence, 2015, Springer, London

[2] S.W.S. McKeever, Thermoluminescence of solids, Cambridge Solid State Science Series, Oklahoma State University, 1988.

[3] M. A. Stevens-Kalceff, Miner. Petrol. 107, 455 (2013).

[4] M. Dar, G. Jacopin, M. Hezam, N. Arora, S. Zakeeruddin, B. Deveaud, M. Nazeeruddin, M. Gratzel, ACS Photonics 3, 947 (2016).

[5] E. Bosze, G. Hirata, L. Rohwer, J. McKittrick, J. Lumin. 104, 47 (2003).

[6] G. Li, Y. Wang, W. Zeng, W. Chen, S. Han, H. Guo, Y. Li, J. Mater. Chem. C 4, 3304 (2016).

[7] P. F. Carcia, L. H. Brixner, Thin Solid Films 115, 89 (1984).

[8] M. Leskela, Journal of alloys and Compounds, 275, 702 (1998).

[9] A.M. Chinie, S. Georgescu, A. Mateescu, A. Stefan, Rom. J. Phys. 51, 827 (2006).

[10] K. Sohn, D. Park, J. Yoo, J. Kim, Jpn. J. Appl. Phys. 44, 1787 (2005).

[11] J. S. Bae, J. P. Kim, U. C. Choi, J. Kor. Phys. Soc. 49, 616 (2006).

[12] L. S. Chamberlain, L. R. Corruccini, Phys. Rev. B 71, 024434(2005).

[13] S. Khiari, F. Bendjedaa, M. Diaf, Optics and Photonics Journal 3, 13 (2013).

[14] A. Braud, S. Girard, J. L. Doualan, M. Thuau, R. Moncorge, A. M. Tkachuk, Phys. Rev. B 61, 5280 (2000).

[15] J. Gonzalo, R. Gomez San Roman, J. Perriere, C. N. Afonso, R. Perez Casero , Appl. Phys. A 66, 487 (1998).

[16] S. S. Yi, J. S. Bae, B. K. Moon, J. H. Jeong, I. W. Kim, H. L. Park, Appl. Phys. A 76, 433 (2003).

[17] Z. W. Ya, C. XiangMing, Chin. Sc. Bull. 58, 3398 (2013).

[18] Y. Wang, W. Tang, L. Zhang, J. Mater. Sci. Technol. 31, 175 (2015).

[19] J. Antonio Rivera Marquez, Int. J. Electrochem. Sci. 6, 4059 (2011).

[20] P. Orgiani, R. Ciancio, A. Galdi, S. Amoruso, and L. Maritato, Appl. Phys. Lett. 96, 032501 (2010).

[21] J. Gonzalo, R. Gomez San Roman, J. Perriere, C. N. Afonso, R. Perez Casero , Appl. Phys. A 66, 487(1998)

[22] B. Cullity, Elements of X-ray Diffraction, Addison-Wesley publishing (USA) 393.

[23] A. Pandey, V. Kumar, Dalton Trans. 42, 11005 (2013).

[24] C. T. Tsai, D. S. Chuu, G. L. Chen, and S. L. Yang, Journal of Applied Physics 79, 9105 (1996).

Chapter 11

Conclusion and recommendation for future work

In this thesis, the various properties of commercially obtained $Y_2SiO_5:Ce^{3+}$ and $KY_3F_{10}:Ho^{3+}$ phosphor powders are studied. Moreover, the influence of the various deposition parameters such as background gas pressure, target to substrate distance and substrate temperature on the structural and luminescence properties of the $Y_2SiO_5:Ce^{3+}$ and $KY_3F_{10}:Ho^{3+}$ thin films grown by pulsed laser deposition is investigated.

11.1. Conclusion

For both $Y_2SiO_5:Ce^{3+}$ and $KY_3F_{10}:Ho^{3+}$ commercial phosphor powders, the TL intensity increases with an increase in UV exposure time for up to 20 minutes and then decreases. This implies that both powders may be used in the application of UV dosimetry up to 20 minutes of UV dose. The TL intensity peak shifts slightly to higher temperature region for relatively high heating rates, but with reduced intensity peak. For $Y_2SiO_5:Ce^{3+}$, the decrease in TL intensity at high heating rates could be ascribed to thermal quenching effect, in which the efficiency of the luminescence decreases as the temperature increases due to opening up of competing non-radiative relaxation pathways. However, this phenomenon is not attributed to thermal quenching effect for the case of $KY_3F_{10}:Ho^{3+}$. Important TL kinetic parameters, such as the activation energy (E) and the frequency factor (s) were calculated from the glow curves using variable heating rate (VHR) method. The variations of gas pressure and background gas atmosphere have also significant effect on the TL intensities and structure of $Y_2SiO_5:Ce^{3+}$ thin films. The highest TL intensity was obtained for the film deposited using argon as a background gas. Moreover, increase in oxygen pressure resulted in an increase in TL intensity of the films.

PL analysis of $KY_3F_{10}:Ho^{3+}$ phosphor powder shows that green emission at 540 nm which is ascribed to $^5F_4$–$^5I_8$ and $^5S_2$–$^5I_8$ transitions and faint red emission at 750 nm which is due to the $^5F_4$ –$^5I_7$ and $^5S_2$–$^5I_7$ transitions are observed. In addition to the sharp green emission at 540 nm, a broad emission centered at 600 nm was observed for excitation wavelength of 362 nm and it could be attributed to defects in the host. The photoluminescence life time of the phosphor is of the order of few milliseconds and hence it could be useful for scintillation.

The crystallite size of $KY_3F_{10}:Ho^{3+}$ films deposited in various argon gas pressures varied between 54 - 57 nm. It is observed that surface roughness of the deposited films increase with an increase in the gas pressure. The photoluminescence emission peaks of the films increases with increasing the deposition pressure and this is attributed to the increase in surface roughness at such higher deposition pressures.

Degradation in crystalline quality is observed at larger values of target to substrate distance during deposition. The estimated thickness of the films decreases with increasing target to substrate distance and this could be attributed to the decrease in deposition rate at such larger distances.

For the $KY_3F_{10}:Ho^{3+}$ thin films studied in a wide temperatures range, the crystallite size of the deposited films varied between 39 – 74 nm depending on the deposition temperature. The chrystallinity and PL intensity are also enhanced for the films deposited at high substrate temperature. Unusual grow mechanism was observed for the films deposited at low temperature region, i.e., from 0-350^{o}C.

For all $KY_3F_{10}:Ho^{3+}$ thin films grown in various parameters, green PL emission at 540 nm was investigated at three main excitation wavelengths; namely, 362, 416 and 454 nm. In addition, faint red (near infrared) emission was observed at 750 nm for all the excitations. The green emission at 540 nm is ascribed to the $^5F_4$–$^5I_8$ and $^5S_2$–$^5I_8$ transitions and the faint red emission at 750 nm is due to the $^5F_4$ –$^5I_7$ and $^5S_2$–$^5I_7$ transitions. Moreover, Yttrium is the dominant composition in the deposited films and this is attributed to its higher mass as compared to potassium and fluorine.

The structural and luminescence properties of KY_3F_{10}:Ho^{3+} thin films deposited under high and low argon gas pressures were also investigated. Enhanced crystalline structure with well defined grain shapes is obtained for deposition using low gas pressure. The CL image shows non uniform distribution of luminescent centers in the deposited films. Moreover, the CL emission spectra are similar to those of the PL with the main peak at 540 nm, suggesting that the electron beam did not change the electron energy level configuration or transitions of the activator ion in the film.

11.2. Recommendation for future work

Future work on these phosphors includes exploration of their structural and luminescence properties using various parameters such as different deposition time and background atmosphere (vacuum). The influence of laser fluence, room temperature and high pressure (3-4

Torr) depositions can also be investigated. Post deposition annealing in non reactive atmosphere is also one interesting aspect for studying film properties.

To minimize the formation of unwanted bigger particles on the surface of the films, applying off axis PLD technique is one interesting method. In this technique the substrate is mounted at an angle where the plume is not directly focused on the substrate. Detail depth profiling and XPS analysis can also be done.

11.3. Publications

1. The effect of argon gas pressure on structural, morphological and photoluminescence properties of pulsed laser deposited KY_3F_{10}:Ho^{3+} thin films, Appl. Phys A **122**, 619 (2016).
2. Thermally stimulated luminescence of Y_2SiO_5:Ce^{3+} commercial phosphor powder and thin films, International journal of Thermophysics **37**(7), 1 (2016).
3. Thermoluminescence and photoluminescence properties of KY_3F_{10}:Ho^{3+} commercial phosphor powder, Physica scripta **91**(6), 1(2016).
4. Pulsed laser deposited KY_3F_{10}: Ho^{3+} thin films: Influence of target to substrate distance Materials Chemistry and Physics, DOI: 10.1016/j.matchemphys.2016.12.064
5. Enhanced emission and improved crystallinity of KY_3F_{10}: Ho^{3+} thin films grown at high deposition temperature (Submitted to Materials Research Bulletin).
6. Cathodoluminescence properties of KY_3F_{10}: Ho^{3+} thin films (Submitted to SAIP 2016).

11.4. Conference and Workshop participations

1. Egypt-South Africa Collaboration, University of the Free State, Qwa Qwa`campus, 2015.
2. South African Institute of Physics, Port-Elizabeth, 2015.
3. Workshop on pulsed laser deposition, Universidade Eduardo Mondlane, Mozambique, 2015.
4. South African Institute of Physics, Cape Town, 2016.